Copy No. 6

DEFENCE R&D DÉFENSE

DEVELOPMENT OF A DYNAMIC ANALYSIS CAPABILITY IN THE VAST FINITE ELEMENT CODE FOR PRE-STRESSED ENGINE MOUNT STRUCTURES

L. Jiang – M.W. Chernuka

MARTEC Limited

DEFENCE RESEARCH ESTABLISHMENT ATLANTIC

Contractor Report

DREA CR 1999-090

April 1999

National Defence Défense nationale

Canada

101-02395/

National Defence
Research and Development Branch

Défense nationale
Bureau de recherche et développement

DREA CR 1999-090

DEVELOPMENT OF A DYNAMIC ANALYSIS CAPABILITY IN THE VAST FINITE ELEMENT CODE FOR PRE-STRESSED ENGINE MOUNT STRUCTURES

By
L. Jiang – M.W.Chernuka

MARTEC Limited
Suite 400, 1888 Brunswick Street
Halifax, Nova Scotia, Canada
B3J 3J8

Scientific Authority
D.C. Stredulinsky

W7707-8-5700/001/HAL
Contract Number

April 1999

CONTRACTOR REPORT

Prepared for

Defence Research Establishment Atlantic

Centre de Recherches pour la Défense Atlantique

Canada

REPRODUCTION QUALITY NOTICE

This document is the best quality available. The copy furnished to DRDCIM contained pages that may have the following quality problems:

: Pages smaller or Larger than normal

: Pages with background colour or light coloured printing

: Pages with small type or poor printing; and or

: Pages with continuous tone material or colour photographs

Due to various output media available these conditions may or may not cause poor legibility in the hardcopy output you receive.

☒ **If this block is checked, the copy furnished to DRDCIM contained pages with colour printing, that when reproduced in Black and White, may change detail of the original copy.**

ABSTRACT

The work presented in this report was motivated by the results of a previous frequency response analysis of a pre-stressed block rubber engine mount using the 20-noded solid element in the VAST finite element program. These results indicated that when the geometric stiffness matrix was included, the acoustic stiffness of the mount was significantly underestimated. In order to investigate the cause of this discrepancy in the numerical solutions, an extensive finite element study of the engine mount was first carried out in the present contract using VAST and other commercial FE packages. The results from this numerical study confirmed the correctness of the VAST element, but also clearly revealed the need for a nonlinear hyperelastic material model in order to accurately characterize the dynamic behaviour of the pre-stressed engine mount structures.

After a survey of the state-of-the-art literature on finite element procedures for large strain problems, it was concluded that the co-rotational formulation for the 3D solid element proposed by Crisfield and co-workers was especially suitable for implementation into the VAST program. This was not only because this co-rotational method was derived using the same concept as the element-independent co-rotational formulations already incorporated into the shell and beam elements in VAST, but also because it was based on Biot strain and stress measures which simplified the implementation of the hyperelastic material constitutive equations. The theoretical background and computer implementation issues for the co-rotational formulation and the hyperelastic material model are given in this report in detail. A large number of numerical examples have been solved for verification purposes. However, due to the constraint on budget, several simplifications and approximations were made in the present implementation. These must be addressed in the next phase of development.

RÉSUMÉ

Les travaux présentés dans ce rapport ont été réalisés suite aux résultats d'une analyse antérieure de la réponse en fréquence d'un bâti de moteur en caoutchouc dans lequel agissaient des pré-contraintes. Ces résultats indiquent que lorsque la matrice de rigidité géométrique est incluse, la rigidité acoustique du bâti est considérablement sous-estimée. Afin d'étudier la cause de cet écart dans les solutions numériques, une étude approfondie à éléments finis du bâti moteur a d'abord été effectuée dans le présent contrat à l'aide du VAST et d'autres programmes à éléments finis. Les résultats de cette étude numérique ont confirmé l'exactitude de l'élément VAST, mais ont également révélé la nécessité de disposer d'un modèle de matériau hyper-élastique non linéaire afin de caractériser avec précision le comportement dynamique des structures de bâti de moteur à pré-contraintes. Après une étude de la documentation technique de pointe sur les procédures à éléments finis pour les problèmes de grandes contraintes, on a conclu que la formulation co-rotationnelle pour l'élément solide 3D proposée par Crisfield et ses collègues convenait particulièrement bien à la mise en œuvre dans le programme VAST, non seulement parce que la méthode co-rotationnelle était dérivée à l'aide du même concept que les formulations co-rotationnelles indépendantes des éléments déjà intégrées dans les éléments carter et profilé en I dans le VAST, mais aussi parce qu'elle était fondée sur les mesures de déformations et de contraintes qui simplifiaient la mise en œuvre des équations constitutives des matériaux hyper-élastiques. Le fondement théorique et les questions de mise en œuvre informatique de la formulation co-rotationnelle et du modèle de matériau hyper-élastique sont précisées dans le rapport. Un grand nombre d'exemples numériques ont été résolus à des fins de vérification. Toutefois, en raison des restrictions budgétaires, plusieurs simplifications et approximations ont été apportées à la mise en œuvre. Elles seront traitées dans la prochaine phase du développement.

TABLE OF CONTENTS

ABSTRACT ii
TABLE OF CONTENTS iii
LIST OF TABLES v
LIST OF FIGURES vi

1. INTRODUCTION 1.1

2. NUMERICAL ANALYSES OF THE BLOCK RUBBER ENGINE MOUNT 2.1
   - 2.1 Buckling Analyses of the Engine Mount Model 2.1
   - 2.2 Direct Frequency Response Analysis of the Engine Mount Model 2.3
   - 2.3 Nonlinear Static and Dynamic Analyses of the Engine Mount 2.4

3. DEVELOPMENT OF AN 8-NODED NONLINEAR SOLID ELEMENT FOR THE VAST PROGRAM 3.1
   - 3.1 Theoretical Derivation of the Co-Rotation Formulation for 3-D Solid Element 3.1
   - 3.2 Implementation of the Co-Rotational Formulation into the VAST Program 3.10
   - 3.3 Numerical Verification of the 8-Noded Nonlinear Solid Element 3.12
     - 3.3.1 Patch Test – In-plane Stretching and Bending of a Plate 3.12
     - 3.3.2 Bending of a Nearly Incompressible Cantilever Beam 3.12
     - 3.3.3 Linear Buckling Analysis of a Cantilever Beam Under Axial Compression 3.13
     - 3.3.4 Geometrically and Materially Nonlinear Analysis of a Simply-Supported Plate Under Uniform Pressure 3.13
     - 3.3.5 Large Displacement Analysis of a 45° Bend Subjected to an Out-of-Plane Force 3.14
     - 3.3.6 Post-Buckling Analysis of a Hinged Spherical Shell 3.15
     - 3.3.7 Snap-Through and Snap-Back Analysis of a Shallow Cylindrical Shell 3.15
     - 3.3.8 Geometrically and Materially Nonlinear Analyses of a Clamped-Clamped Shallow Cylindrical Arch 3.16
     - 3.3.9 Geometrically and Materially Nonlinear Analyses of a Shallow Spherical Cap 3.16

4. IMPLEMENTATION OF HYPERELASTIC MATERIAL MODEL INTO THE 8-NODED NONLINEAR SOLID ELEMENT 4.1
   - 4.1 Rubber Materials and the Hyperelastic Material Model 4.1
   - 4.2 Theoretical Derivation of Stresses and Tangent Modulus Matrix for the Ogden's Hyperelastic Material Model 4.4
   - 4.3 Implementation of the Ogden's Hyperelastic Model into the VAST Program 4.7
   - 4.4 Numerical Verification 4.8
     - 4.4.1 Thick Hyperelastic Cylinder Under Internal Pressure 4.8
     - 4.4.2 Frequency Response Analysis of the Pre-Stressed Engine Mount Model 4.9

TABLE OF CONTENTS - Continued

5. CONCLUSIONS AND RECOMMENDATION FOR FURTHER WORK 5.1

6. REFERENCES 6.1

LIST OF TABLES

Table 2.1: Comparison of Critical Load Factors Predicted by the VAST Program Using the Coarse and Refined Meshes of the Block Rubber Engine Mount.... 2.8

Table 2.2: Comparison of the Analytical and Numerical Solutions to the Buckling Loads of an Axially Loaded Cantilever Beam.... 2.8

Table 2.3: Comparison of Vertical Displacements of Corner and Mid-side Nodes of the Simplified Engine Mount Model Predicted by Frequency Response Analyses with.... 2.9

Table 3.1: Patch Test Results of the Present 8-Noded Solid Element and the Exact Solutions. 3.17

Table 3.2: End Deflections of the Nearly Incompressible Beam Obtained by the 8-Noded Solid Element With Reduced Integration and Incompatible Modes. 3.17

Table 3.3: Buckling Loads of an Axially Loaded Slender Cantilever Beam Predicted by 3.18

Table 4.1: Material Constants Employed in the Analysis of the Thick Rubber Cylinder 4.11

LIST OF FIGURES

Figure 1.1: A Typical Engine Mount Used for the Experiment 1.4
Figure 1.2: Finite Element Model Utilized to Predict Dynamic Stiffness 1.5
Figure 1.3: Comparison of Measured and Predicted Dynamic Stiffness Properties of..... 1.6
Figure 1.4: Comparison of Measured and Predicted Dynamic Stiffness Properties 1.7

Figure 2.1: Finite Element Model Utilized to Predict Dynamic Stiffness Properties 2.10
Figure 2.2: Linear Buckling Modes of the Engine Mount Model 2.11
Figure 2.3: Refined Finite Element Mesh for the Engine Mount Model 2.13
Figure 2.4: Linear Buckling Modes of the Engine Mount Under Static Compression Predicted by the Refined Finite Element Model 2.14
Figure 2.5: Finite Element Mesh for Linear Buckling Analysis of a Cantilever Beam 2.15
Figure 2.6: Linear Buckling Modes of a Cantilever Beam Under Axial Compression 2.16
Figure 2.7: A Highly Simplified Finite Element Model of the Engine Mount, Including One 20-Noded Solid Element Representing the Visco-elastic Core Material 2.19
Figure 2.8: An 8-Noded Solid Element Mesh for the Visco-elastic Core of the Engine Mount 2.20
Figure 2.9: Time Histories of Vertical DisplacementsPredicted by the ANSYS Program 2.21
Figure 2.10: Time Histories of Vertical Displacement Predicted by the VAST Program for Linear Dynamic Analysis of the Engine Mount Under a Point Load. 2.22
Figure 2.11: Time Histories of Vertical Displacements at Nodes 57 and 21 Predicted by the ANSYS Program for Linear Dynamic Analysis of the Engine Mount Under a Uniform Pressure 2.23
Figure 2.12: Time Histories of Vertical Displacement Predicted by the VAST Program .. 2.24
Figure 2.13: Nonlinear Dynamic Responses of the Engine Mount Without Initial Static Compression Predicted by ANSYS Using the Mooney-Rivlin Hyperelastic Model 2.25
Figure 2.14 Load-Deflection Curves of the Engine Mount Under Static Compression 2.26
Figure 2.15: Nonlinear Dynamic Responses of the Engine Mount With Initial Static Compression Predicted by ANSYS Using the Mooney-Rivlin Hyperelastic Model 2.27

Figure 3.1: Problem Geometry, Mesh Layouts, Load Conditions and Boundary Constrains 3.19
Figure 3.2: Regular Mesh Utilized for Patch Test for the 8-Noded Solid Element in VAST 3.20
Figure 3.3: Distorted Mesh Utilized for Patch Test for the 8-Noded Solid Element in VAST 3.21
Figure 3.4: Problem Geometry, Load Conditions and Boundary Constrains for 3.22
Figure 3.5: 8-Noded Solid Element Mesh for Bending Analysis of the 3.23
Figure 3.6: 8-Noded Solid Element Mesh for Linear Buckling Analysis of 3.24

LIST OF FIGURES - Continued

Figure 3.7: Buckling Mode Shapes of the Axial Loaded Cantilever Beam Predicted by the 3.25
Figure 3.8: Problem Geometry, Load Conditions and Boundary Constrains for Nonlinear 3.28
Figure 3.9: Solid Element Meshes for Nonlinear Analyses of the Simply-Supported..... 3.29
Figure 3.10: Comparison of Load-Center Deflection Curves of the Square Plate..... 3.31
Figure 3.11: Comparison of Load-Center Deflection Curves of the Square Plate Obtained..... 3.33
Figure 3.12: Problem Geometry, External Load and Boundary Conditions for Large 3.35
Figure 3.13: Finite Element Meshes for Large Displacement Analysis of the 45° Bend.... 3.36
Figure 3.14: Comparison of Non-dimensionalized Load-Tip Deflection Curves of the..... 3.37
Figure 3.15: Problem Geometry, External Load and Boundary Conditions for..... 3.38
Figure 3.16: Finite Element Meshes for Post-Buckling Analysis of the Spherical Shell.... 3.39
Figure 3.17: Comparison of Load-Center Deflection Curves of the Spherical Shell..... 3.40
Figure 3.18: Problem Geometry and External Load for Snap-Through and Snap-Back 3.41
Figure 3.19: Solid Element Meshes for Post-Buckling Analysis of the Hinged Cylindrical 3.42
Figure 3.20: Comparison of Load-Center and Edge Deflection Curves of the Thicker..... 3.43
Figure 3.21: Comparison of Load-Center and Edge Deflection Curves of the Thinner 3.44
Figure 3.22: Problem Geometry, External Load and Boundary Conditions for General.... 3.45
Figure 3.23: Finite Element Meshes for General Nonlinear Analysis of the Cylindrical Arch. 3.46
Figure 3.24: Comparison of Load-Center Deflection Curves of the Cylindrical 3.47
Figure 3.25: Problem Geometry and External Loading Condition for Geometrically and . 3.48
Figure 3.26: Finite Element Meshes for Nonlinear Analysis of the Shallow Spherical Shell. 3.49
Figure 3.27: Comparison of Load-Center Deflection Curves of the Shallow Spherical Shell 3.50
Figure 3.28: Comparison of Load-Center Deflection Curves of the Shallow Spherical Shell 3.51

Figure 4.1: Comparison of Treloar's Experimental Data with the Predictions of the neo-Hookean (----), Mooney-Rivlin (-.-.-) and Ogden's (—) Strain Energy Functions 4.12
Figure 4.2: Coarse Finite Element Mesh for Plane Strain Expansion of a Thick Rubber 4.14
Figure 4.3: Comparison of the Reference Solution and the VAST Predictions..... 4.15
Figure 4.4: Fine Finite Element Mesh for Plane Strain Expansion of a Thick Rubber Cylinder Under Internal Pressure. (a) Boundary Constraints and (b) Loading Condition. 4.16
Figure 4.5: Comparison of the Reference Solution and the VAST Predictions..... 4.17
Figure 4.6: Comparison of the Reference Solution and the VAST Predictions Using 4.18
Figure 4.7: A Simplified Engine Mount Model Used for Frequency Response 4.19

LIST OF FIGURES - Continued

Figure 4.8: Comparison of Undamped Frequency Responses of the Engine Mount 4.20
Figure 4.9: Comparison of Damped Frequency Responses of the Engine Mount 4.21
Figure 4.10: Load-Deflection Curves for Nonlinear Static Analysis of the Engine Mount 4.22

1. INTRODUCTION

Reduction of noise and vibration levels generated by machinery on board ships is especially important in the naval context. One way to achieve this noise reduction is to design and install highly efficient vibration isolation systems, which often involve visco-elastic materials. In order to assess the efficiency of these vibration isolation systems, quantitative data on the acoustic stiffness of these systems must be obtained. Dynamic tests can be performed to experimentally measure the sound transfer functions of various vibration isolation mounts under compressive and shear forces. From these transfer functions, the acoustic stiffnesses can be derived [1]. However, for large engine mounts involving multiple degrees-of-freedom and large initial static loads, the experimental measurements are often difficult and expensive to conduct.

An alternative method for characterizing the dynamic behavior of vibration isolation systems is to perform direct frequency response analyses using frequency-dependent stiffness and damping properties of the mount material, which can be measured relatively easily from small samples. Through contracts from DREA, a finite element based frequency response analysis capability has been developed at Martec Limited over the past several years [2-5]. By solving the discretized equations of motion directly in the frequency domain, this capability can handle complex and arbitrarily frequency-dependent material properties. The current version of VAST provides options for computing strain energy ratios and system loss factors, solving complex eigenvalue problems, treating complex, frequency-dependent Poisson's ratio, and specifying very general external load vectors. This capability has been verified by extensive numerical experiments.

DREA had recently utilized the VAST program to predict the acoustic stiffness behavior of a block rubber engine mount as shown in Figure 1.1, and compared the numerical results with the experimental measurement of the Netherlands Navy [1]. This mount was composed of a pair of steel plates and a very thick layer of constrained rubber material. Before the application of the small amplitude dynamic excitation, this engine mount was loaded by a static compressive force which resulted in a 12% reduction on the total height of the mount. In the finite element analyses conducted at DREA, a relatively coarse mesh of the 20-noded solid element was employed to

model the engine mount. This mesh is displayed in Figure 1.2. The frequency-dependent stiffness and damping properties of the visco-elastic core material measured by the DREA Dockyard Lab [6] were used in these analyses.

The initial VAST predictions, in which the effect of the static compression was completely ignored, were in reasonable agreement with the experimental results in both compression and shear as shown in Figures 1.3 and 1.4. To obtain more accurate numerical solutions, two additional direct frequency response analyses were conducted. In the first analysis, the deformed geometry of the engine mount caused by the static compression was utilized in the computation of the element stiffness and mass matrices, whereas in the second analysis, both deformed geometry and geometric stiffness matrix were considered. Numerical results from these analyses indicated that the inclusion of the deformed geometry alone improved the accuracy of the VAST solution, however, once the geometric stiffness matrix was included into the analysis, the VAST direct frequency response results became too soft, resulting in a significant underestimation of the acoustic stiffness of the system.

The objective of the present study is to further investigate this numerical problem, identify the defects in the current element and geometric stiffness matrices of the solid element, and implement enhanced element formulation which is able to produce correct numerical solutions for pre-stresses engine mount systems. This objective was achieved in three steps.

First of all, a comprehensive study of the engine mount model was carried out. Linear buckling analysis of the engine mount revealed that at least the first 20 critical loads were less than the static compressive force, suggesting that the addition of the geometric stiffness matrix would reduce the overall stiffness of the mount. In order to verify the correctness of the geometric stiffness matrix of the 20-noded solid element, linear buckling problem of a cantilever beam under axial compression was considered. The eigenvalues and eigenvectors predicted by VAST were in excellent agreement with the theoretical results. The direct frequency response results obtained by VAST and ANSYS were then compared with and without the geometric stiffness matrix. Close agreement was observed in both cases. A nonlinear static analysis was then performed using ANSYS to characterize the large deformation of the mount under static compression. The

Mooney-Rivlin hyperelastic material model was utilized to represent the rubber core. Because the frequency-response analysis option was not available for the hyperelastic solid element in ANSYS, nonlinear dynamic responses of the mount were obtained in time domain through direct time integration. A stiffening effect of the pre-stress was demonstrated in these nonlinear solutions. These results not only verified the correctness of the VAST element, but also clearly indicated the need of a hyperelastic material model in VAST. The details of the analyses and results are presented in Chapter 2 of the present report.

From a quite extensive survey of the state-of-the-art literatures on large strain finite element formulations, it was concluded that the co-rotational procedure proposed by Crisfield and co-workers [7-11] fitted into the overall code structure of the VAST program very well. Besides its capability for treating arbitrarily large rotations, this nonlinear formulation for 3D continua used co-rotational Biot stress and strain measures, which simplified the implementation of hyperelastic material models. However, the algorithm for calculating rigid body rotations was developed based on an assumption that the deformation gradient was uniform over the solid element. This assumption restricted the application of the co-rotational formulation to the lower-order 8-noded solid elements. In this report, the theoretical background and computer implementation of the co-rotational formulation is described in Chapter 3, and the hyperelastic material model is incorporated into this element in Chapter 4. Both chapters include extensive numerical studies for verification purposes.

Conclusions and recommendations for further work are presented in Chapter 5.

Figure 1.1: A Typical Engine Mount Used for the Experiment

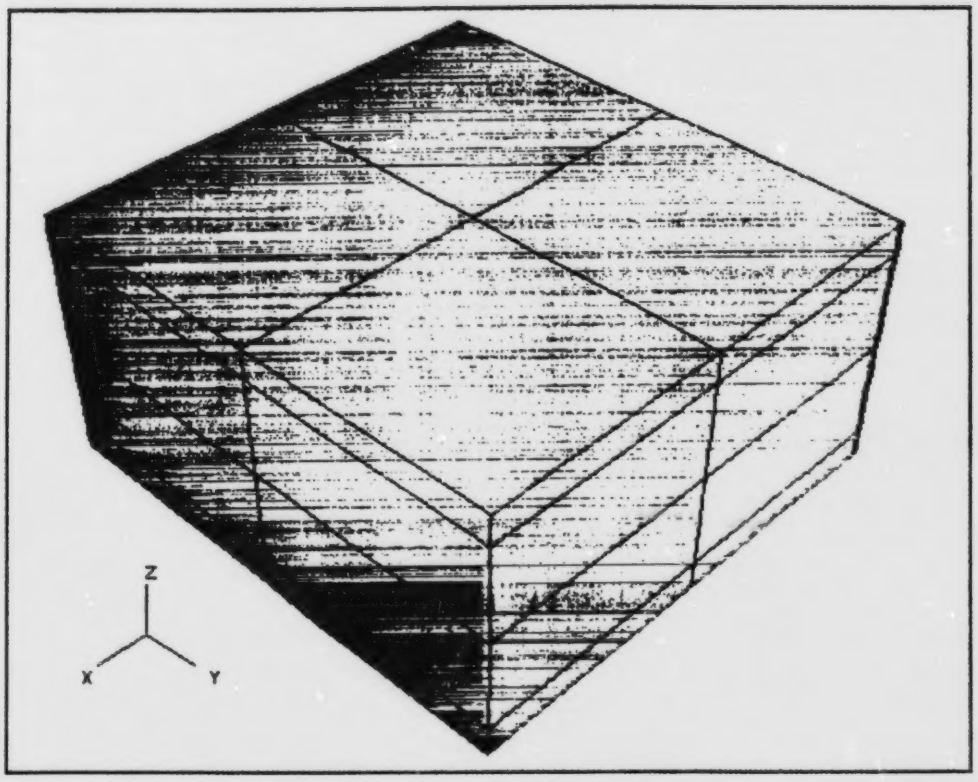

Figure 1.2: Finite Element Model Utilized to Predict Dynamic Stiffness Properties of the Engine Mount Model

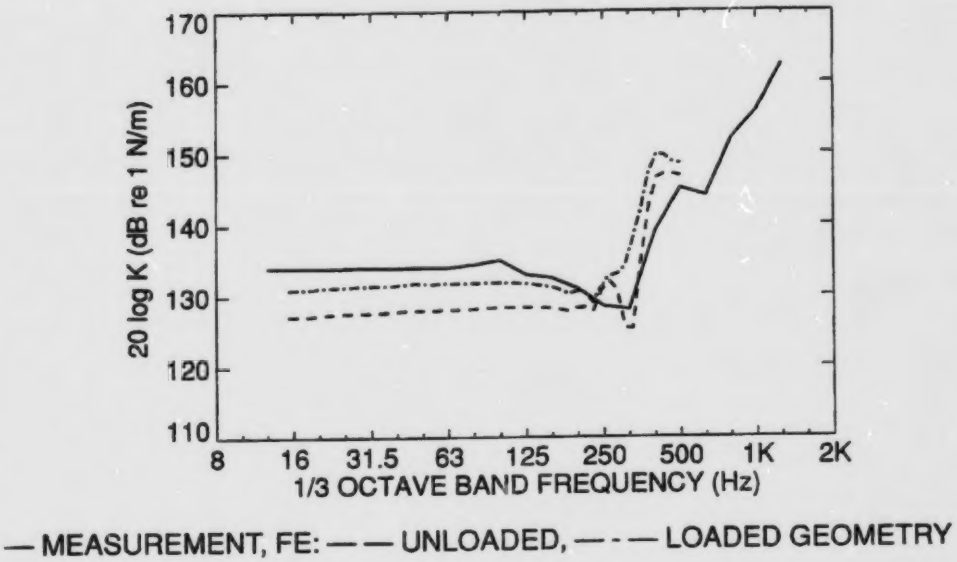

Figure 1.3: Comparison of Measured and Predicted Dynamic Stiffness Properties of the Engine Mount in Compression

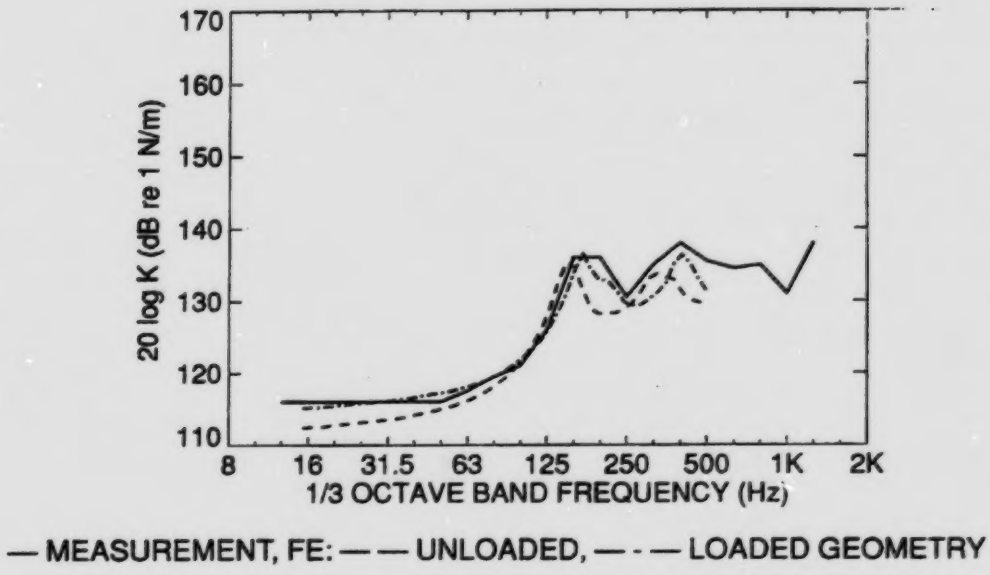

Figure 1.4: Comparison of Measured and Predicted Dynamic Stiffness Properties of the Engine Mount in Shear

2. NUMERICAL ANALYSES OF THE BLOCK RUBBER ENGINE MOUNT

As mentioned in the previous chapter, the present work was motivated by the direct frequency response analysis results of a pre-stressed block rubber engine mount obtained by DREA using the VAST finite element program. It had been found that if the frequency response analyses were carried out using the original undeformed geometry of the engine mount, VAST predicted an acoustic stiffness which was in reasonable agreement with the experimental measurement. However, when the geometric stiffness matrix, evaluated using the stresses caused by the static compression, was included, VAST solutions became significantly softer than the measured data, resulting in a serious underestimation of the acoustic stiffness.

To investigate the effect of the geometric stiffness matrix on the predicted dynamic behavior of the engine mount model, an extensive numerical study was first carried out in the present project.

2.1 Buckling Analyses of the Engine Mount Model

Linearized buckling analysis is a good way to verify the geometric stiffness formulation of an element. The geometric stiffness matrix implemented in the 20-noded solid element in VAST was based on the standard formulation given as follows [12]:

$$\mathbf{K}_G = \int_v \mathbf{B}_{NL}^T \hat{\mathbf{S}} \mathbf{B}_{NL} \, dV \tag{2.1}$$

In this equation, $\mathbf{B}_{NL}$ denotes the displacement derivative matrix defined as:

$$\{u_{,x} \; u_{,y} \; u_{,z} \; v_{,x} \; v_{,y} \; v_{,z} \; w_{,x} \; w_{,y} \; w_{,z}\}^T = \mathbf{B}_{NL} \; \mathbf{U} \tag{2.2}$$

where ( ), denotes the partial derivative, and $\hat{\mathbf{S}}$ is a block diagonal stress matrix defined as:

$$\hat{\mathbf{S}} = [\text{diag } \mathbf{S}] = \begin{bmatrix} \mathbf{S} & 0 & 0 \\ 0 & \mathbf{S} & 0 \\ 0 & 0 & \mathbf{S} \end{bmatrix} \tag{2.3}$$

where **S** is a 3x3 matrix containing the initial stress components:

$$\mathbf{S} = \begin{bmatrix} \sigma_x & \hat{\sigma}_{xy} & \hat{\sigma}_{xz} \\ \hat{\sigma}_{xy} & \sigma_y & \hat{\sigma}_{yz} \\ \hat{\sigma}_{xz} & \hat{\sigma}_{yz} & \sigma_z \end{bmatrix} \tag{2.4}$$

In the present study, buckling analyses were performed using the static compressive load as a reference load vector. The coarse 20-noded solid element mesh generated by DREA (shown in Figure 2.1) was first utilized in these eigenvalue analyses. In this finite element model, the in-plane dimensions of the mount were 0.229m x 0.241m. The thicknesses of the plate and core were 0.015m and 0.096m, respectively. The material properties of steel adopted in these analyses included Young's modulus $E=0.207\text{x}10^{12}$ N/m^2, Poisson's ratio $\nu=0.3$ and mass density $\rho=0.787\text{x}10^4$ kg/m^3. For the rubber layer, material properties measured on the initial undeformed configuration were used. They included Young's modulus $E=0.216\text{x}10^7$ N/m^2, Poisson's ratio $\nu=0.47$ and mass density $\rho=0.107\text{x}10^4$ kg/m^3. The amplitude of the static compressive load applied on the engine mount was 37000 N.

The first 10 buckling loads predicted by the eigenvalue analysis are summarized in Table 2.1 and several typical buckling mode shapes are displayed in Figure 2.2. It is interesting to note that for all these modes, the predicted critical load factors (eigenvalues) were consistently positive and less than unity, suggesting that the inclusion of the geometric stiffness did reduce the overall stiffness of the engine mount structure. By examining the buckling mode shapes, it is readily recognized that these modes were consistently characterized by large shear deformations of the core. This is probably due to the relatively small shear modulus to bulk modulus ratio of the rubber materials.

In order to eliminate the possibility that the stress softening effect observed earlier was caused by the coarseness of the finite element mesh, a refined mesh had been created as shown in Figure 2.3 and used for buckling analysis. The first 10 eigenvalues obtained using the fine mesh were still positive and less than unity as presented in Table 2.1, and the predicted mode shapes still contained large shear deformations as displayed in Figure 2.4.

In order to verify the VAST predictions, other commercial finite element programs, ANSYS and NASTRAN, were also used. ANSYS predicted critical load factors smaller than one, which was consistent with the VAST solutions. However, NASTRAN failed to provide any results due to an ill-conditioning problem related to the geometric stiffness matrix.

To further verify the geometric stiffness matrix of the 20-noded solid element, we considered the buckling problem of a cantilevered beam column loaded axially at the free end. This problem was selected because of the availability of the analytical solutions [13]. The length of the beam was taken as 50m and the dimensions of the cross-section was 1m x 1m. The material properties utilized were $E=2.0\times10^{11}$ N/m^2 and $\nu=0.3$. The finite element mesh is shown in Figure 2.5 which contained 20 solid elements. The first 16 buckling loads of the beam column predicted by VAST are compared with the analytical solutions in Table 2.2 with excellent agreement. It should be noticed that repeated eigenvalues existed in the finite element solution. This is because the beam column can buckle into two orthogonal planes passing through the Z-axis. A number of buckling mode shapes predicted by VAST are shown in Figure 2.6 which are also in excellent agreement with the analytical solutions presented in reference [13]. This excellent agreement between the finite element and analytical solutions to the beam buckling problem confirmed the correctness of the geometric stiffness matrix in the 20-noded solid element.

2.2 Direct Frequency Response Analysis of the Engine Mount Model

Following the linear buckling analyses, direct frequency response analyses of the engine mount were reconsidered. To avoid potential ill-conditioning problems associated with the huge difference between the stiffnesses of the steel plates and rubber core material, a highly simplified finite element model of the engine mount, which included only one solid element representing the

rubber material, was employed as shown in Figure 2.7. The vertical displacement at the bottom surface of the rubber block was constrained and minimum boundary conditions were applied in the in-plane directions. The upper surface was loaded by uniform pressure. The frequency-dependent material properties of the visco-elastic core were not used in these frequency response analyses since such a capability was not available in the ANSYS program.

Both VAST and ANSYS frequency response results were obtained with and without the effect of the static compression included. The magnitudes of the vertical displacements at the corner and mid-side nodes predicted by both finite element programs are compared in Table 2.3. Consistent with the VAST predictions, ANSYS also produced a softer response after the inclusion of the geometric stiffness matrix corresponding to the static compression. The agreement of the VAST and ANSYS solutions again verified the correctness of the geometric stiffness formulation implemented in the 20-noded solid element in the VAST program.

2.3 Nonlinear Static and Dynamic Analyses of the Engine Mount

The results of linear buckling and frequency response analyses presented in the preceding sections suggested that to accurately characterize the dynamic behavior of the engine mount, an appropriate hyperelastic material model must be utilized. Because the ADINA program was not available to Martec during the course of the present study, the ANSYS program, which provides the Mooney-Rivlin material model, had been used to carry out the nonlinear analyses. This well-known hyperelastic material model contained two material constants, which can be calculated by fitting the material test data. Because material test data for the engine mount material were not available at the time of the analysis, a set of typical material constants for rubbers, C_1=0.552 MPa and C_2=0.138MPa, were used. A Poisson's ratio of 0.49 was employed to model the near incompressibility of the rubber material. However, it should be realized that the values of material constants used in the nonlinear analyses were not important for the current purposes.

Since the only three-dimensional hyperelastic solid element provided in ANSYS was an 8-noded element, a new finite element mesh was created using the lower-order solid elements as shown in Figure 2.8. Again, to avoid the ill-conditioning problem, only the rubber material layer

was included in this new mesh. The bottom of the rubber block was fully constrained against translations in the Z-direction, however, minimum constrains were used in the in-plane directions.

Because the hyperelastic solid element in ANSYS only worked for full (combined geometrically and materially) nonlinear situation, direct frequency response analysis, which operated on a set of linearized equations of motion, cannot be performed using this element. To investigate the effect of the static load on the dynamic characteristics of the engine mount, the Scientific Authority has suggested that time domain nonlinear dynamic analyses be performed under sinusoidal external loading with and without the initial static compression.

To become familiar with the input data format of the ANSYS program for time history calculations, two linear dynamic analyses of the engine mount model were first conducted, and the ANSYS predictions were compared with the VAST solutions. In the first analysis, a concentrated dynamic load defined as:

$$F(t) = 100 \sin(100\pi t) \qquad t \in [0,0.04] \tag{2.5}$$

was applied at the center of the upper surface. The time history of the vertical displacements at the center node 57 and the corner node 21 obtained by using ANSYS are displayed in Figure 2.9. The VAST solutions to the same problem are shown in Figure 2.10. The ANSYS and VAST results are in very close agreement. Since a smaller time step size was utilized in the VAST analysis, more details of the dynamic response were modeled in the VAST solution.

In the second dynamic analysis, a uniform pressure load was applied on the top surface of the rubber block as:

$$P(t) = 1000 \sin(100\pi t) \qquad t \in [0,0.08] \tag{2.6}$$

The time history of the vertical displacements predicted by ANSYS and VAST are presented in Figures 2.11 and 2.12, respectively. Again, excellent agreement between these solutions are observed.

We then moved on to compute the nonlinear dynamic response of the engine mount without the static compression. Using the uniform dynamic pressure load given in Equation (2.6), nonlinear responses were obtained for the first four cycles. The vertical displacements at the center node 57 and the corner node 21 on the upper surface of the rubber block are presented in Figure 2.13, as darker and lighter solid lines, respectively. Comparing Figures 2.13 and 2.11, it is readily realized that the nonlinear dynamic responses are quite different from the linear ones.

The nonlinear static response of the engine mount under the initial compression was now computed up to a total height reduction of 33%. The load-displacement curves are shown in Figure 2.14 where the maximum displacement components in each direction are displayed. The load-vertical deflection curve was almost linear, similar to the test results obtained at the DREA Dockyard lab [6]. However, it was still noticeable that the structural response became progressively stiffer with the increase of the static load. This stiffening effect was caused by the nonlinear material property rather than the geometric nonlinearity in the problem.

Although the dynamic solution of the rubber block with only the sinusoidal excitation was relatively straightforward using ANSYS, difficulties were experienced when attempting to take the static compression into account. The ANSYS program provided the capability to include static and dynamic loads in the same analysis by arranging them into separate time blocks. The inertial effect can be turned on and off independently in these blocks. In the first attempt for nonlinear dynamic analysis with static compression, the inertial effect was turned off in the first block for nonlinear static loading, and turned back on in the subsequent time blocks for dynamic analyses. However, when the dynamic effect was activated in the second time block, an initial velocity vector was automatically calculated based on the last two solution points in the first (static) time block and prescribed onto the structure. This initial velocity vector caused significant noise in the dynamic response, which makes the direct comparison of the solutions with and without static load impossible.

As it appeared that ANSYS did not provide an option for resetting the initial velocities at the beginning of the second time block, two analysis approaches have been taken in the present nonlinear dynamic analysis to minimize the effect of the non-zero initial velocity. First of all, the

pseudo-time period, over which the ramp static load was applied, was increased to a few magnitudes larger than the dynamic time scale. However, numerical results indicated that this was unable to completely eliminate the effect of the unwanted initial velocity. In the second approach, an additional time block with constant static load was inserted between the end of the ramp application of the static load and the onset of the dynamic load. This additional constant load time block not only produced a zero initial velocity vector, but also decreased the level of out-of-balance force resulting from the nonlinear static analysis. Mathematically, the time function of the applied pressure load in this problem can be expressed as:

$$P(t) = \begin{cases} P_0\, t/t_1 & t \in [0, t_1] \\ P_0 & t \in [t_1, t_2] \\ P_0 + P_1 \sin[100\pi(t - t_2)] & t \in [t_2, t_3] \end{cases} \qquad (2.7)$$

where P_0 = 1675000 Pa, P_1 = 1000 Pa, t_1 = 0.01 Sec., t_2 = 0.09 Sec., and t_3 = 0.17 Sec. Using this pressure time function, nonlinear dynamic results were obtained successfully for the first four cycles of dynamic loading. The vertical dynamic displacements at the center (node 57) and corner (node 21) of the top surface are displayed in Figure 2.15, where the static solution was also included as dash-double dot line.

Comparing the first minimum and maximum displacements presented in Figures 2.13 and 2.15, it is readily recognized that the application of the static load reduced the amplitude of the forced vibration of the rubber block under the same dynamic load. In other words, the presence of the static compression increased the dynamic stiffness of the rubber block. This result is opposite to the predictions of the linear finite element theory presented earlier in this report. The numerical results obtained in the present investigation clearly indicated that a hyperelastic material model is required for accurate characterization of dynamic behavior of the rubber engine mount structure.

Table 2.1: Comparison of Critical Load Factors Predicted by the VAST Program Using the Coarse and Refined Meshes of the Block Rubber Engine Mount

Mode No.	Critical Load Factors	
	Coarse Mesh	Fine Mesh
1	0.66525	0.49903
2	0.68247	0.62009
3	0.71702	0.64500
4	0.80591	0.82075
5	0.80603	0.82076
6	0.84851	0.84016
7	0.85102	0.84084
8	0.87241	0.84144
9	0.87708	0.84170
10	0.91730	0.86381

Table 2.2: Comparison of the Analytical and Numerical Solutions to the Buckling Loads of an Axially Loaded Cantilever Beam

Mode No.	Buckling Loads (MN)	
	Analytical Solution [13]	Numerical Solution
1	16.449	16.609
2	16.449	16.609
3	148.04	149.26
4	148.04	149.26
5	411.23	413.68
6	411.23	413.68
7	806.02	808.71
8	806.02	808.72
9	1332.4	1332.0
10	1332.4	1332.0
11	1990.4	1979.9
12	1990.4	1979.9
13	2779.9	2748.2
14	2779.9	2748.2
15	3701.1	3637.7
16	4927.5	4649.4

Table 2.3: Comparison of Vertical Displacements of Corner and Mid-side Nodes of the Simplified Engine Mount Model Predicted by Frequency Response Analyses with The VAST and ANSYS Programs

Excitation Frequency (Hz)	Corner Node (1)		Mid-side Node (4)	
	VAST	ANSYS	VAST	ANSYS
Without Static Compression				
16	0.0286	0.02860430	0.0390	0.03846399
32	0.0332	0.03356803	0.0319	0.03232089
48	0.0364	0.03670065	0.0345	0.03448836
64	0.0435	0.04416800	0.0415	0.04147508
80	0.0615	0.06326475	0.0604	0.05990733
With Static Compression				
16	0.0620	0.06455658	0.0608	0.05960749
32	0.0601	0.05979897	0.0526	0.04947254
48	0.0612	0.07379876	0.0670	0.06076606
64	0.1090	0.10576150	0.0866	0.08737360
80	0.2580	0.24397360	0.1740	0.20174430

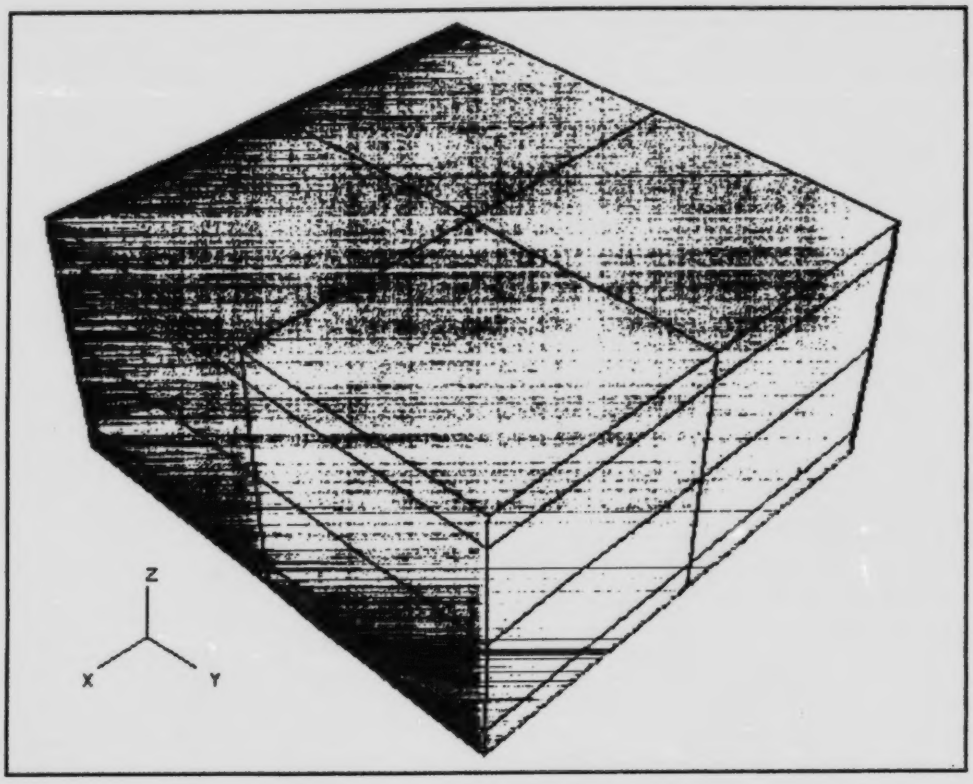

Figure 2.1: Finite Element Model Utilized to Predict Dynamic Stiffness Properties of the Engine Mount Model

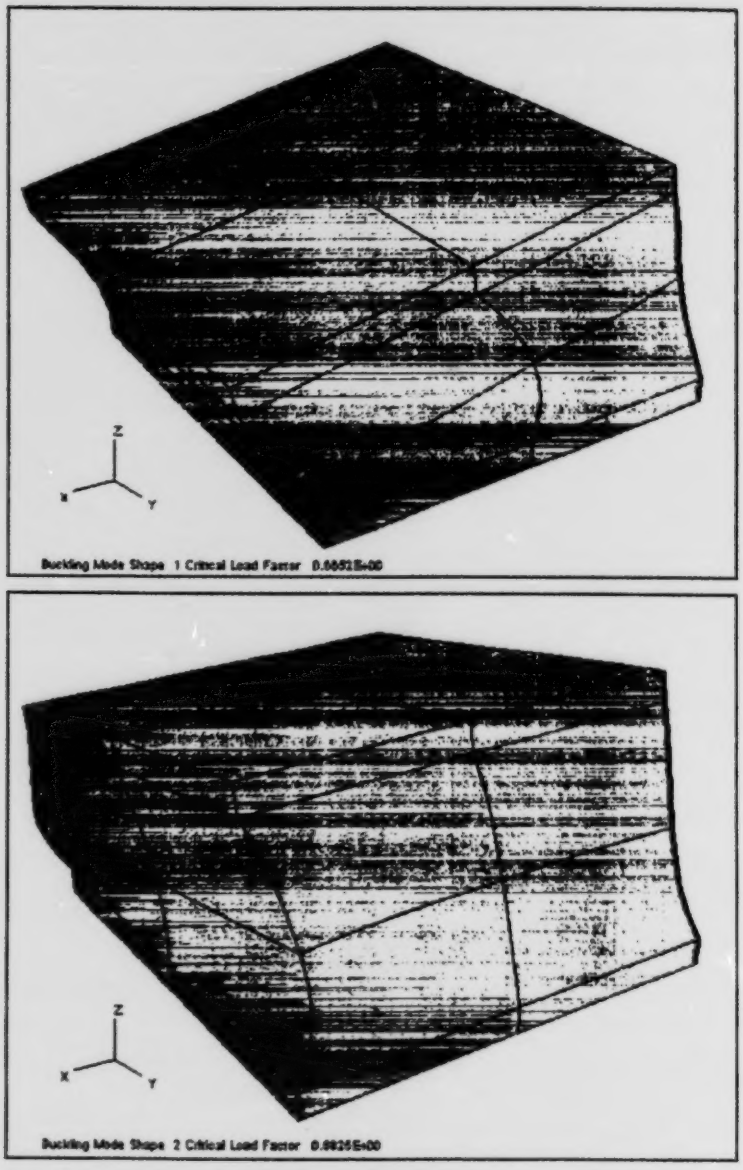

Figure 2.2: Linear Buckling Modes of the Engine Mount Model Under Static Compression

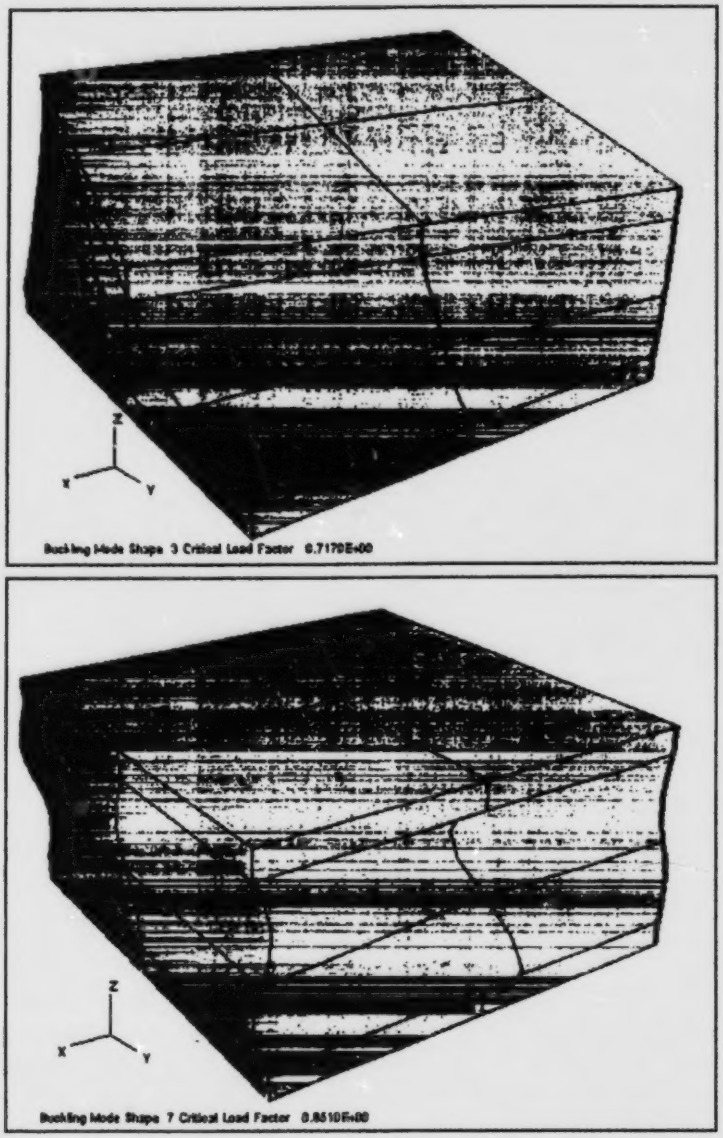

Figure 2.2 (continued): Linear Buckling Modes of the Engine Mount Model Under Static Compression

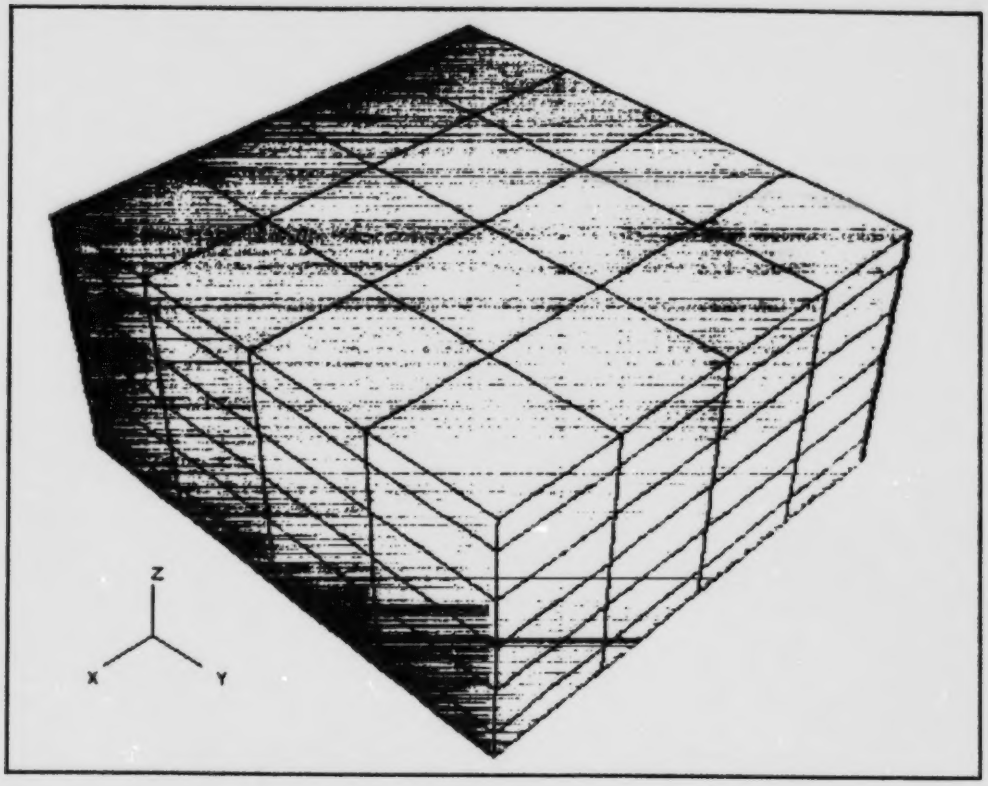

Figure 2.3: Refined Finite Element Mesh for the Engine Mount Model

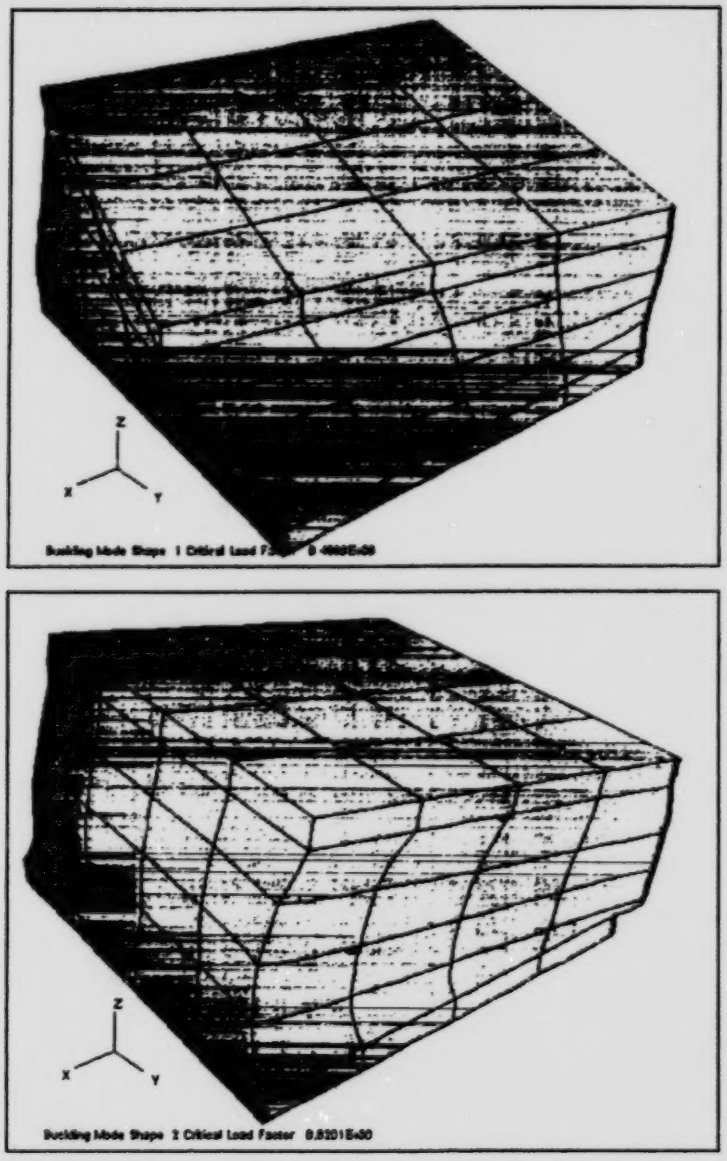

Figure 2.4: Linear Buckling Modes of the Engine Mount Under Static Compression Predicted by the Refined Finite Element Model

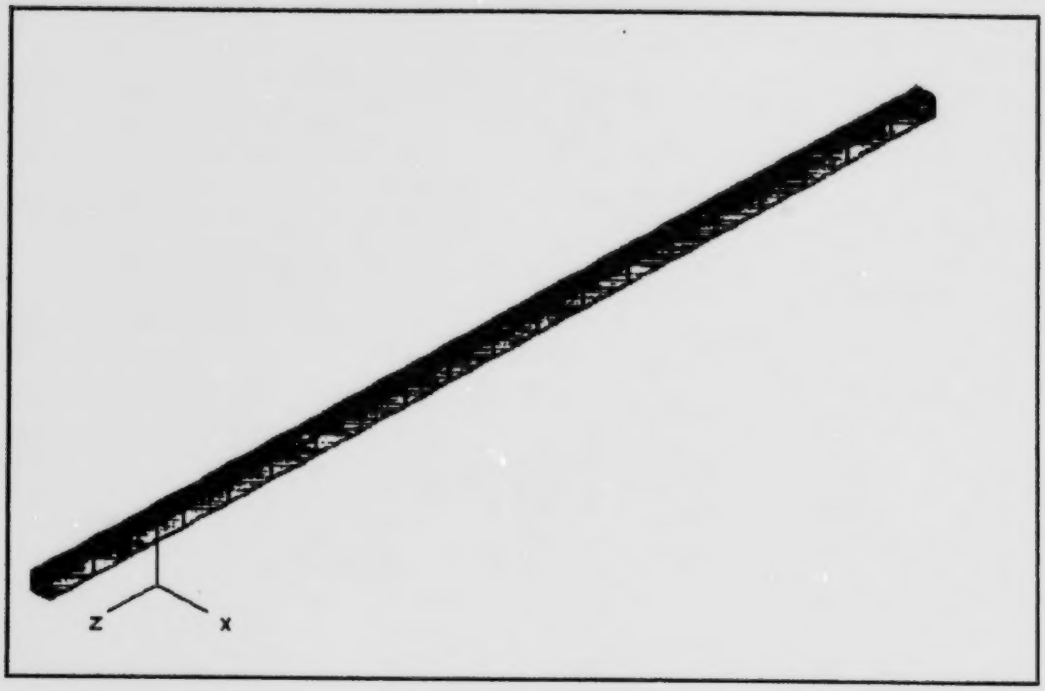

Figure 2.5: Finite Element Mesh for Linear Buckling Analysis of a Cantilever Beam Under Axial Compression

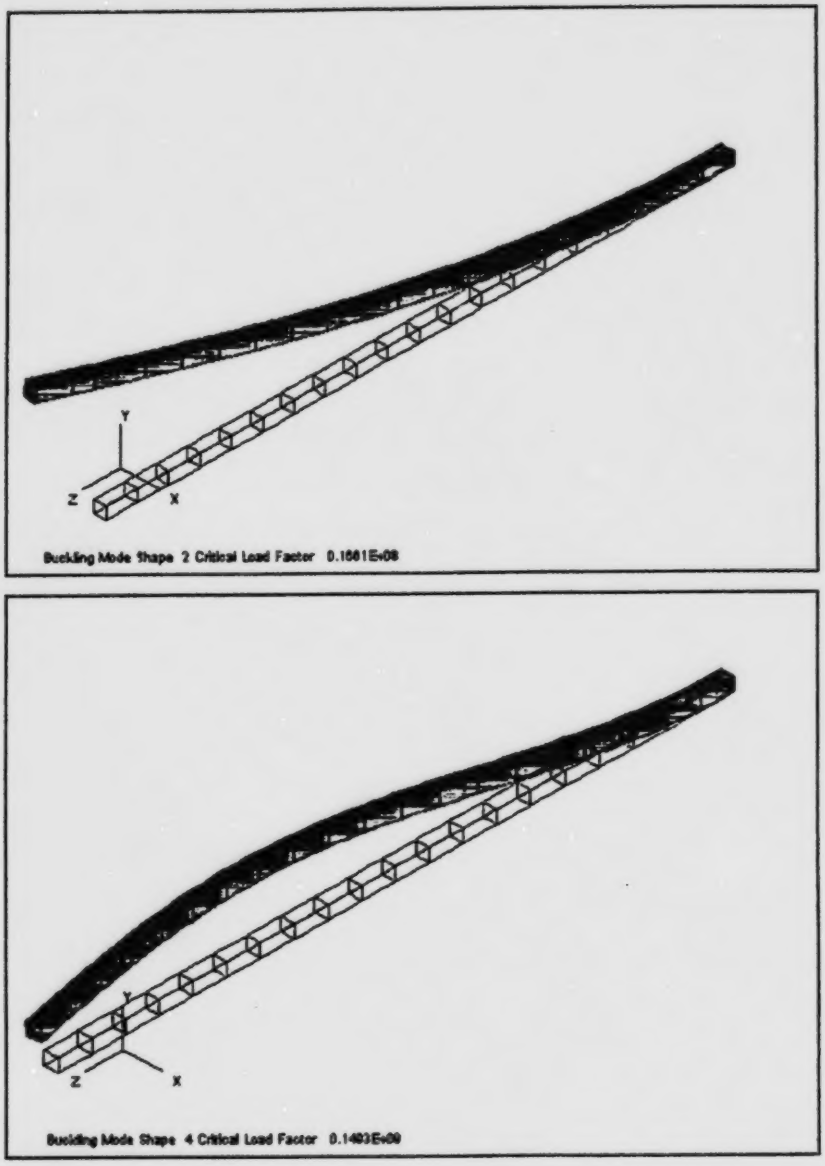

Figure 2.6: Linear Buckling Modes of a Cantilever Beam Under Axial Compression Predicted by the 20-Noded Solid Elements

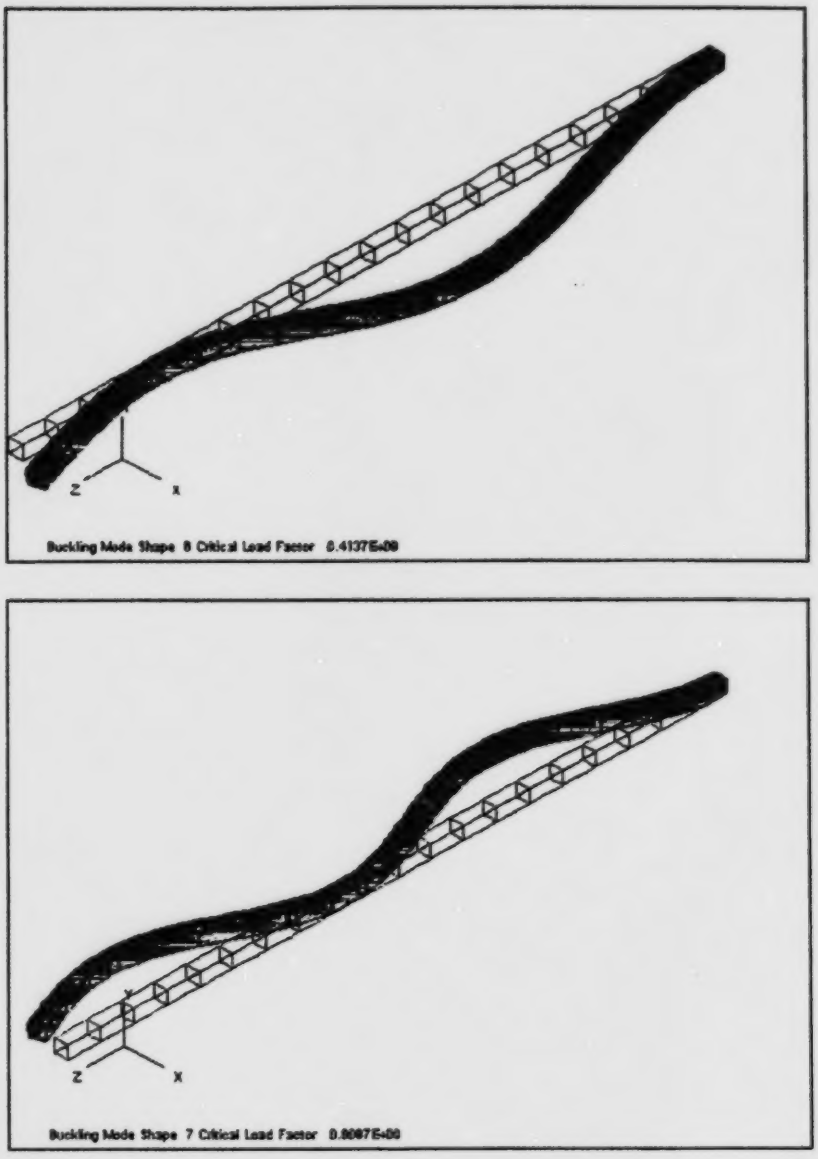

Figure 2.6 (continued): Linear Buckling Modes of a Cantilever Beam Under Axial Compression Predicted by the 20-Noded Solid Elements

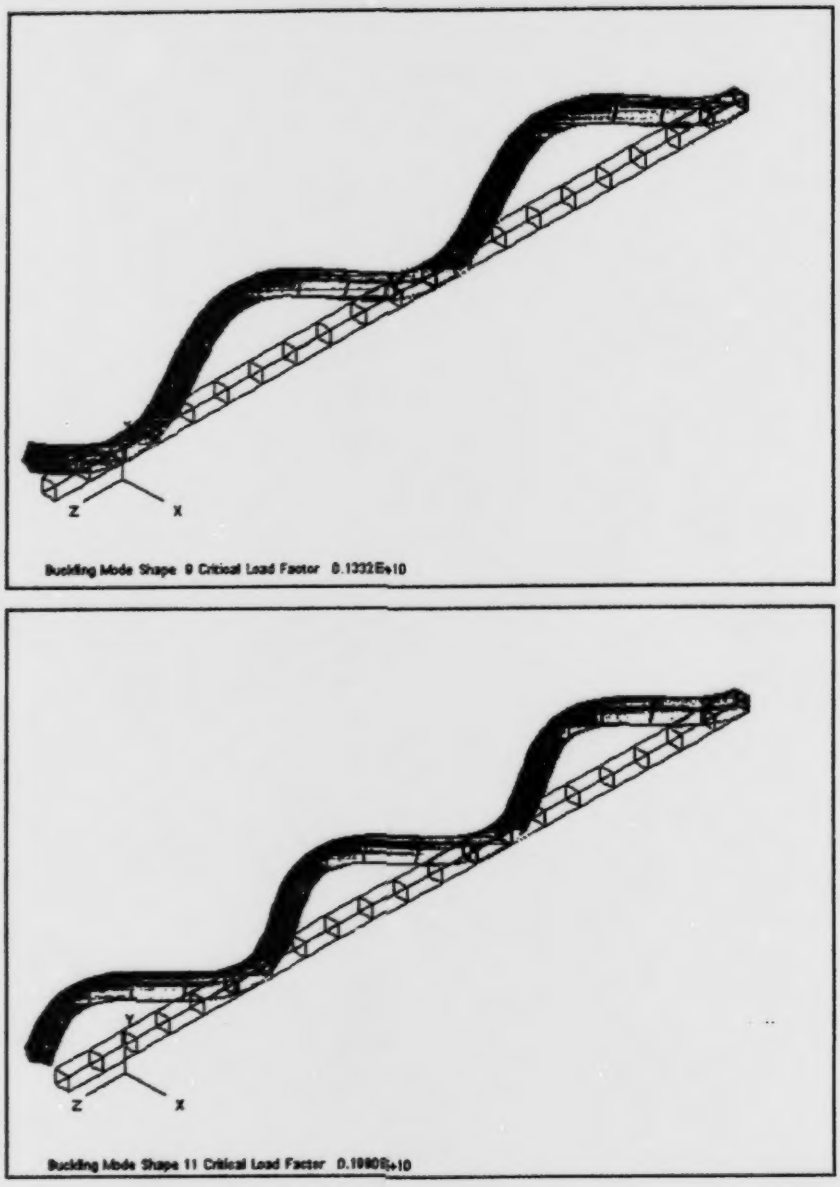

Figure 2.6 (continued): Linear Buckling Modes of a Cantilever Beam Under Axial Compression Predicted by the 20-Noded Solid Elements

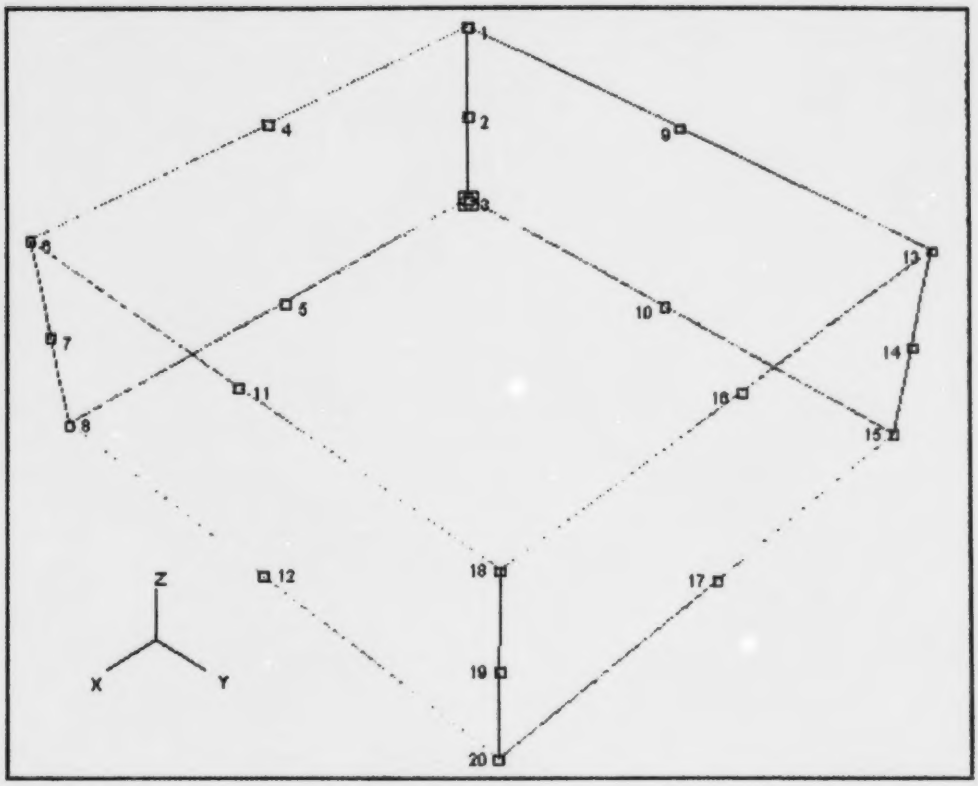

Figure 2.7: A Highly Simplified Finite Element Model of the Engine Mount, Including One 20-Noded Solid Element Representing the Visco-elastic Core Material

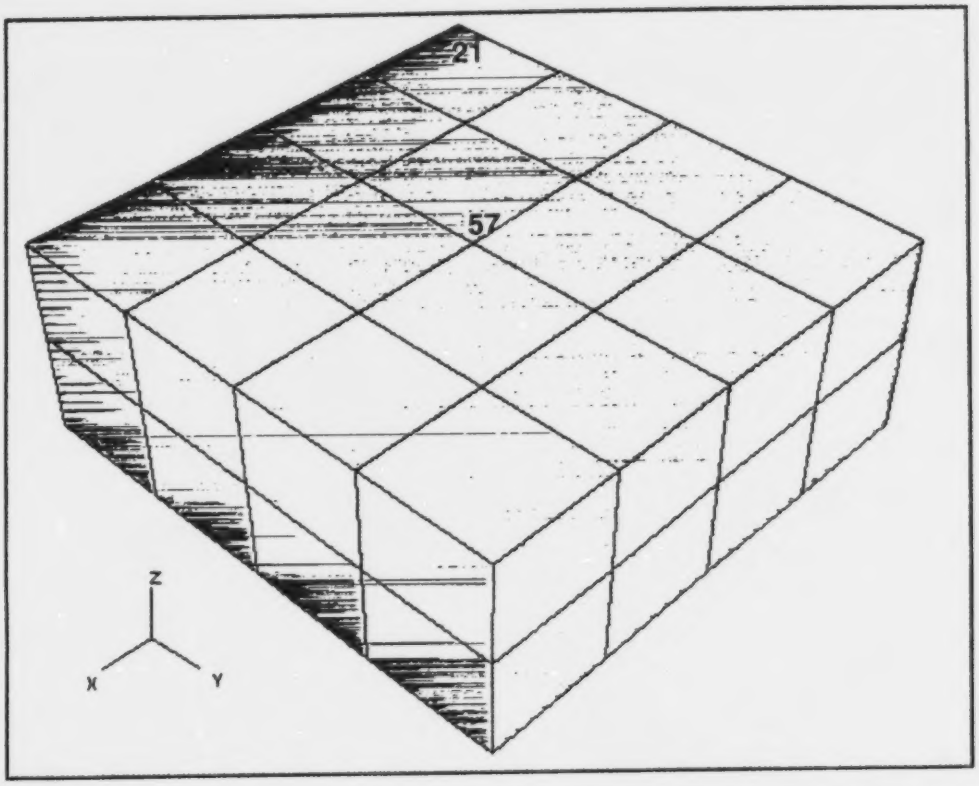

Figure 2.8: An 8-Noded Solid Element Mesh for the Visco-elastic Core of the Engine Mount.

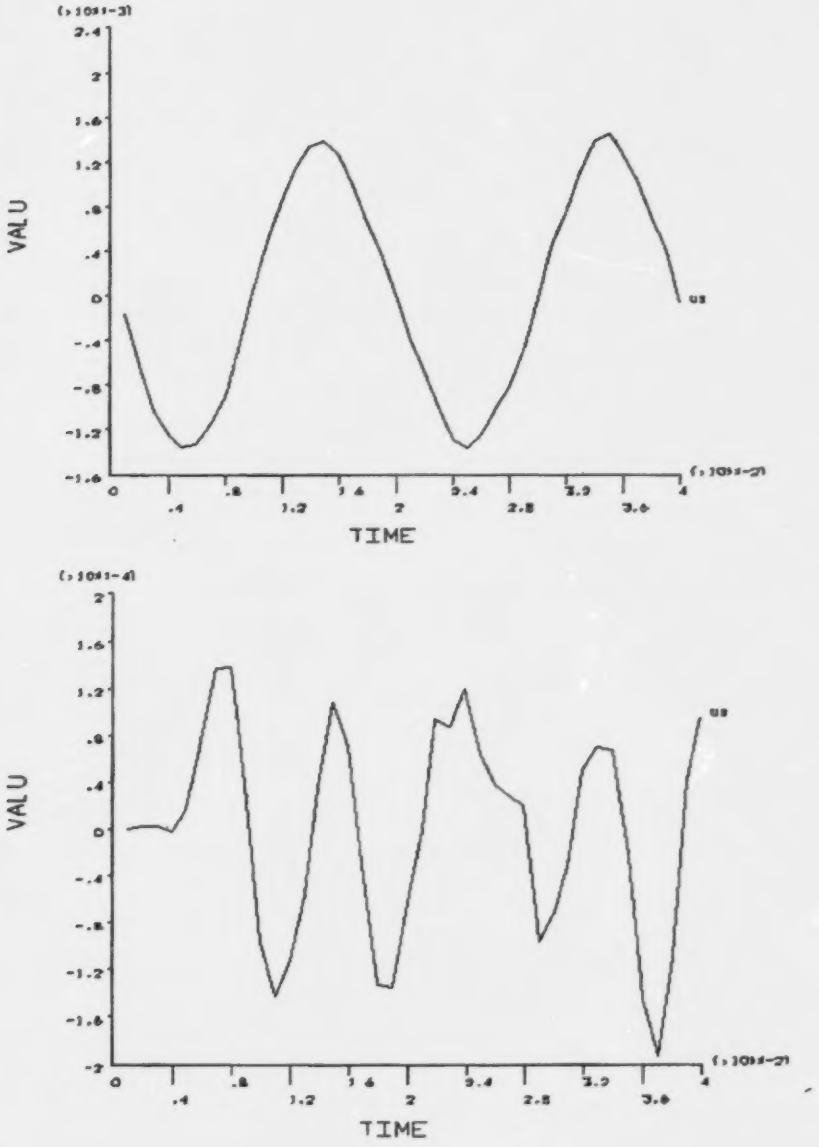

Figure 2.9: Time Histories of Vertical DisplacementsPredicted by the ANSYS Program for Linear Dynamic Analysis of the Engine Mount Under a Point Load.
(a) Center Node 57; (b) Corner Node 21.

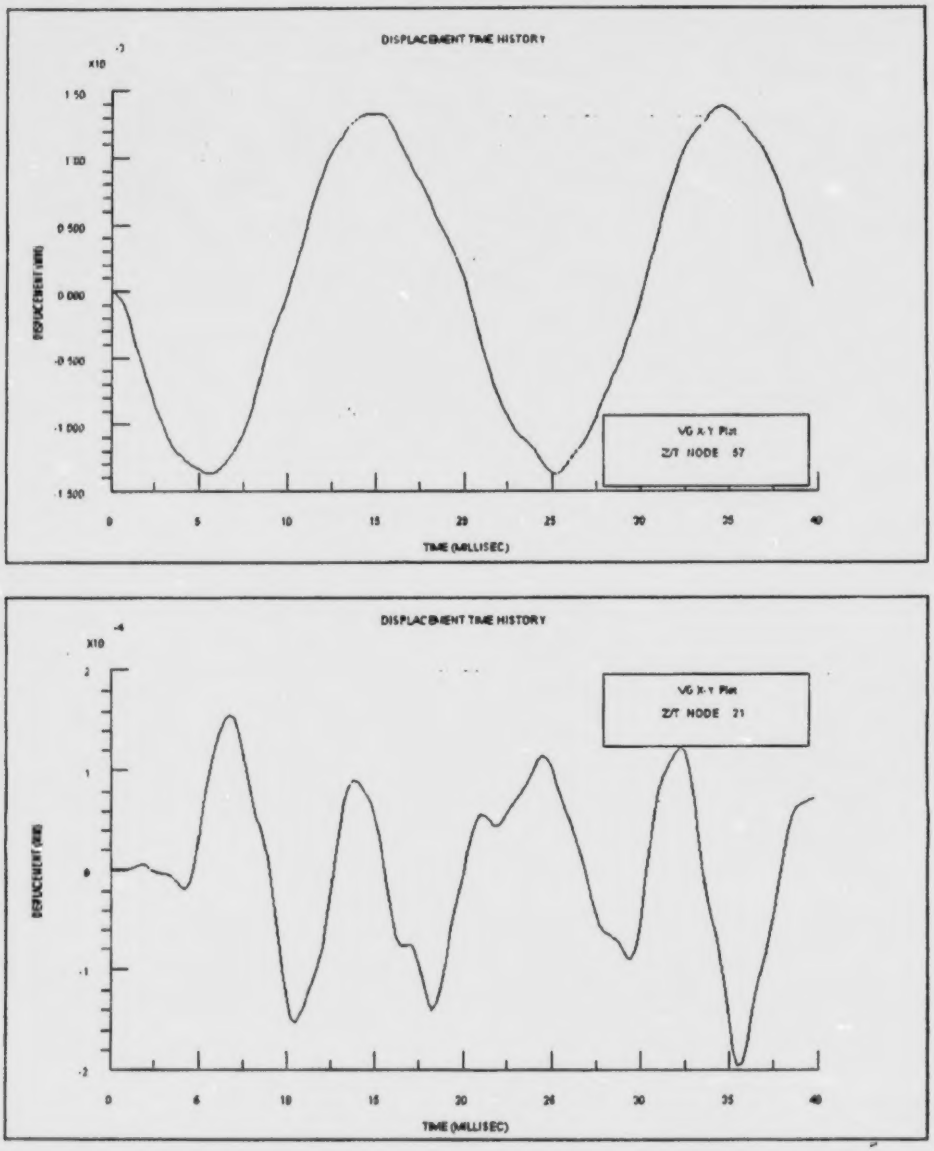

Figure 2.10: Time Histories of Vertical Displacement Predicted by the VAST Program for Linear Dynamic Analysis of the Engine Mount Under a Point Load.
(a) Center Node 57; (b) Corner Node 21.

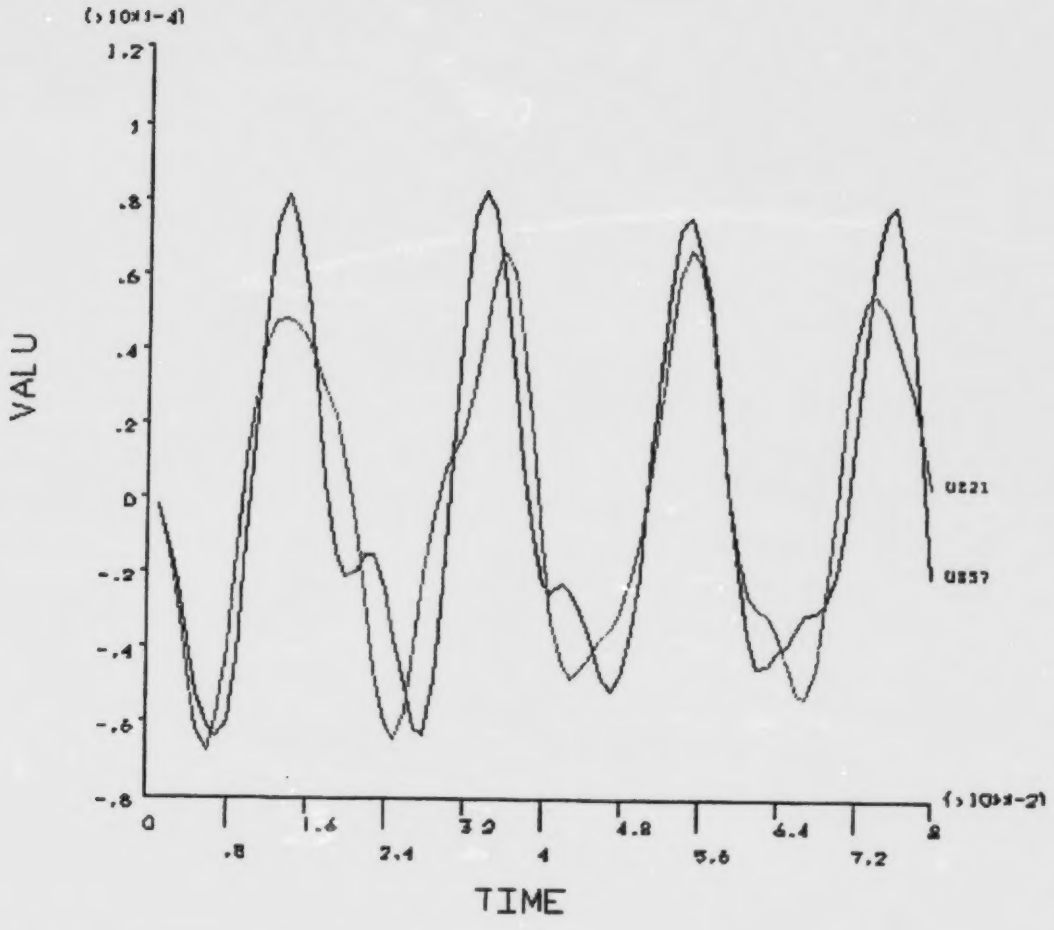

Figure 2.11: Time Histories of Vertical Displacements at Nodes 57 and 21 Predicted by the ANSYS Program for Linear Dynamic Analysis of the Engine Mount Under a Uniform Pressure.

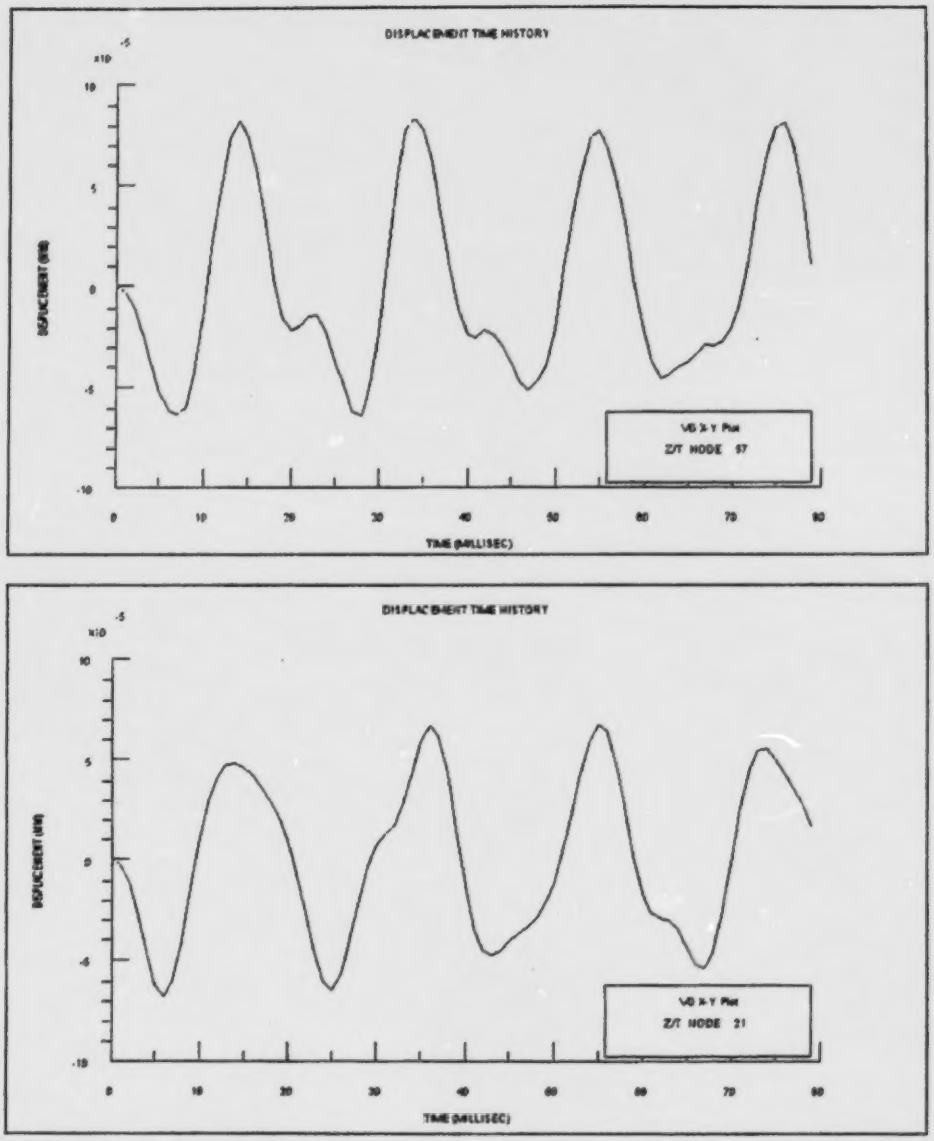

Figure 2.12: Time Histories of Vertical Displacement Predicted by the VAST Program for Linear Dynamic Analysis of the Engine Mount Under a Uniform Pressure. (a) Center Node 57; (b) Corner Node 21.

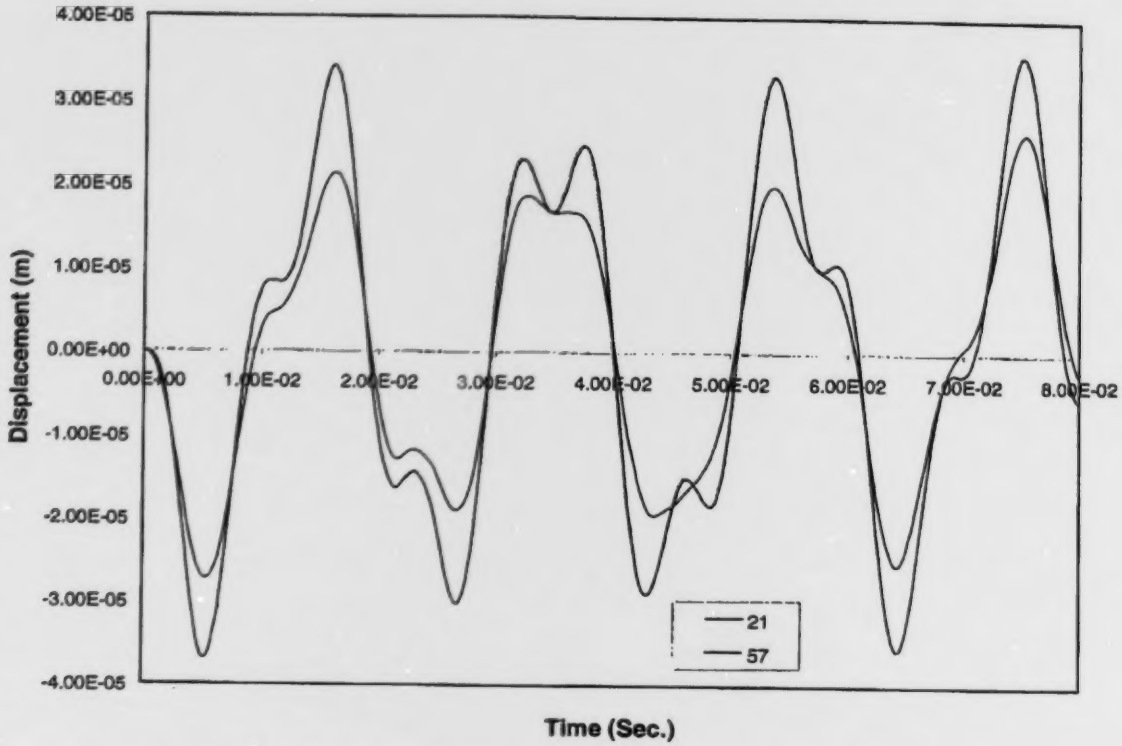

Figure 2.13: Nonlinear Dynamic Responses of the Engine Mount Without Initial Static Compression Predicted by ANSYS Using the Mooney-Rivlin Hyperelastic Model.

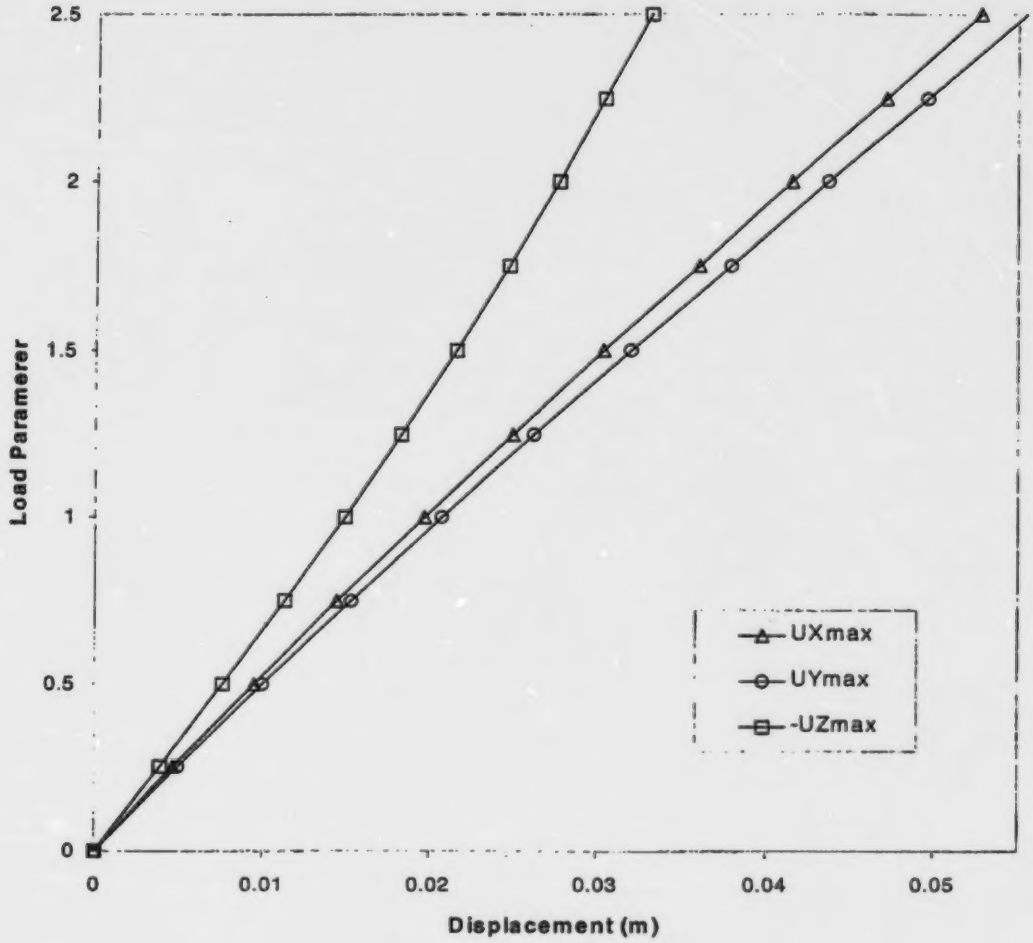

Figure 2.14 Load-Deflection Curves of the Engine Mount Under Static Compression Predicted by ANSYS Using the Mooney-Rivlin Hyperelastic Model.

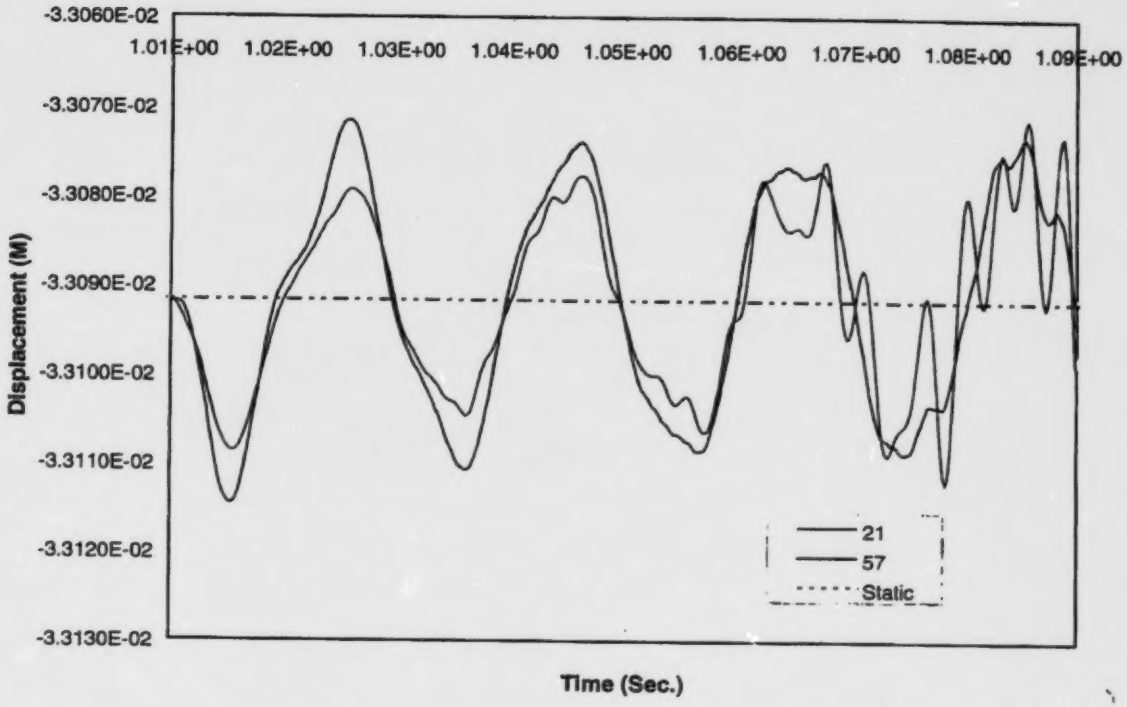

Figure 2.15: Nonlinear Dynamic Responses of the Engine Mount With Initial Static Compression Predicted by ANSYS Using the Mooney-Rivlin Hyperelastic Model.

3. DEVELOPMENT OF AN 8-NODED NONLINEAR SOLID ELEMENT FOR THE VAST PROGRAM

Extensive finite element analyses for studying the dynamic characteristics of a pre-strained engine mount model have been presented in the previous chapter. The results of these finite element analyses have clearly demonstrated the need of a nonlinear hyperelastic solid element for accurate solutions of rubber materials in the finite strain regime. Because the finite deformation of rubber materials often involved both geometrical and material nonlinearities, a solid element with general nonlinear capabilities must be implemented.

Through an extensive state-of-the-art literature survey on large strain finite element formulations, the co-rotational method recently proposed by Crisfield and co-workers [7-11] was found to be particularly attractive. This formulation was derived using the idea of element independent co-rotational algorithm initiated by Nour-Omid and Rankin [14]. Since the nonlinear formulation adopted in the VAST program was also based on the co-rotational algorithm described in [14], the nonlinear solid element developed by Crisfield [7-11] could easily fit into the overall code structure of VAST.

3.1 Theoretical Derivation of the Co-Rotation Formulation for 3-D Solid Element

In the co-rotational shell and beam elements previously implemented into the VAST program [15], the element local coordinate system was always calculated using the current nodal coordinates of the element. However, in the current nonlinear solid element, a slightly different approach for defining the local coordinate system was adopted following Crisfield and co-workers [8,11]. In the initial undeformed configuration, the element local co-ordinate system was assumed to coincide with the global system as:

$$\mathbf{E}^0 = \left[\mathbf{e}_1^0\ \mathbf{e}_2^0\ \mathbf{e}_3^0\right] = [\mathbf{i}\ \mathbf{j}\ \mathbf{k}] \tag{3.1}$$

where $\mathbf{E} = [\mathbf{e}_1\ \mathbf{e}_2\ \mathbf{e}_3]$ indicates the direction cosines of the element co-rotational coordinate system and the superscript "0" denotes the initial configuration at time "zero". In the deformed

configuration, the rigid body rotation matrix was computed through polar-decomposition of the deformation gradient matrix evaluated at the centroid of the element as:

$$\mathbf{F}_c = \mathbf{R}_c \mathbf{U}_c \tag{3.2}$$

and

$$\mathbf{E} = [\mathbf{e}_1\ \mathbf{e}_2\ \mathbf{e}_3] = \mathbf{R}_c \tag{3.3}$$

where **F**, **R** and **U** denote the deformation gradient matrix, the rotation matrix and the right stretch matrix, respectively. The subscript "C" indicates quantities evaluated at the centroid of the element. The method for calculating the rotation matrix from the deformation gradient matrix is not unique. In the present implementation, we first calculated the eigenvalues and eigenvectors of the deformation gradient matrix through a local eigenvalue analysis and then, formulated the inverse of the right stretch matrix as:

$$\mathbf{U}_c^{-1} = \sum_{i=1}^{3} \frac{1}{\lambda_i} \mathbf{N}_i \otimes \mathbf{N}_i \tag{3.4}$$

where λ_i and $\mathbf{N}_i$ (i=1,2,3) denote the eigenvalues and eigenvectors of **F**, respectively. Finally, the rotation matrix was evaluated as:

$$\mathbf{R}_c = \mathbf{F}_c\ \mathbf{U}_c^{-1} \tag{3.5}$$

Because this polar-decomposition was exact only if the deformation gradient matrix was constant over the entire solid element, this co-rotational formulation was obviously more suitable with lower-order solid elements.

One of the beauties of this co-rotational formulation was the equivalence between the co-rotational engineering strain and the Biot strain. After the removal of rigid body rotations from

the total deformation gradient matrix, the local co-rotational engineering strain could be evaluated at each numerical integration point as:

$$\boldsymbol{\varepsilon}_l = \frac{1}{2}\left(\mathbf{D}_l + \mathbf{D}_l^T\right) \tag{3.6}$$

where $\mathbf{D}_l$ is the local displacement derivative matrix defined as:

$$\mathbf{D}_l = \mathbf{U}_l - \mathbf{I} \tag{3.7}$$

Substituting Equation (3.7) into (3.6), the local engineering strain could be expressed as:

$$\boldsymbol{\varepsilon}_l = \frac{1}{2}\mathbf{U}_l + \frac{1}{2}\mathbf{U}_l^T - \mathbf{I} = \mathbf{U}_l - \mathbf{I} \tag{3.8}$$

This relation indicated that the local engineering strain, $\boldsymbol{\varepsilon}_l$, measured in the element co-rotational coordinate system could be considered as a Biot strain. It should be noticed that in the above derivation, the property of symmetry of the local right stretch matrix was utilized. As will be discussed in the next chapter, this equivalence between the co-rotational engineering strain and the Biot strain ensured convenient implementation of the large strain hyperelastic material model into this solid element.

Similar to the co-rotational formulations for structural elements implemented in VAST earlier [15], the strain-producing displacements measured in the local co-rotational coordinate system of each element were defined as the difference between the current and undeformed geometries as:

$$\mathbf{u}_l^i = \mathbf{x}_l^i - \mathbf{X}_l^i = \mathbf{E}^T\mathbf{x}_g^i - \mathbf{X}_l^i \tag{3.9}$$

where $\mathbf{x}_l$ and $\mathbf{X}_l$ denote local coordinates in current and original configurations, respectively. $\mathbf{x}_g^i$ is the current global coordinates, and the superscript "i" indicates the node number. The co-rotational engineering strain vector was then calculated using $\mathbf{u}_l$ as in regular finite element formulations.

In order to derive the transformation matrix, **T**, which connected the deformational and total displacement increments, we differentiated Equation (3.9) as:

$$\delta \mathbf{u}_l^i = \delta \mathbf{E}^T \mathbf{x}_g^i + \mathbf{E}^T \delta \mathbf{u}_g^i \tag{3.10}$$

The variation of the local co-rotational coordinate system could be expressed as:

$$\delta \mathbf{E} = \mathbf{S}(\delta\theta)\, \mathbf{E} \tag{3.11}$$

where $\delta\theta$ is the incremental rigid body rotations and **S**, a skew symmetric matrix. Substituting Equation (3.11) into (3.10) and making use of the properties of the skew symmetric matrix, **S**, we obtained:

$$\delta \mathbf{u}_l^i = \mathbf{E}^T \mathbf{S}\left(\mathbf{x}_g^i\right) \delta \grave{\mathbf{e}} + \mathbf{E}^T\, \delta \mathbf{u}_g^i \tag{3.12}$$

and for the entire element, we have:

$$\delta \mathbf{u}_l = \mathbf{z}\, \delta \grave{\mathbf{e}} + \left[\text{diag}\, \mathbf{E}^T\right] \delta \mathbf{u}_g \tag{3.13}$$

where [diag **E**] indicates a 24x24 block diagonal matrix and

$$\mathbf{z} = \left[\text{col}\, \mathbf{E}^T \mathbf{S}\left(\mathbf{x}_g^i\right)\right] \tag{3.14}$$

is a 24x3 block column matrix.

To find the relationship between the incremental rigid body rotation, $\delta\theta$, and the incremental global displacement vector, $\delta \mathbf{u}_g$, a spin vector evaluated at the centroid of the solid element was considered as:

$$\grave{\mathbf{U}}_l = \mathbf{A}_l^T\, \mathbf{u}_l \tag{3.15}$$

where $\mathbf{A}_l$ is a 24x3 matrix. Because $\mathbf{A}_l$ was evaluated using the original geometry measured in the element co-rotational frame, it remained constant throughout the entire nonlinear analysis. Due to the polar decomposition discussed before, the spin vector vanished at the element centre as:

$$\dot{\mathbf{U}}_l = \mathbf{0} \tag{3.16}$$

Differentiating Equation (3.16), we obtained:

$$\delta\dot{\mathbf{U}}_l = \mathbf{A}_l^T\ \delta\mathbf{u}_l = \mathbf{A}_l^T\ \lfloor diag\ \mathbf{E}^T \rfloor \delta\mathbf{u}_g + \mathbf{A}_l^T \mathbf{z}\delta\dot{\mathbf{e}} = \mathbf{0} \tag{3.17}$$

Rearranging terms in the above equation led to:

$$\delta\dot{\mathbf{e}} = -\left[\mathbf{A}_l^T\mathbf{z}\right]^{-1}\ \mathbf{A}_l^T\ \left[diag\ \mathbf{E}^T\right]\delta\mathbf{u}_g = \mathbf{v}^T\delta\mathbf{u}_g \tag{3.18}$$

Substituting Equation (3.18) into (3.13), the transformation matrix, **T**, was obtained as:

$$\delta\mathbf{u}_l = \left[\ \lfloor \text{diag}\ \mathbf{E}^T \rfloor + \mathbf{z}\mathbf{v}^T\ \right]\delta\mathbf{u}_g = \mathbf{T}\ \delta\mathbf{u}_g \tag{3.19}$$

Using the principle of virtual work, the transformation of the internal force vectors from the local to the global systems could be expressed as:

$$\mathbf{q}_g = \mathbf{T}^T\mathbf{q}_l \tag{3.20}$$

where the local internal force vector, $\mathbf{q}_l$, is evaluated using the linear strain-displacement matrices and co-rotational stresses computed at each numerical integration point. Derivation of the tangent stiffness matrix required differentiation of the global internal force vector as:

$$\delta\mathbf{q}_g = \mathbf{T}\delta\mathbf{q}_l + \delta\mathbf{T}^T\mathbf{q}_l = \left[\mathbf{T}^T\mathbf{K}_l\mathbf{T} + \mathbf{K}_G\right]\delta\mathbf{u}_g \tag{3.21}$$

where $\mathbf{K}_l$ indicates the local element stiffness matrix, which is the derivative of the local internal force vector, $\mathbf{q}_l$, with respect to the local deformational displacements $\mathbf{u}_l$. Now the second term in the right hand side of the above equation must be expressed as the product of the consistent geometric stiffness matrix, $\mathbf{K}_G$, and the global incremental displacement vector, $\delta\mathbf{u}_g$. To reach this goal, this term was first separated into three terms using the expression of the transformation matrix given in Equation (3.19) as:

$$\delta\mathbf{T}^T\mathbf{q}_l = \delta[\text{diag } \mathbf{E}]\mathbf{q}_l + \mathbf{v}\delta\mathbf{z}^T\mathbf{q}_l + \delta\mathbf{v}\mathbf{z}^T\mathbf{q}_l \tag{3.22}$$

After a quite lengthy mathematical manipulation detailed in references [8,11], the first two terms were simplified as:

$$\delta[\mathit{diag}\ \mathbf{E}]\mathbf{q}_l = -\left[\mathit{col}\ \mathbf{S}\left(\overline{\mathbf{q}}_l^j\right)\right]\mathbf{v}^T\ \delta\mathbf{u}_g \tag{3.23}$$

and

$$\mathbf{v}\delta\mathbf{z}^T\mathbf{q}_l = \left[\mathbf{v}\left[\text{row } \mathbf{S}\left(\overline{\mathbf{q}}_l^j\right)\right] + \mathbf{v}\sum_{j=1}^{n}\left[\mathbf{S}\left(\mathbf{x}_g^j\right)\mathbf{S}\left(\overline{\mathbf{q}}_l^j\right)\right]\mathbf{v}^T\right]\delta\mathbf{u}_g \tag{3.24}$$

where

$$\overline{\mathbf{q}}_l^j = \mathbf{E}\,\mathbf{q}_l^j \tag{3.25}$$

indicates the local internal force vector measured in the global coordinates system. n denotes the total number of nodes in the solid element. It should be noted that the second term in the right hand side of Equation (3.24) is unsymmetric. The derivation of the third term in Equation (3.22) was complicated by the differentiation of matrix, $\mathbf{v}$. However, Crisfield and co-workers [8,11] have demonstrated that the contribution of this term to the geometric stiffness matrix vanished at equilibrium, and neglecting this term and the unsymmetric part of (3.24) did not degrade the quadratic convergence rate of the Newton-Raphson iteration method. In the present work, we followed Crisfield's suggestion [8,11] and ignored these terms in our implementation. Combining

Equations (3.23) and (3.24), we came up with the final form of the consistent geometric stiffness matrix:

$$\mathbf{K}_G = -\left[\text{col } \mathbf{S}\left(\bar{\mathbf{q}}_i^j\right)\right]\mathbf{v}^T + \mathbf{v}\left[\text{row } \mathbf{S}\left(\bar{\mathbf{q}}_i^j\right)\right] + \mathbf{v}\,\text{sym}\sum_{j=1}^{n}\left[\mathbf{S}\left(\mathbf{x}_g^j\right)\mathbf{S}\left(\bar{\mathbf{q}}_i^j\right)\right]\mathbf{v}^T \qquad (3.26)$$

In order to improve the numerical performance of the lower-order solid element for bending dominant problems and incompressible or nearly incompressible materials, incompatible displacement modes, which are often referred as the "bubble modes", have been incorporated into the assumed displacement field in the element. The technique of using incompatible modes to enhance the accuracy of lower-order membrane and solid elements for bending dominant situations was first proposed by Taylor and co-workers [16] and later, refined by Wilson and Ibrahimbegovic [17]. Designed based on the consideration of passing the patch test, this technique has been proven highly efficient. The equivalence between this method and the enhanced strain formulation proposed by Simo and Armero [18] has been established. However, based on the numerical results obtained by Crisfield and co-workers [8,10,11] on various finite strain problems, the present 3-D solid co-rotational formulation with incompatible modes was numerically more stable than the enhanced strain method [18].

In the present implementation, the original standard displacement field of the solid element was modified by including contributions of "bubble" displacement modes as:

$$\mathbf{u} = \sum_{j=1}^{n} N_j(\xi,\eta,\zeta)\mathbf{u}_j + \sum_{k=1}^{3} N_k^*(\xi,\eta,\zeta)\mathbf{u}_k^* \qquad (3.27)$$

where the bubble functions are defined as:

$$\begin{aligned} N_1^* &= 1-\xi^2 \\ N_2^* &= 1-\eta^2 \\ N_3^* &= 1-\zeta^2 \end{aligned} \qquad (3.28)$$

and the coefficients corresponding to the bubble modes are internal variables and do not associate with the element nodes. It is obvious that the inclusion of the bubble modes would result in incompatible displacement distributions over the element boundaries. Using this modified displacement interpolation, the element local strain vector can be derived as:

$$\boldsymbol{\varepsilon}_l = \mathbf{B}_l\, \mathbf{u}_l + \mathbf{B}_l^* \mathbf{u}_l^* \tag{3.29}$$

where $\mathbf{B}_l$ and $\mathbf{B}_l^*$ are the regular and incompatible strain-displacement matrices, and $\mathbf{u}_l$ and $\mathbf{u}_l^*$ are nodal and internal degrees-of-freedom, respectively. It had been discovered [16, 17] that in order to pass the patch test, elements equipped with the incompatible displacement modes must be able to represent constant strain states in arbitrarily distorted element geometry. This required matrix $\mathbf{B}_l^*$ to satisfy the following equation:

$$\int_{V_l} \mathbf{B}_l^*\, dV = \mathbf{0} \tag{3.30}$$

This could be conveniently achieved by adding a constant term, $\mathbf{B}_c^*$, to $\mathbf{B}_l^*$ as [17]:

$$\tilde{\mathbf{B}}_l^* = \mathbf{B}_l^* + \mathbf{B}_c^* \tag{3.31}$$

where

$$\mathbf{B}_c^* = -\frac{1}{V_l}\int_{V_l} \mathbf{B}_l^*\, dV \tag{3.32}$$

and could be pre-calculated before the computation of element stiffness matrices and internal force vectors. With the incompatible displacement modes, the local incremental equilibrium equations can be discretized as:

$$\begin{bmatrix} \mathbf{K}_{l11} & \mathbf{K}_{l12} \\ \mathbf{K}_{l21} & \mathbf{K}_{l21} \end{bmatrix} \begin{Bmatrix} \delta\mathbf{u}_l \\ \delta\mathbf{u}_l^* \end{Bmatrix} + \begin{Bmatrix} \mathbf{q}_l \\ \mathbf{q}_l^* \end{Bmatrix} = \begin{Bmatrix} \mathbf{f} \\ \mathbf{0} \end{Bmatrix} \tag{3.33}$$

where the assumption that the internal degrees-of-freedom are not subjected to the external loads have been adopted. The stiffness sub-matrices were calculated as:

$$\begin{aligned} \mathbf{K}_{111} &= \int_{V_i} \mathbf{B}_i^T \, \mathbf{C}_i \mathbf{B}_i \, dV \\ \mathbf{K}_{112} &= \mathbf{K}_{121}^T = \int_{V_i} \mathbf{B}_i^T \, \mathbf{C}_i \tilde{\mathbf{B}}_i^* \, dV \\ \mathbf{K}_{122} &= \int_{V_i} \tilde{\mathbf{B}}_i^{*T} \, \mathbf{C}_i \tilde{\mathbf{B}}_i^* \, dV \end{aligned} \tag{3.34}$$

whereas the internal force vectors were defined as:

$$\begin{aligned} \mathbf{q}_i &= \int_{V_i} \mathbf{B}_i^T \, \acute{o}_i \, dV \\ \mathbf{q}_i^* &= \int_{V_i} \tilde{\mathbf{B}}_i^{*T} \, \acute{o}_i \, dV \end{aligned} \tag{3.35}$$

Using the second equation in (3.33), we have:

$$\delta \mathbf{u}_i^* = -\mathbf{K}_{122}^T \left(\mathbf{K}_{121} \, \delta \mathbf{u}_i + \mathbf{q}_i^* \right) \tag{3.36}$$

Substituting this relation back into the first equation in (3.33), the internal variables could be statically condensed out and the resulting element equilibrium equations became:

$$\overline{\mathbf{K}}_i \, \delta \mathbf{u}_i + \overline{\mathbf{q}}_i = \mathbf{f} \tag{3.37}$$

where the condensed element stiffness matrix and internal force vector were expressed as:

$$\begin{aligned} \overline{\mathbf{K}}_i &= \mathbf{K}_{111} - \mathbf{K}_{112} \, \mathbf{K}_{122}^{-1} \, \mathbf{K}_{121} \\ \overline{\mathbf{q}}_i &= \mathbf{q}_i - \mathbf{K}_{112} \, \mathbf{K}_{122}^{-1} \, \mathbf{q}_i^* \end{aligned} \tag{3.38}$$

During nonlinear analyses, the internal displacements are repeatedly updated at the end of each iteration as:

$$\mathbf{u}_I^* \leftarrow \mathbf{u}_I^* + \delta\mathbf{u}_I^* \tag{3.39}$$

and used in Equation (3.29) to calculate the current element strains.

3.2 Implementation of the Co-Rotational Formulation into the VAST Program

As mentioned earlier, because the co-rotational formulation incorporated into the 8-noded solid element in the present project was derived using the same concept as the element-independent co-rotational algorithm which had been previously implemented into various shell and beam elements in the VAST program, the present implementation did not require significant overall structural change of the program. However, considerable modifications were still needed at the element level, including the element subroutines for calculating element stiffness matrices and stresses. In the element stiffness routine, an algorithm was developed to perform the polar-decomposition at element center for computing rigid body rotations from the deformation gradient matrix. Capabilities for formulating internal force vectors and elastic-plastic tangent moduli were provided. Various coordinate transformations were implemented to transform element matrices and internal force vectors from the co-rotational frame to the global coordinate system. In addition to the original geometric stiffness matrix, the consistent stiffness matrix, given in Equation (3.26), had been incorporated. In the stress module, an algorithm was incorporated to separate the total displacement field into a rigid body motion part and a pure deformation part. Only the latter is related to the element strains. Both implicit and explicit numerical integration methods were implemented for integrating the rate-type elastic-plastic constitutive equations.

In order to enhance the performance of this lower-order solid element in bending dominant deformations and for incompressible materials, incompatible displacement modes were added to the displacement interpolation functions of the standard isoparametric solid element. Special treatment of the incompatible modes was utilized to ensure the accuracy of the element for arbitrarily distorted element geometry [16, 17]. The internal variables associated with these added bubble modes were eliminated at the element level through static condensation, which resulted in modifications of the element stiffness matrices and internal force vectors. As defined in equation (3.36), the computation of the incremental internal degrees-of-freedom at each

equilibrium iteration required the current local element stiffness matrix and internal force vector. However, in the VAST program, the .T43 file which contained these quantities along with the strain- or stress-displacement matrices was only updated at the beginning of a new solution step and remained unchanged during the equilibrium iterations. Because the internal force vector varied significantly during the Newton-Raphson iteration, its contribution to the internal variables was neglected and the local element stiffness alone was used to recover the internal degrees-of-freedom at the stage of strain calculation as:

$$\delta \mathbf{u}_I^* = -\mathbf{K}_{I22}^T \mathbf{K}_{I21} \ \delta \mathbf{u}_1 \tag{3.40}$$

It is obvious that these approximations would decrease the accuracy of element strains when the contributions of the incompatible bubble displacement modes were significant in the deformations. This problem must be addressed in further enhancement of the VAST program.

In the original implementation of the 8-noded solid element in VAST, element stresses were only computed at the element center and assumed constant over the entire element. Such a piece-wise constant stress distribution was insufficient for handling material nonlinearities and producing accurate internal force vectors required by nonlinear analyses. As a result, in the newly improved version of the 8-noded solid element, stresses at all numerical integration points were calculated in nonlinear analysis and stored on the .T53 file. For linear analysis, however, nodal stresses were computed and stored on the T53 file. An option for detailed stress output at integration points was also provided.

In order to increase the accuracy of the 8-noded solid element for nearly incompressible materials, a selective reduced integration technique has been implemented [5], in which the shear strain energy term was integrated accurately using a 2x2x2 Gauss rule, whereas the volumetric strain energy term was evaluated using a single point quadrature. This capability was preserved in the present improved solid element. For linear analysis, the selected reduced integration method will be automatically activated when the ratio of the Lamé parameter and shear modulus is greater than 2.

3.3 Numerical Verification of the 8-Noded Nonlinear Solid Element

In order to verify the performance of the improved 8-noded solid element in linear and nonlinear analyses, an extensive numerical study has been conducted. Some representative results are presented in this section.

3.3.1 Patch Test – In-plane Stretching and Bending of a Plate

In order to ensure that the improved 8-noded solid element with incompatible modes would pass the patch test, we first considered the in-plane stretching and bending problems suggested in References [16, 17]. This problem involved a rectangular plate subjected to uniform tension along the axial direction and uniform bending under in-plane end moment as shown in Figure 3.1. In the present study, we utilized the same regular and distorted finite element meshes as used in Reference [16]. The meshes used by VAST are displayed in Figures 3.2 and 3.3, respectively. The end displacements predicted by VAST for various meshes and load cases are compared with the exact solutions in Table 3.1. For both meshes, the 8-noded solid element passed the in-plane stretching patch test exactly. For the regular mesh, this element with incompatible modes passed the higher-order bending patch test, indicating that it behaved like a truly higher order (quadratic) element in bending dominant situations.

3.3.2 Bending of a Nearly Incompressible Cantilever Beam

In order to demonstrate the superior performance of the improved 8-noded element in modeling nearly incompressible materials, the bending problem of an incompressible cantilever beam considered previously in [5] was revisited in the present work. The problem geometry, external load and boundary conditions are shown in Figure 3.4, and the finite element mesh is given in Figure 3.5. In the previous analysis [5], the selective reduced numerical integration technique was utilized to handle the nearly incompressible material. In the present study, both reduced integration and incompatible displacement modes were used. The VAST results are presented in Table 3.2. These results indicate that both techniques are very effective in handling incompressible materials, and when Poisson's ratio becomes very close to 0.5, both techniques may be required at the same time to obtain satisfactory solutions. However, the use of selective

reduced integration caused extra complications in the treatment of material nonlinearities. As a result, in the current version of VAST, this option is turned off automatically in nonlinear analyses.

3.3.3 Linear Buckling Analysis of a Cantilever Beam Under Axial Compression

To verify the original and consistent geometric stiffness formulations of the 8-noded solid element, a buckling analysis of an axially compressed cantilever slender prismatic beam-column was considered. The geometric and material properties of the beam were assumed identical to those of the beam buckling problem considered in the previous chapter, namely length L=50.0 m, cross-section 1.0m x 1.0m, Young's modulus $E=2.0\times10^5$ MN/m^2 and Poisson's ratio $\nu=0.3$. The beam was fully constrained at one end and subjected to an axial compressive load at the other end. Twenty 8-noded solid elements were used to model the beam as shown in Figure 3.6. The first 16 buckling modes were obtained using both the original and consistent geometric stiffness matrices and the critical load values are compared with the analytical solutions [13] in Table 3.3. The finite element results obtained using different geometric stiffness formulations are in close agreement and agree with the analytical solutions. The buckling mode shapes predicted by both geometric stiffness matrices are also in close agreement and only those predicted by the consistent geometric stiffness matrix are displayed in Figure 3.7. Buckling loads were also obtained without the incompatible displacement modes and the results are included in Table 3.3 for comparison purposes. These results clearly indicated the crucial role of the incompatible modes in bending dominated problems.

3.3.4 Geometrically and Materially Nonlinear Analysis of a Simply-Supported Plate Under Uniform Pressure

This example involved nonlinear deformations of a simply-supported square plate subjected to a uniform pressure load. The problem geometry, material properties and boundary conditions are given in Figure 3.8. This problem has been solved previously by VAST using various shell and plate elements and the solutions were compared with the published results with excellent agreement [19]. In the present study, this problem was reconsidered using the 8-noded

solid element. Due to symmetry in this problem, a quarter of the plate was modeled using four different meshes as shown in Figure 3.9. Nonlinear solutions were obtained for the geometrically nonlinear and nonlinear-material-only situations by using various solid element meshes and the resulting load-center deflection curves are presented in Figure 3.10(a, b). The nonlinear solutions obtained using a 4x4 mesh of the 4-noded quadrilateral shell element are also included for comparison purposes. These results indicated that the coarse mesh (mesh 1) of the 8-noded solid element mesh was inadequate for this problem. However, solutions produced by the 4x4x2 mesh (mesh 2) of the solid element were already in good agreement with the shell element results. The solutions of meshes 3 and 4 were not only in excellent agreement with the shell solutions, but also very close to each other, indicating the convergence of the VAST nonlinear analyses.

In order to demonstrate the effect of the incompatible displacement modes, geometrically and materially nonlinear responses of the plate were also computed without the bubble modes using mesh 2. The results obtained with and without the incompatible modes are compared in Figure 3.11. The superior numerical performance of the incompatible modes in nonlinear analyses is clearly demonstrated.

3.3.5 Large Displacement Analysis of a 45° Bend Subjected to an Out-of-Plane Force

In this example, we considered nonlinear response of a 45° bend as shown in Figure 3.12. This bend, which was clamped at one end and loaded by an out-of-plane point force at the other end, experienced extremely large displacements and rotations. This is a very difficult test problem and has been used by a number of researchers to verify their nonlinear finite element formulations [8,11,15]. In the present work, two meshes were utilized as shown in Figure 3.13, which contained 10 2-noded general beam elements and 16 8-noded solid elements, respectively. Again, due to the superior bending behavior of the solid element with incompatible modes, only one row of elements were employed in the solid element mesh. The non-dimensionalized load-tip deflection curves obtained by using the beam and solid elements are compared in Figure 3.14. Very close agreement between these two solutions is observed. Both the original and the newly implemented geometric stiffness matrices of the solid element were utilized in the present analysis. It was very interesting to find out that the convergence rate with the original geometric stiffness

matrix was considerably faster than the consistent one presented in Section 3.1 of the current report.

3.3.6 Post-Buckling Analysis of a Hinged Spherical Shell

This problem was used to test the ability of the 8-noded solid element to handle snap-through-type geometrically nonlinear behavior. The problem geometry and external load conditions are given in Figure 3.15. All four edges of the spherical shell were hinged and immovable in all three directions. Similar to the last numerical example, this problem is also a standard benchmark problem and has been solved by a number of researchers. In a previous report [15], the VAST solution to this problem using 4-noded quadrilateral shell elements was compared with published numerical results with excellent agreement. As a result, in the present work, we compared the solid element solution against the result from the quadrilateral shell element. Due to symmetry in this problem, one-quarter of the spherical shell was modeled by a 3x3 mesh of the shell element and a 3x3x2 mesh of the solid element, as shown in Figure 3.16. The load-center deflection curves predicted by these two elements are compared in Figure 3.17. Good agreement is observed in both pre- and post-buckling solutions. The displacement control solution strategy has been used in this problem to obtain the complete nonlinear solution.

3.3.7 Snap-Through and Snap-Back Analysis of a Shallow Cylindrical Shell

This problem involved highly nonlinear responses of a shallow cylindrical shell subjected a vertical point load at the center as shown in Figure 3.18. The straight edges of the shell were hinged and the curved edges were free. Two shell thicknesses were considered and the snap-back behavior appeared in the thinner shell situation. Because the accuracy of the 4-noded quadrilateral shell element was previously verified for this problem [15], a solution obtained using a 4x4 mesh of quadrilateral shell element was employed as the reference solution in the present study. Due to symmetry in this problem, only one quarter of the shell was modeled. The solid element meshes for different shell thicknesses are given in Figure 3.19. The load-deflection curves at the center node (C) and edge node (E) obtained by using the shell and solid elements are compared in Figures 3.20 and 3.21 for the thicker and thinner cylindrical shells, respectively. The shell and solid

element solutions are in close agreement for both shell thicknesses. The orthogonal trajectory solution strategy with automatic solution step adjustment algorithm was used in these analyses to successfully trace the entire load-deflection curves.

3.3.8 Geometrically and Materially Nonlinear Analyses of a Clamped-Clamped Shallow Cylindrical Arch

This problem involved combined geometrically and materially nonlinear response of a shallow cylindrical arch. This arch was clamped at both ends and loaded by a concentrated vertical force at the mid-span as shown in Figure 3.22. Due to symmetry in this problem, half of the arch was discretized into two meshes containing 16 4-noded quadrilateral shell and 8-noded solid elements, respectively (see Figure 3.23). The load-center deflection curves obtained by both elements for geometrically and combined nonlinear analyses are compared in Figure 3.24. In both nonlinear situations, the predictions of the shell and solid elements are in very good agreement. Considering the coarseness of the solid element mesh utilized in the present analysis, the performance of the element in bending dominant problems is indeed impressive.

3.3.9 Geometrically and Materially Nonlinear Analyses of a Shallow Spherical Cap

In this final example, we considered combined geometrically and materially nonlinear behavior of a shallow spherical shell subjected to a center point load as shown in Figure 3.25. Two kinds of boundary conditions were considered. In the first boundary condition, the outer edge of the spherical shell was clamped, whereas in the second boundary condition, the spherical shell was hinged along the edge. The 4-noded shell and 8-noded solid element meshes for this problem are given in Figure 3.26, which contained one-quarter of the entire structure. Using the orthogonal trajectory solution strategy with automatic solution step adjustment, geometrically and combined nonlinear solutions of the spherical shell with different boundary conditions were obtained using both shell and solid elements. The load-center deflection curves predicted by both elements are compared in Figures 3.27 and 3.28, for clamped and hinged boundary conditions, respectively. Very close agreement between the shell and solid solutions is again observed.

Table 3.1: Patch Test Results of the Present 8-Noded Solid Element and the Exact Solutions.

Mesh	Incompatible Modes	End Displacement	
		Stretching	Bending
Regular	No	6.0	-17.76
Regular	Yes	6.0	-18.0
Distorted	No	6.0	-16.94
Distorted	Yes	6.0	-17.58
Exact	-	6.0	-18.0

Table 3.2: End Deflections of the Nearly Incompressible Beam Obtained by the 8-Noded Solid Element With Reduced Integration and Incompatible Modes.

Reduced Integration	Incompatible Modes	End Deflection		
		PR=0.49	PR=0.4999	PR=0.4999999
No	No	-0.5896	-0.1074	-0.0469
Yes	No	-0.9069	-0.9034	-0.9033
No	Yes	-0.9406	-0.8118	-0.7188
Yes	Yes	-0.9971	-0.9940	-0.9940

Table 3.3: Buckling Loads of an Axially Loaded Slender Cantilever Beam Predicted by the 8-Noded Solid Element with the Original and Consistent Geometric Stiffness Matrices.

Buckling Mode	Exact Solution [13]*	8-Noded Solid Element			
		With Bubble Mode		Without Bubble Mode	
		Original K_G	Consistent K_G	Original K_G	Consistent K_G
1	16.449	16.520	16.522	58.625	58.631
2	16.449	16.520	16.522	58.626	58.631
3	148.04	149.67	149.79	528.59	529.02
4	148.04	149.67	149.79	528.59	529.02
5	411.23	421.26	422.21	1473.5	1476.9
6	411.23	421.26	422.23	1473.5	1477.0
7	806.02	842.32	846.10	2903.4	2916.9
8	806.02	842.36	846.22	2903.7	2917.1
9	1332.4	1430.2	1441.1	4831.7	4870.4
10	1332.4	1430.4	1441.3	4833.0	4871.2
11	1990.4	2210.2	2235.8	7276.8	7368.2
12	1990.4	2210.5	2236.4	7279.5	7371.3
13	2779.9	3216.1	3271.2	10257.	10447.
14	2779.9	3217.1	3271.7	10261.	10451.
15	3701.1	4494.1	4601.0	13791.	14148.
16	4927.5	6103.4	6299.1	17894.	18531.

*Note: Unit of buckling load is MN.

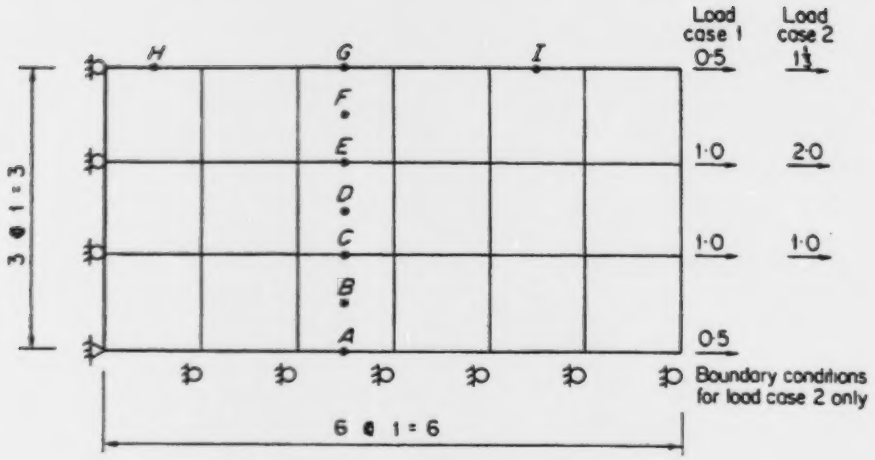

Figure 2(a). Mesh configuration for patch test

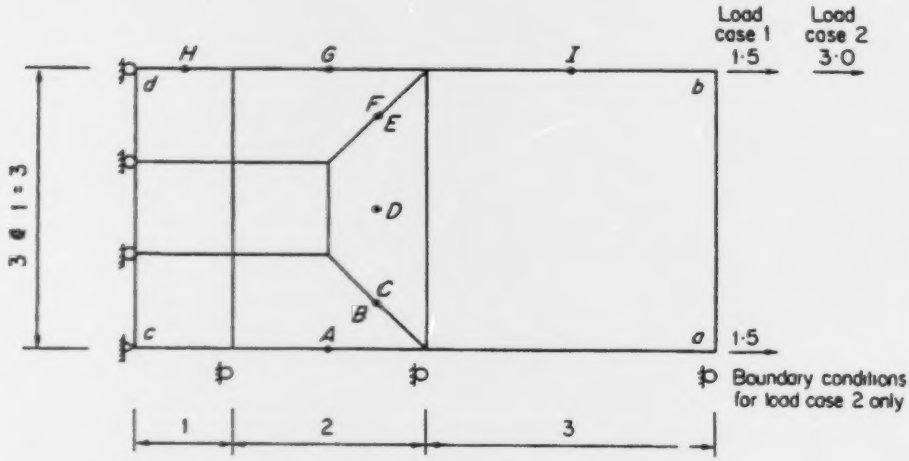

Figure 3.1: Problem Geometry, Mesh Layouts, Load Conditions and Boundary Constrains for Patch Test Employed in Reference [16].

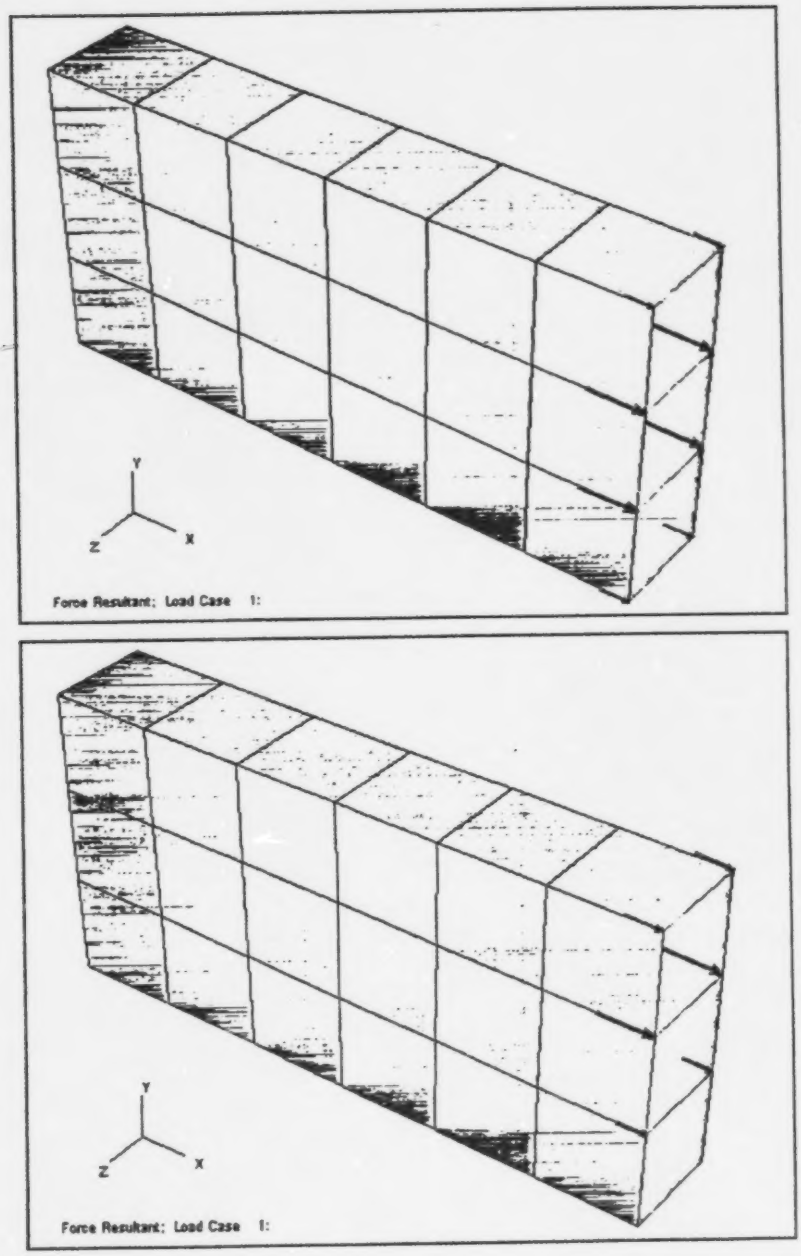

Figure 3.2: Regular Mesh Utilized for Patch Test for the 8-Noded Solid Element in VAST.
(a) Uniform Axial Tension, (b) Uniform Bending Moment.

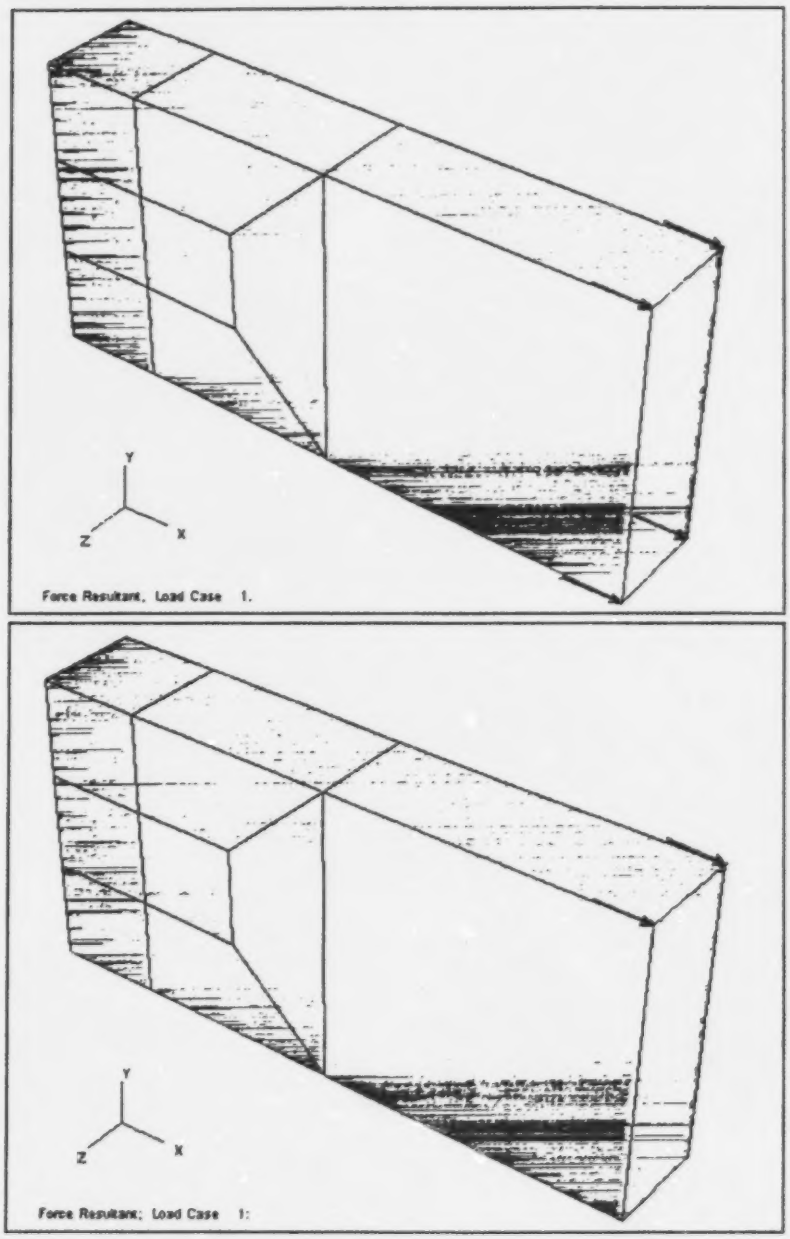

Figure 3.3: Distorted Mesh Utilized for Patch Test for the 8-Noded Solid Element in VAST.
(a) Uniform Axial Tension, (b) Uniform Bending Moment.

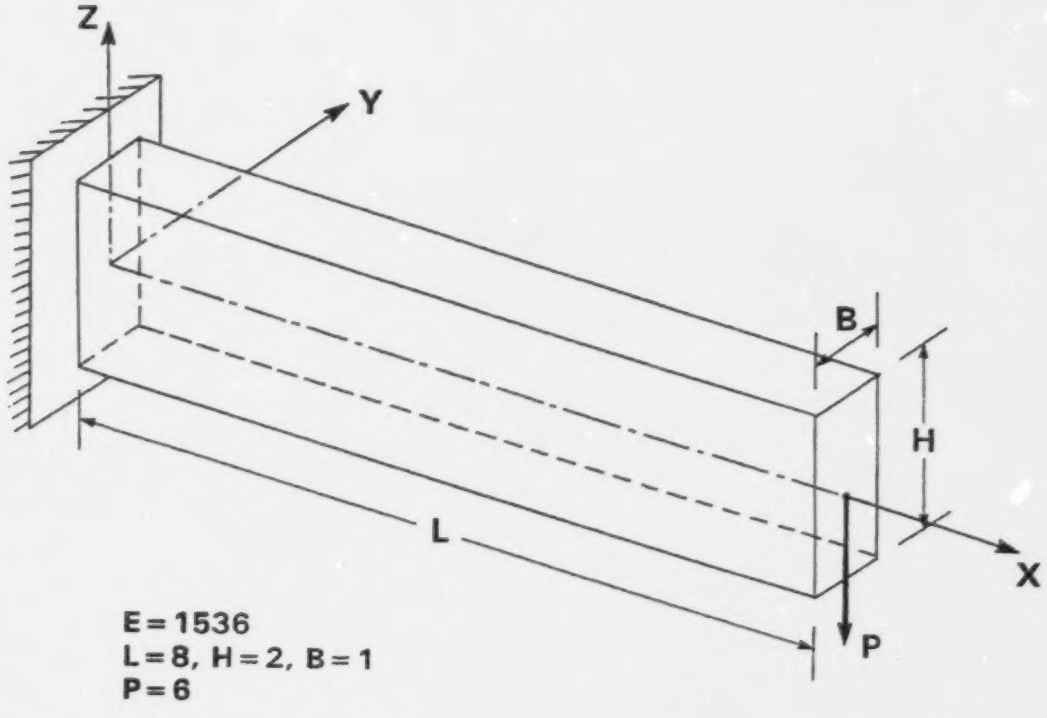

Figure 3.4: Problem Geometry, Load Conditions and Boundary Constrains for Bending Analysis of a Nearly Incompressible Cantilever Beam.

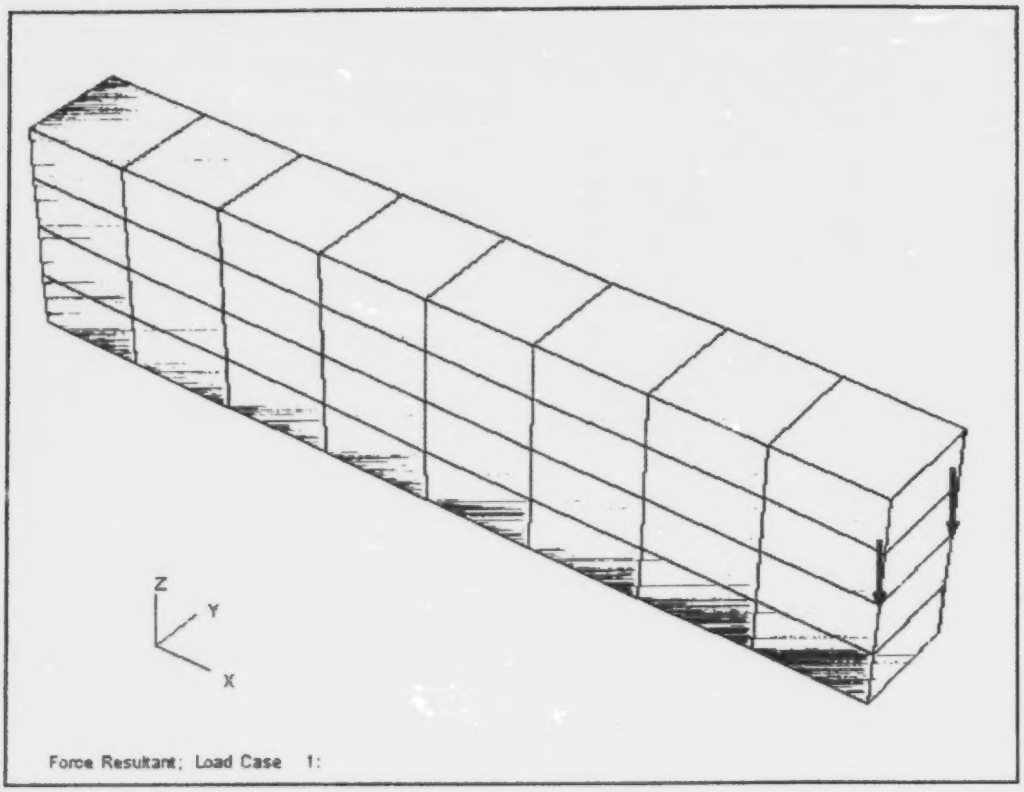

Figure 3.5: 8-Noded Solid Element Mesh for Bending Analysis of the Nearly Incompressible Cantilever Beam.

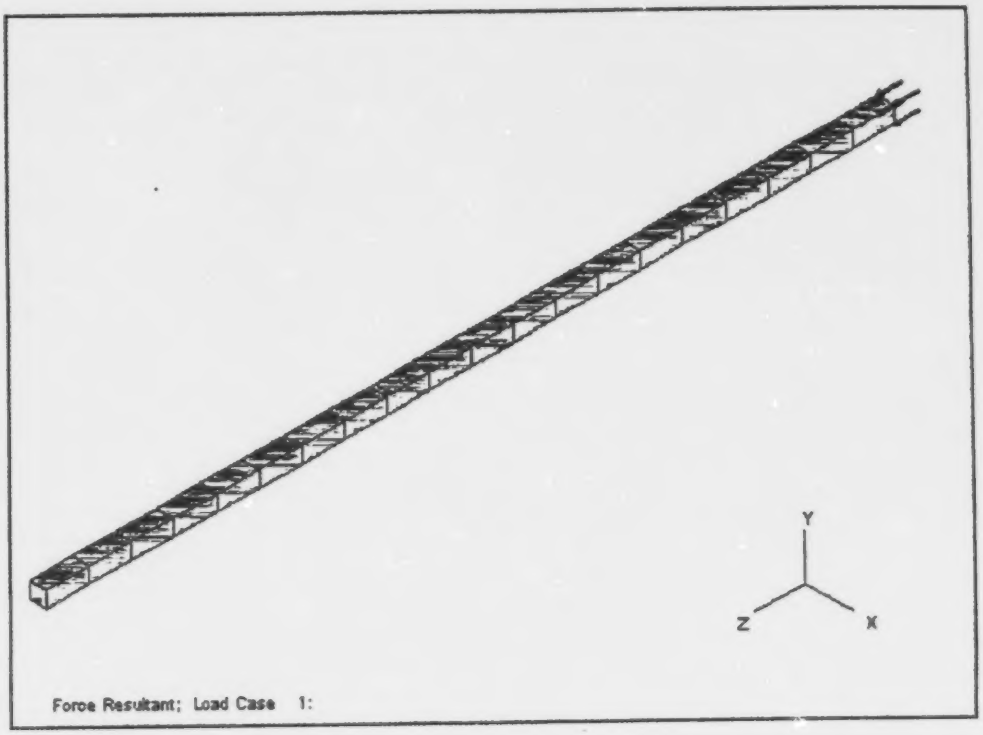

Figure 3.6: 8-Noded Solid Element Mesh for Linear Buckling Analysis of a Cantilever Beam Under Axial Compression.

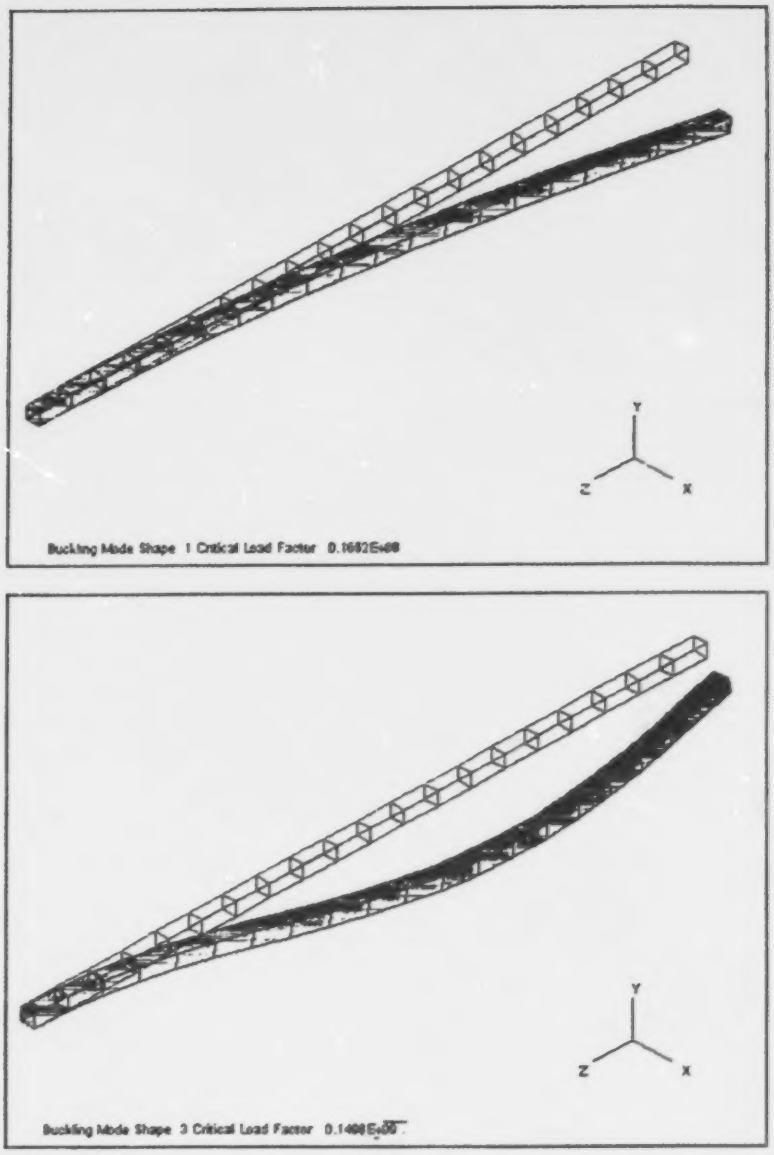

Figure 3.7: Buckling Mode Shapes of the Axial Loaded Cantilever Beam Predicted by the 8-Noded Solid Element in VAST. (a) Mode One. (b) Mode Two.

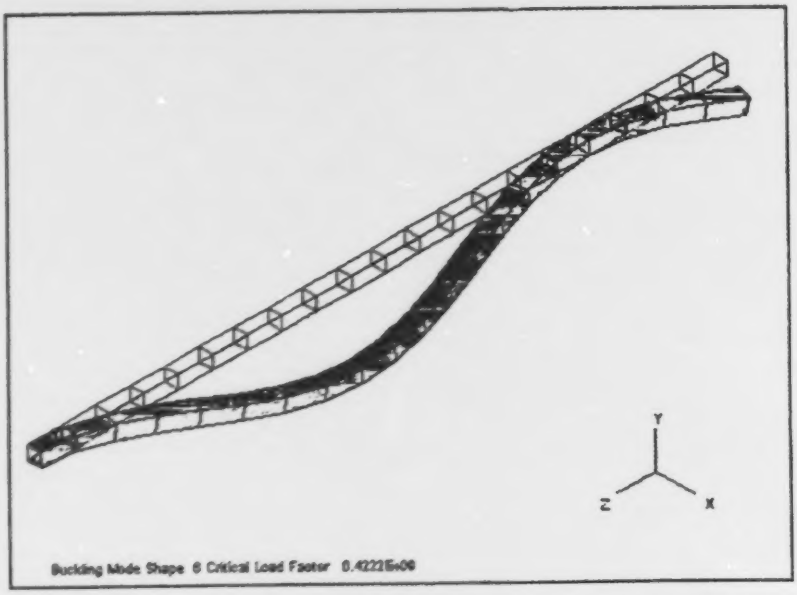

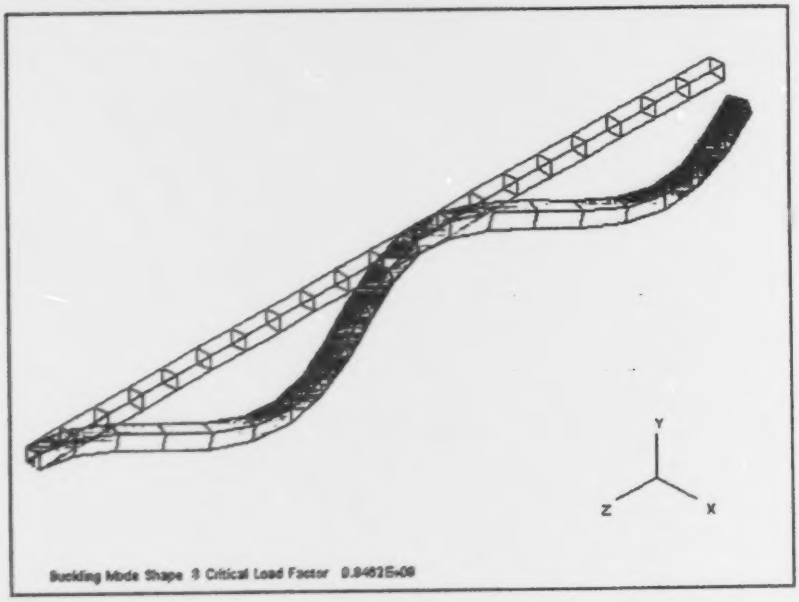

Figure 3.7 (continued): Buckling Mode Shapes of the Axial Loaded Cantilever Beam Predicted by the 8-Noded Solid Element in VAST. (c) Mode Three. (d) Mode Four.

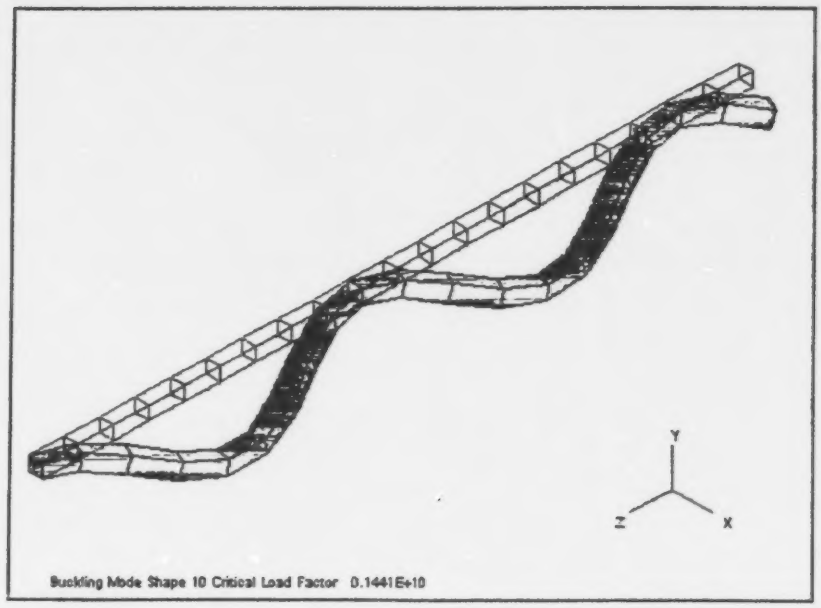

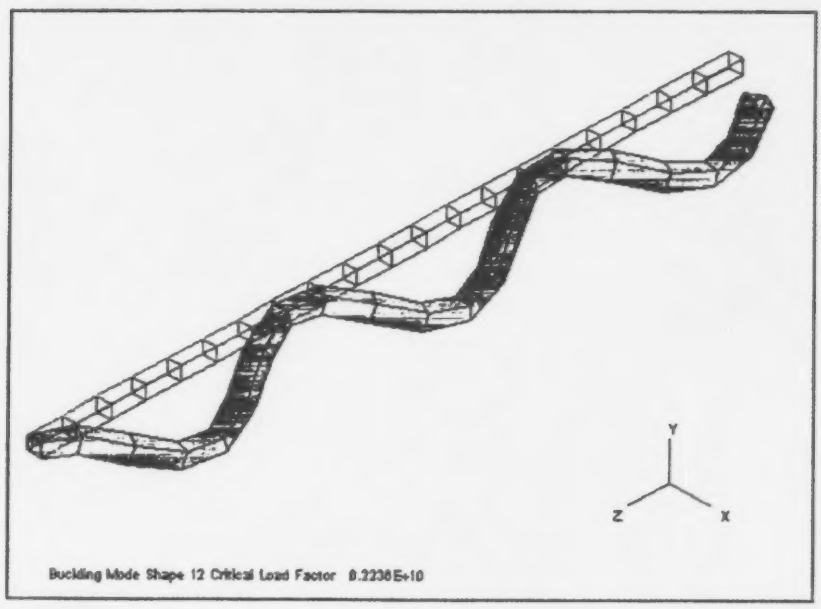

Figure 3.7 (continued): Buckling Mode Shapes of the Axial Loaded Cantilever Beam Predicted by the 8-Noded Solid Element in VAST. (e) Mode Five. (f) Mode Six.

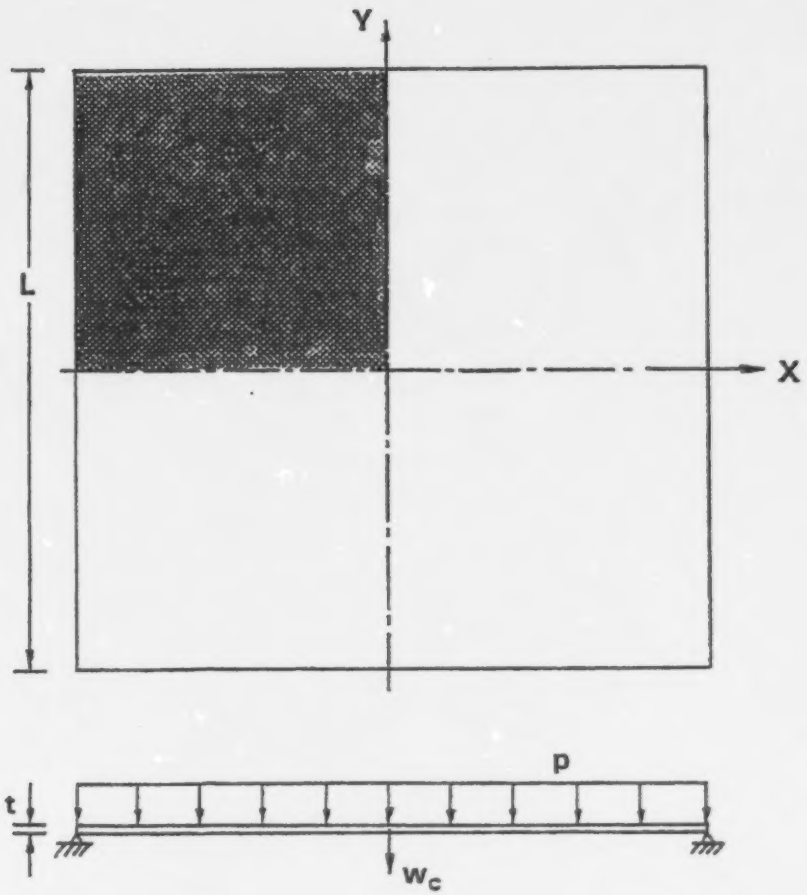

$E = 2.0 \times 10^{11}$ N/m², $\nu = 0.3$
$\sigma_Y = 3.0 \times 10^{8}$ N/m², $E_T = 0.0$ N/m²
L = 8.0 m, t = 0.2 m
$p = \lambda \times 1.125 \times 10^{6}$ N/m²

Figure 3.8: Problem Geometry, Load Conditions and Boundary Constrains for Nonlinear Analysis of a Simply-Supported Square Plate Under Uniform Pressure.

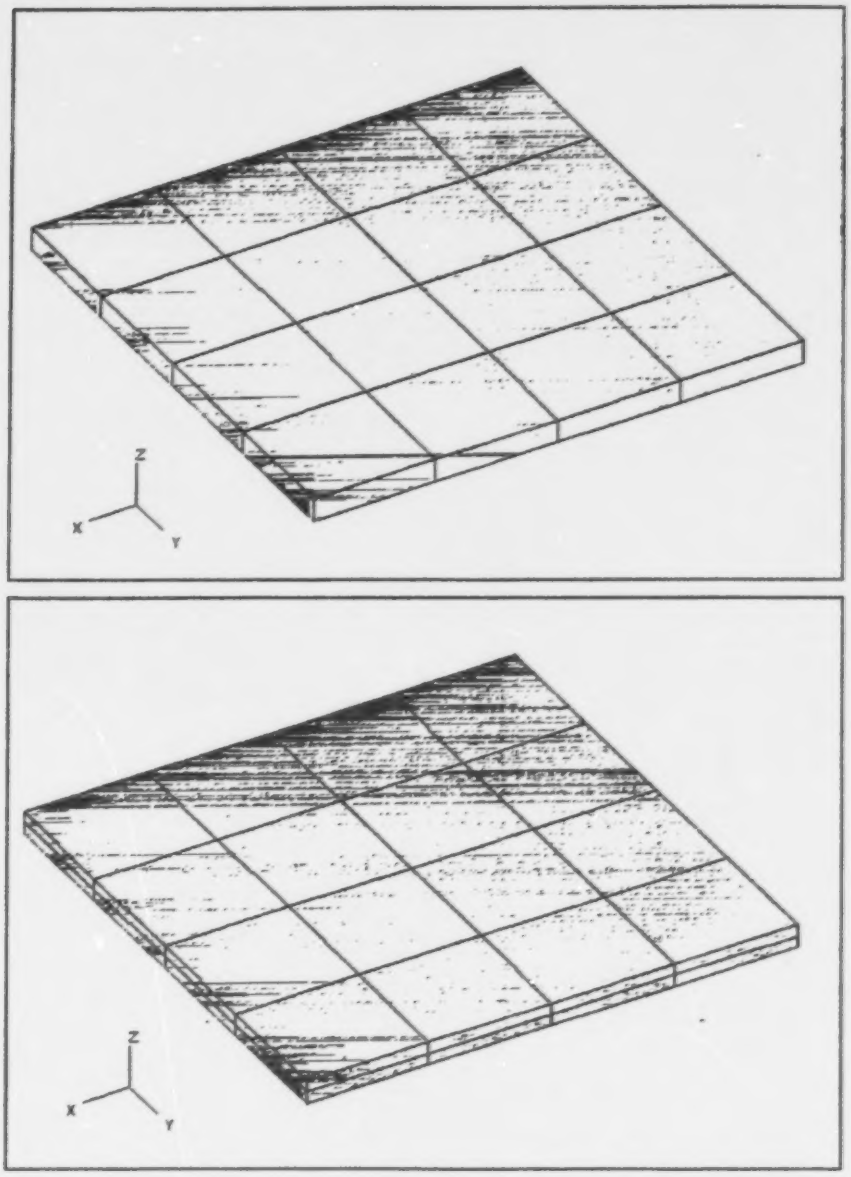

Figure 3.9: Solid Element Meshes for Nonlinear Analyses of the Simply-Supported Square Plate Under Uniform Pressure. (a) 4x4x1 Mesh, (b) 4x4x2 Mesh.

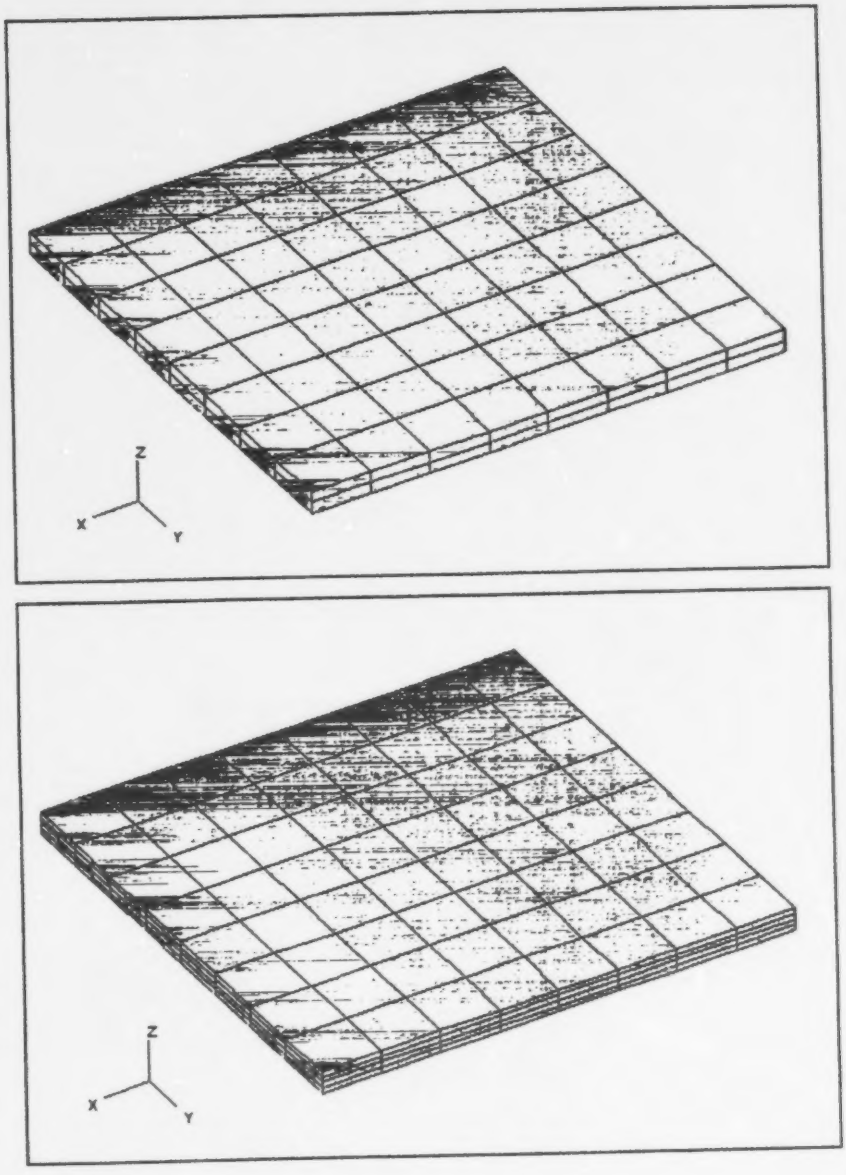

Figure 3.9 (continued): Solid Element Meshes for Nonlinear Analyses of the Simply-Supported Square Plate Under Uniform Pressure. (c) 8x8x2 Mesh, (d) 8x8x4 Mesh.

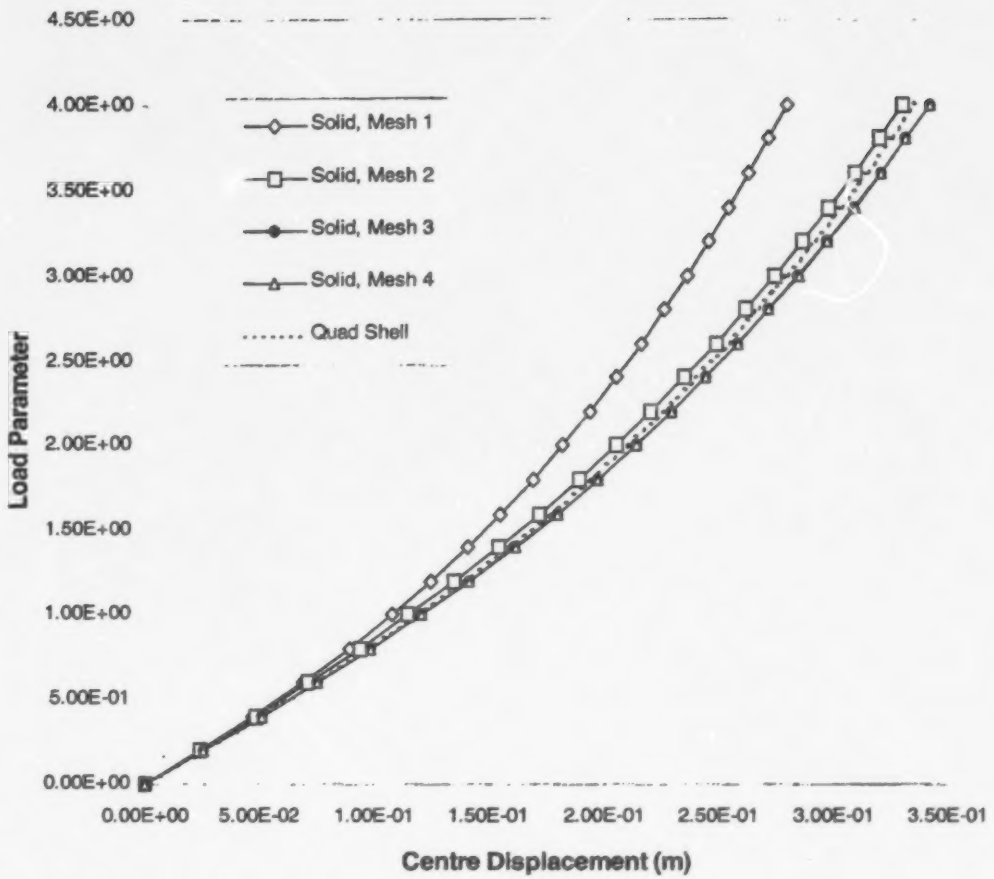

Figure 3.10: Comparison of Load-Center Deflection Curves of the Square Plate Obtained by the 8-Noded Solid and 4-Noded Quad Shell Elements.
(a) Geometrically Nonlinear Analyses.

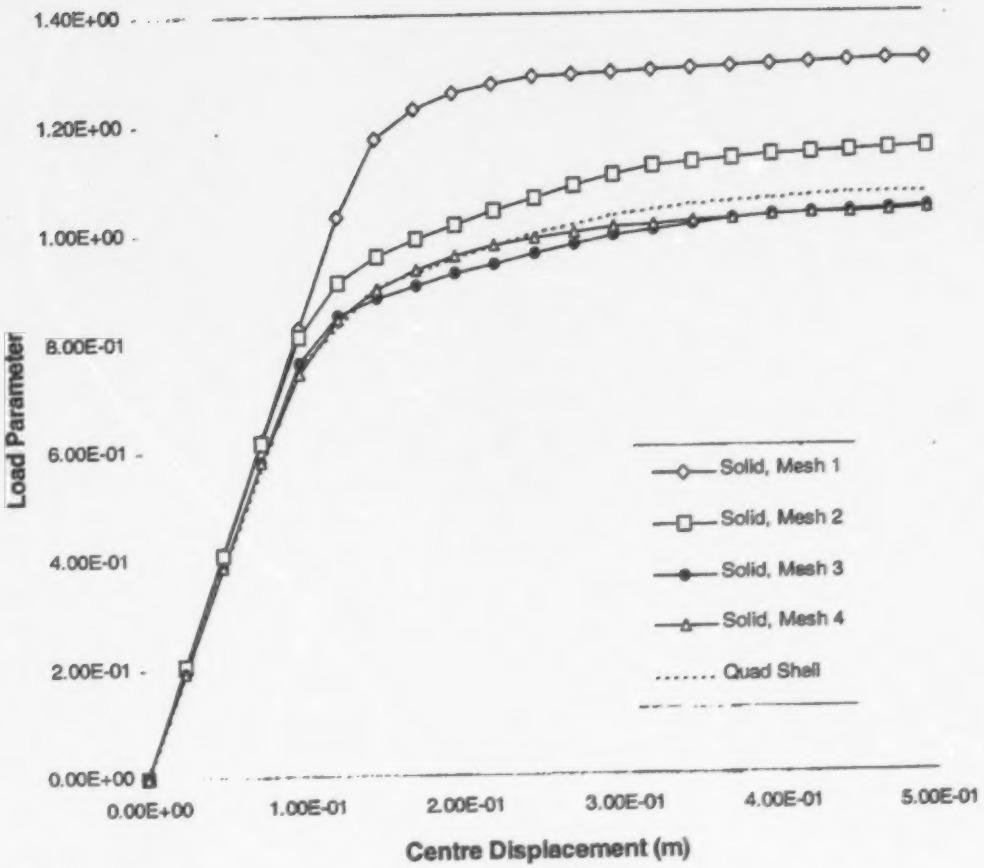

Figure 3.10 (continued): Comparison of Load-Center Deflection Curves of the Square Plate Obtained by the 8-Noded Solid and 4-Noded Quad Shell Elements.
(b) Nonlinear-Material-Only Analyses.

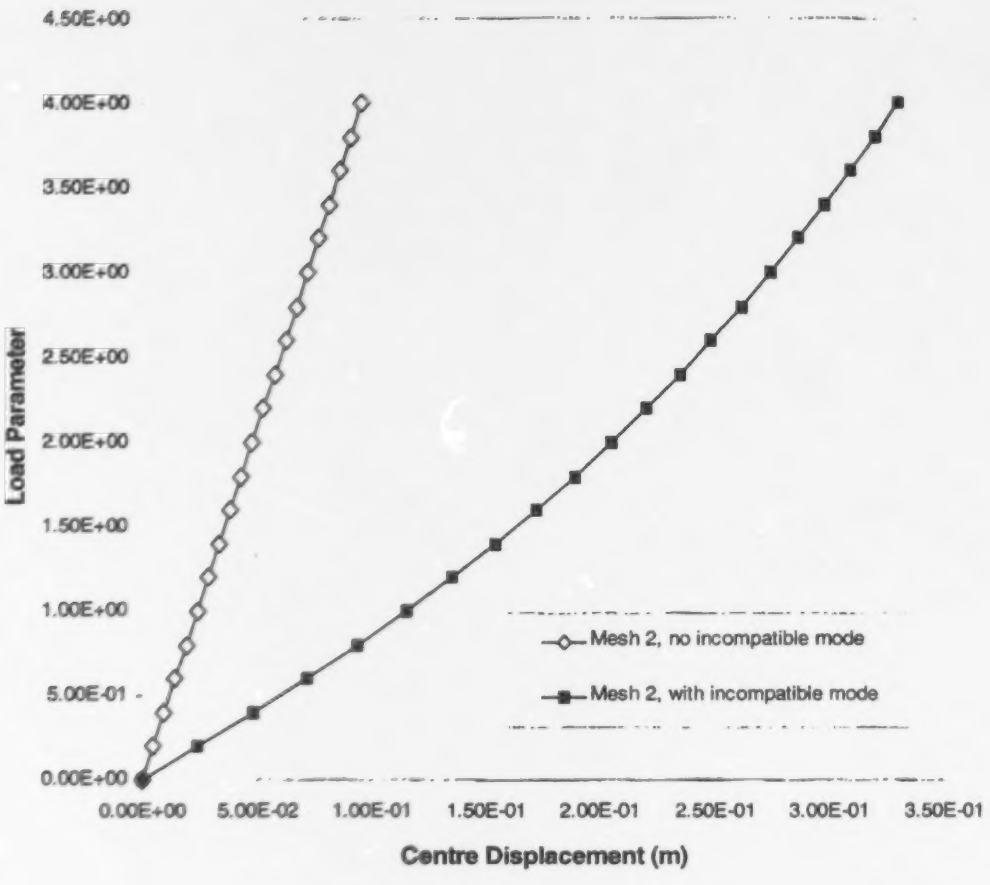

Figure 3.11: Comparison of Load-Center Deflection Curves of the Square Plate Obtained by the 8-Noded Solid Element With and Without the Incompatible Modes.
(a) Geometrically Nonlinear Analyses.

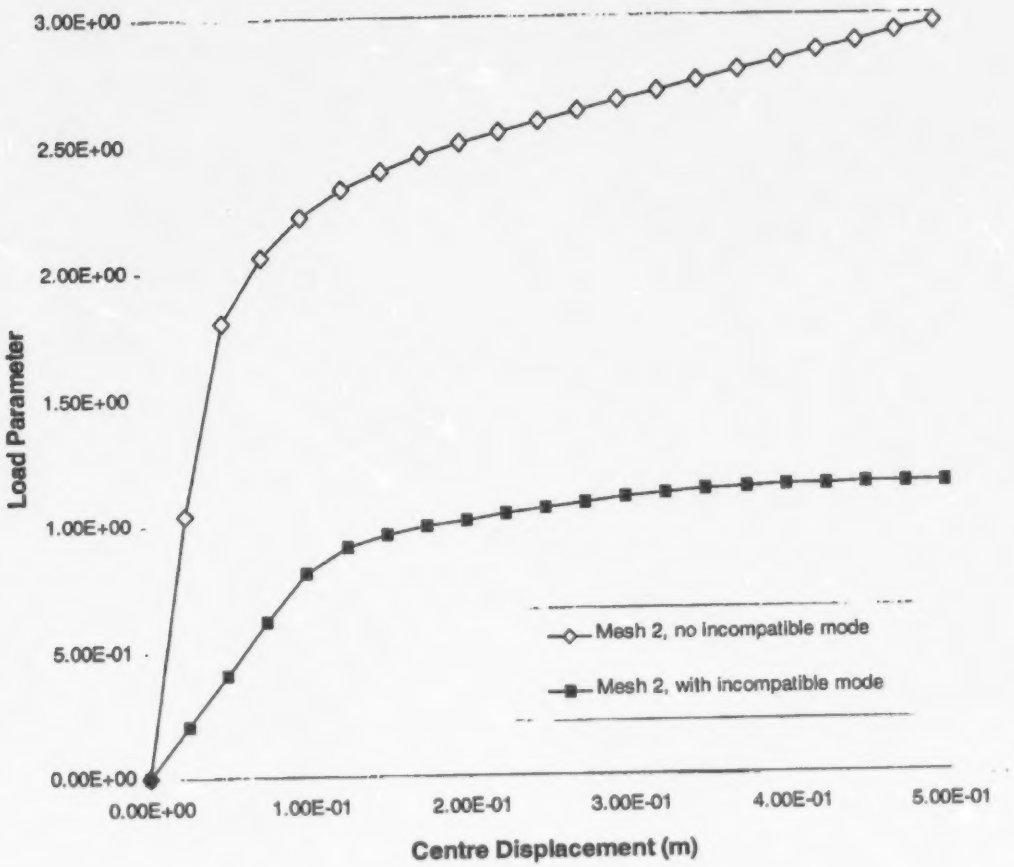

FIGURE 3.11 (continued): Comparison of Load-Center Deflection Curves of the Square Plate Obtained by the 8-Noded Solid Element With and Without the Incompatible Modes. (b) Nonlinear-Material-Only Analyses.

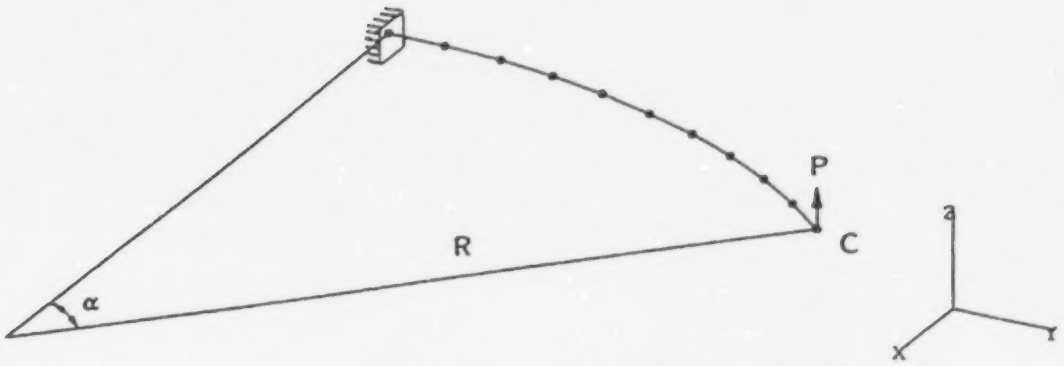

E = Young's Modulus = 1.0×10^7
ν = Poisson's Ratio = 0.0
b = Width = 1.0
h = Thickness = 1.0
R = Radius = 100.0
α = Subtending Angle = 45.0°

Figure 3.12: Problem Geometry, External Load and Boundary Conditions for Large Displacement Analysis of a 45° Bend Under an Out-of-Plane Force.

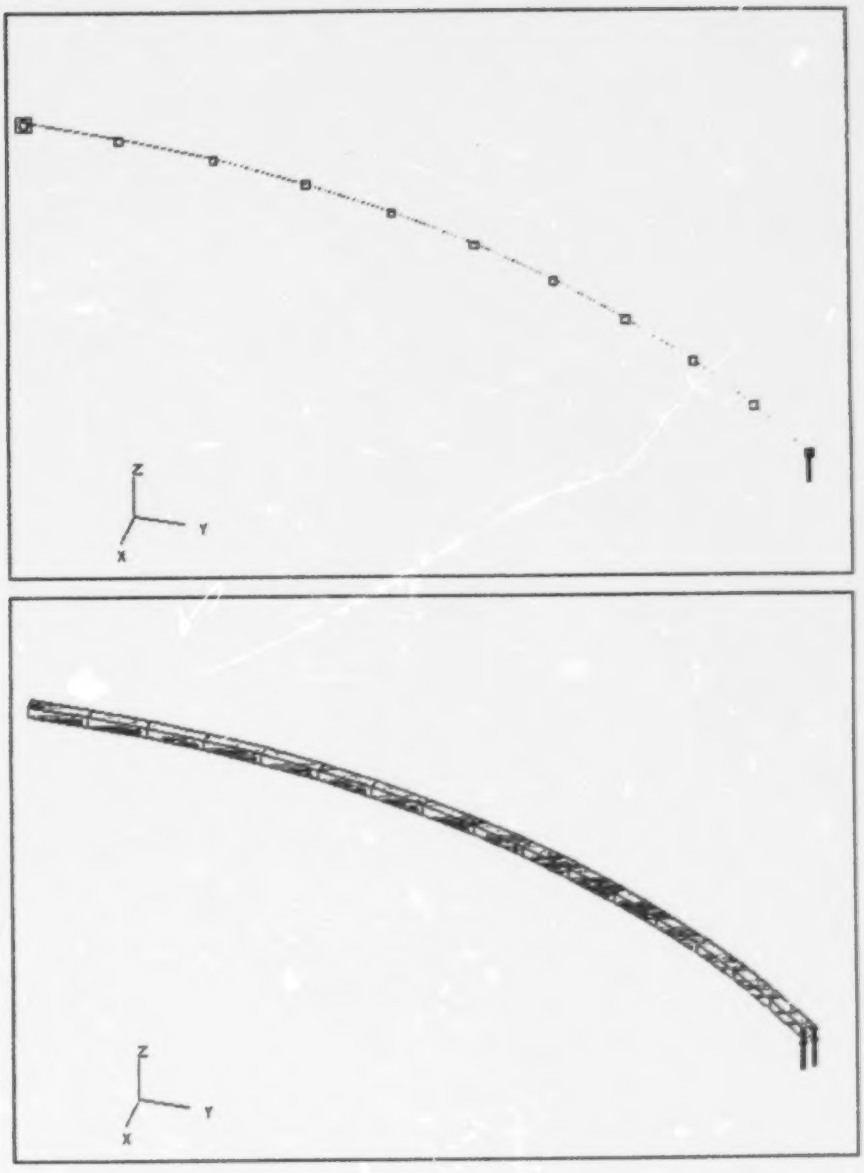

Figure 3.13: Finite Element Meshes for Large Displacement Analysis of the 45° Bend.
(a) 2-Noded General Beam Element, (b) 8-Noded Solid Element.

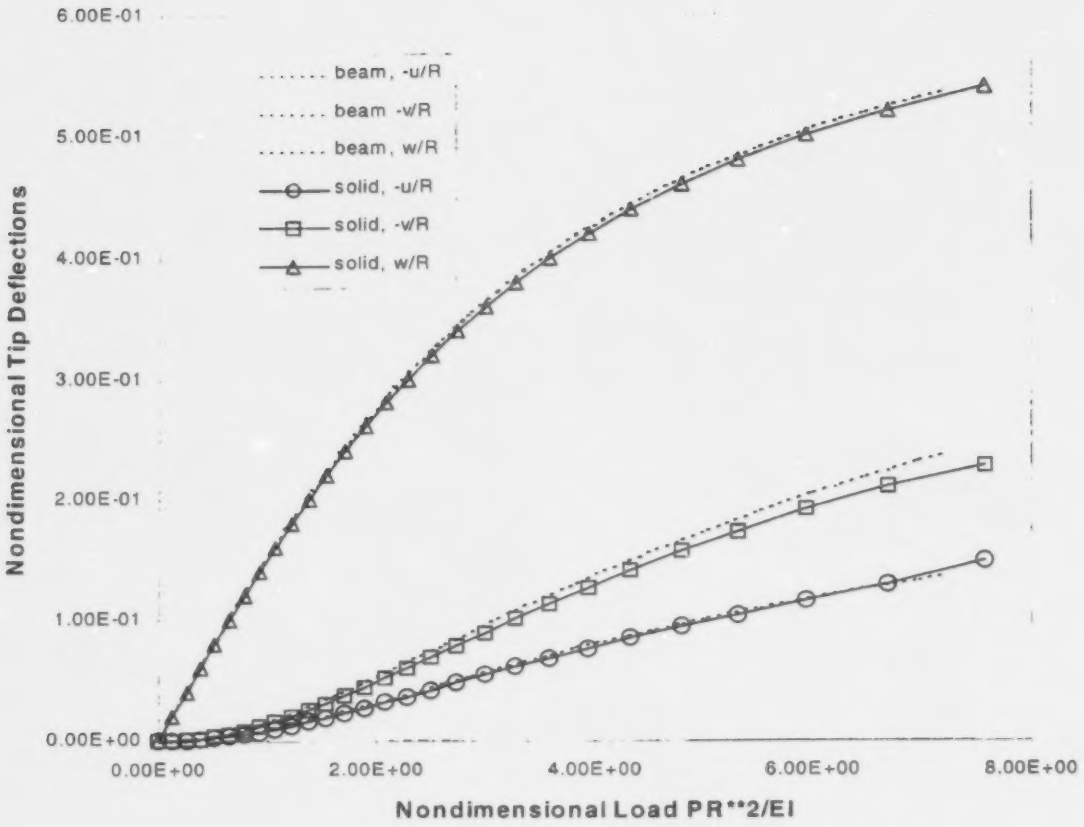

Figure 3.14: Comparison of Non-dimensionalized Load-Tip Deflection Curves of the Bend Obtained by Beam and Solid Elements.

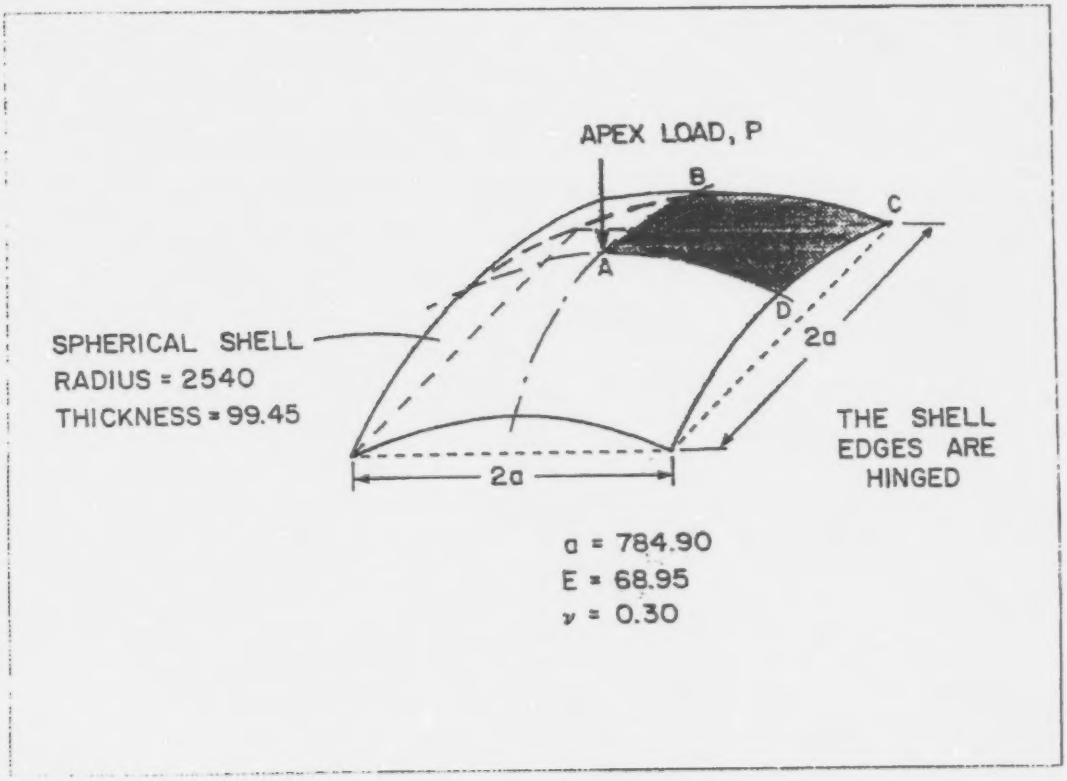

Figure 3.15: Problem Geometry, External Load and Boundary Conditions for Post-Buckling Analysis of a Hinged Spherical Shell.

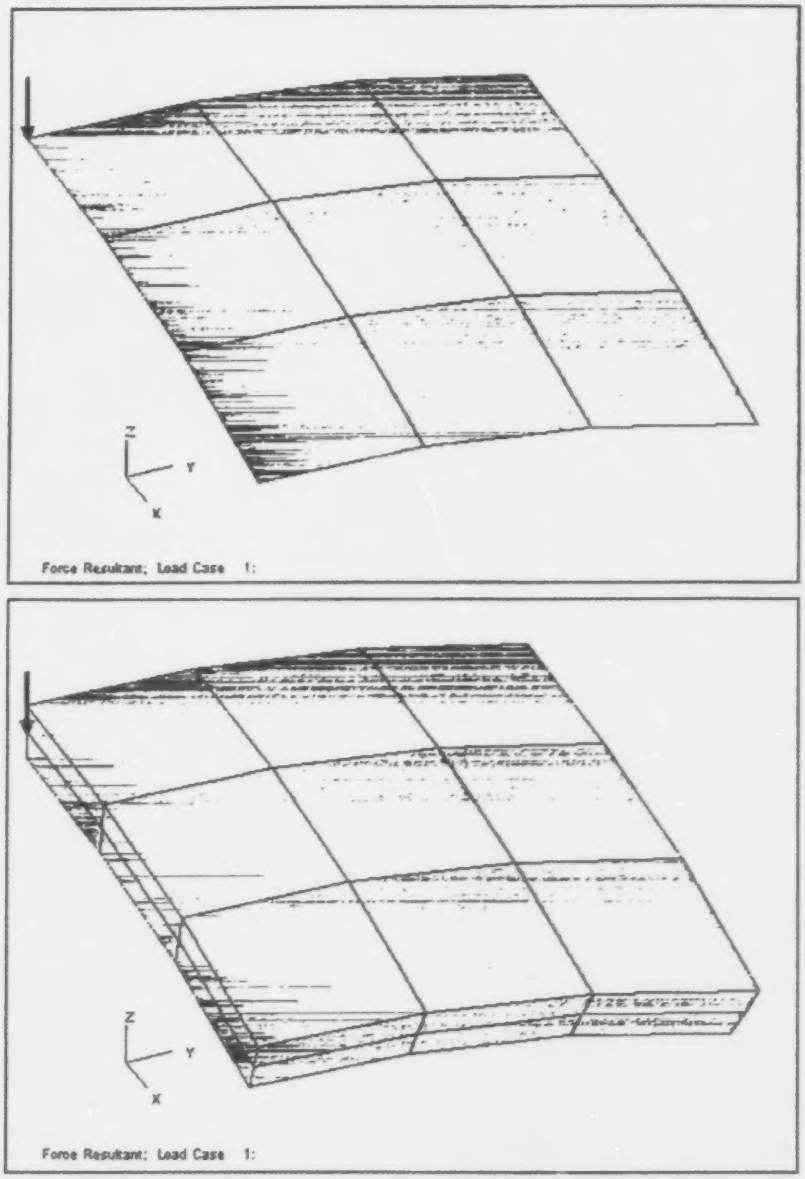

Figure 3.16: Finite Element Meshes for Post-Buckling Analysis of the Spherical Shell.
(a) 4-Noded Quadrilateral Shell Element, (b) 8-Noded Solid Element.

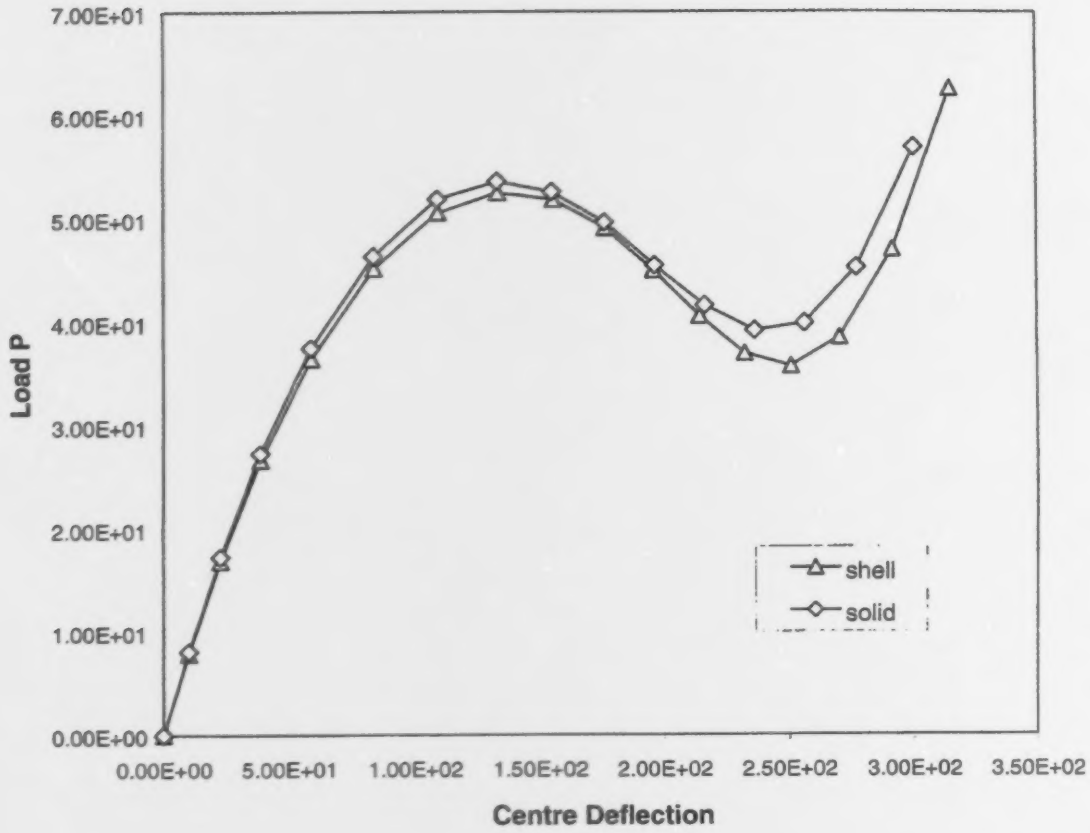

Figure 3.17: Comparison of Load-Center Deflection Curves of the Spherical Shell Predicted by Shell and Solid Elements.

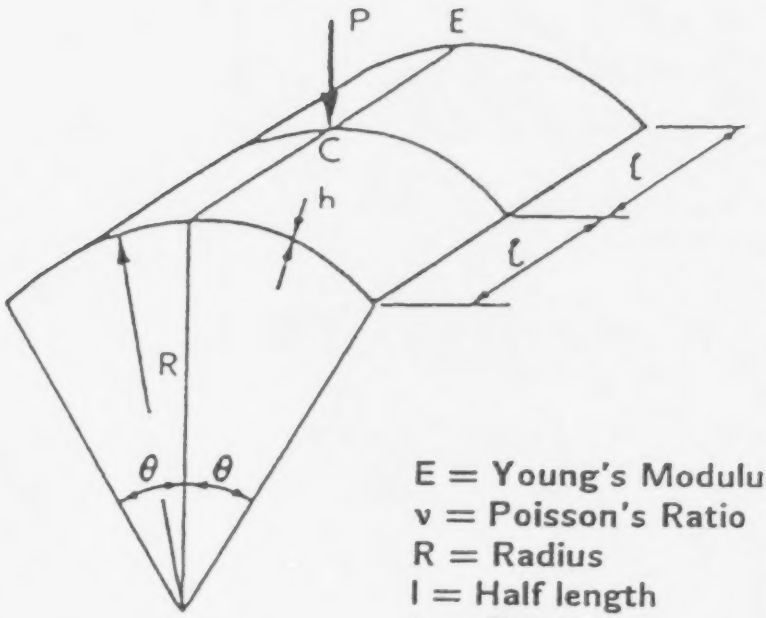

E = Young's Modulus = 3102.75
ν = Poisson's Ratio = 0.3
R = Radius = 2540
l = Half length = 254
h = Thickness = 12.7, 6.35
θ = Half angle = 0.1 rad.

Figure 3.18: Problem Geometry and External Load for Snap-Through and Snap-Back Analysis of a Hinged Shallow Cylindrical Shell Subjected to a Center Point Load.

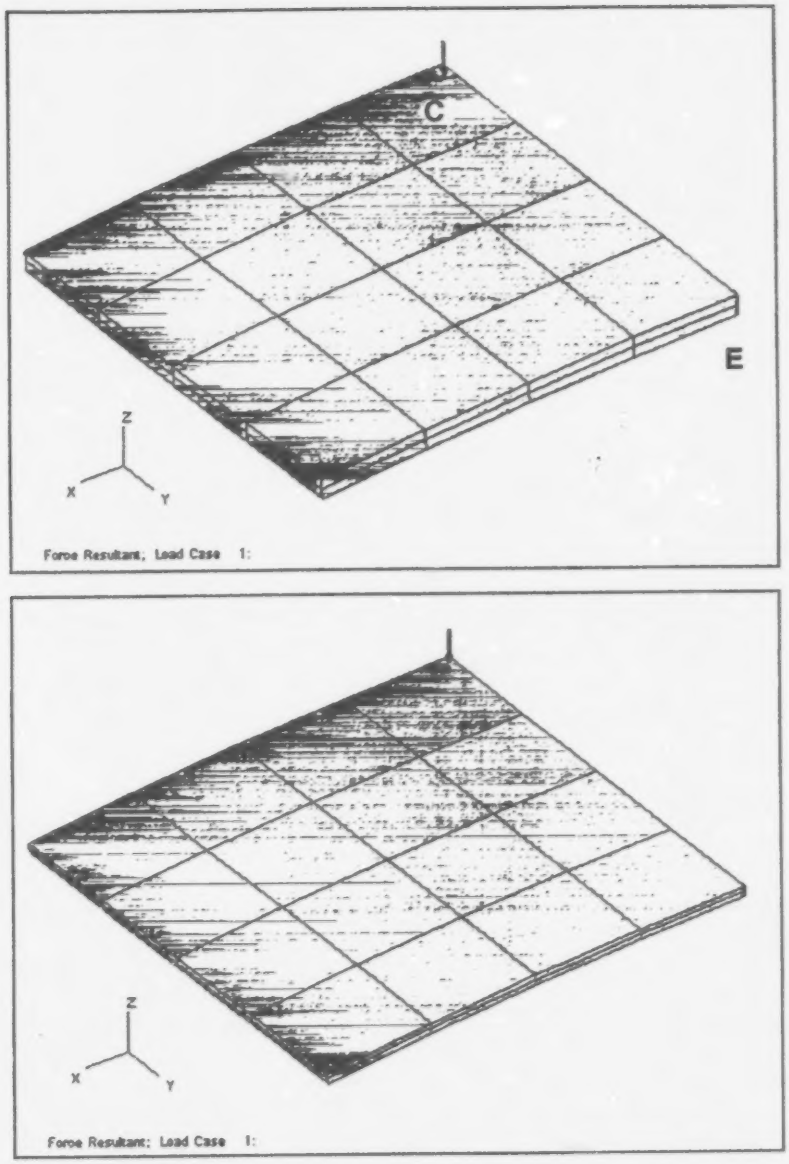

Figure 3.19: Solid Element Meshes for Post-Buckling Analysis of the Hinged Cylindrical Shell. (a) Shell Thickness t=12.7, (b) Shell Thickness t=6.35.

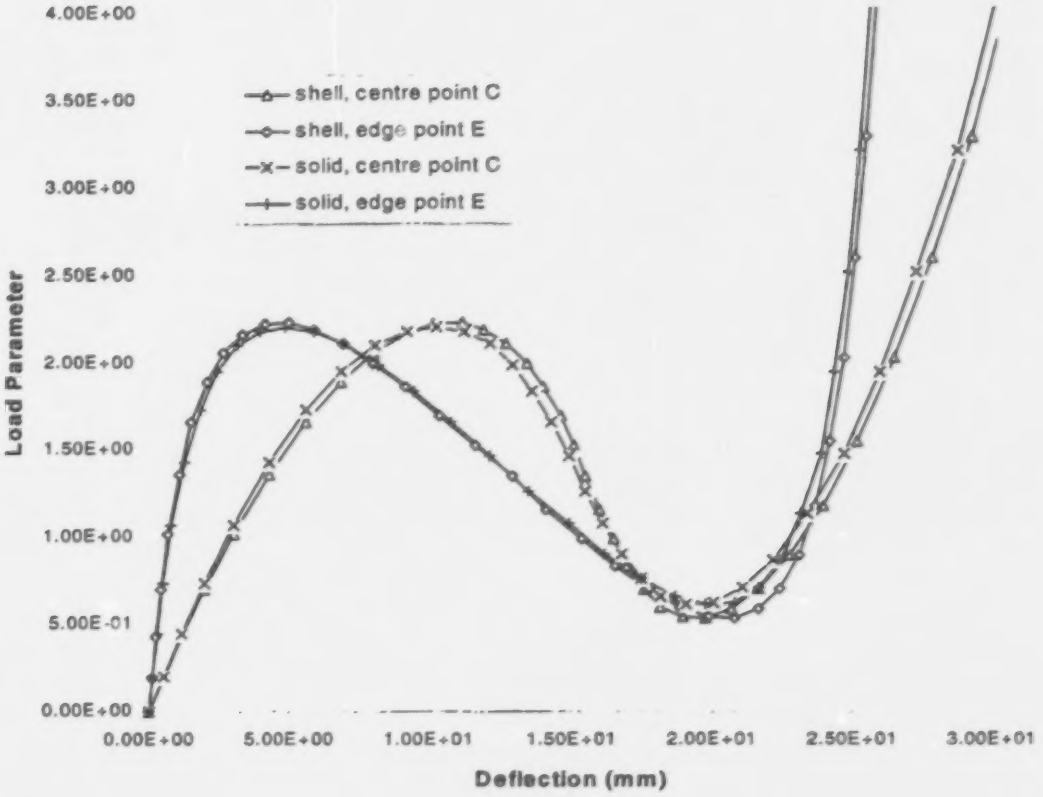

Figure 3.20: Comparison of Load-Center and Edge Deflection Curves of the Thicker Cylindrical Shell (t=12.7) Predicted by the Shell and Solid Elements.

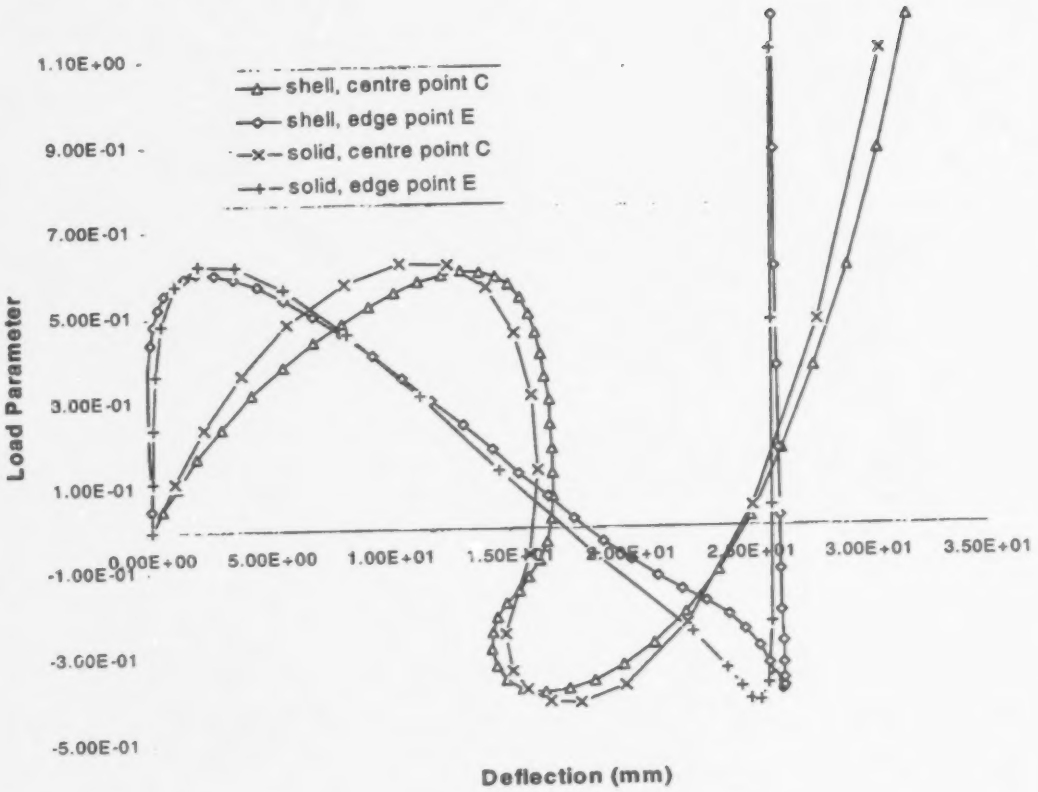

Figure 3.21: Comparison of Load-Center and Edge Deflection Curves of the Thinner Cylindrical Shell (t=6.35) Predicted by the Shell and Solid Elements.

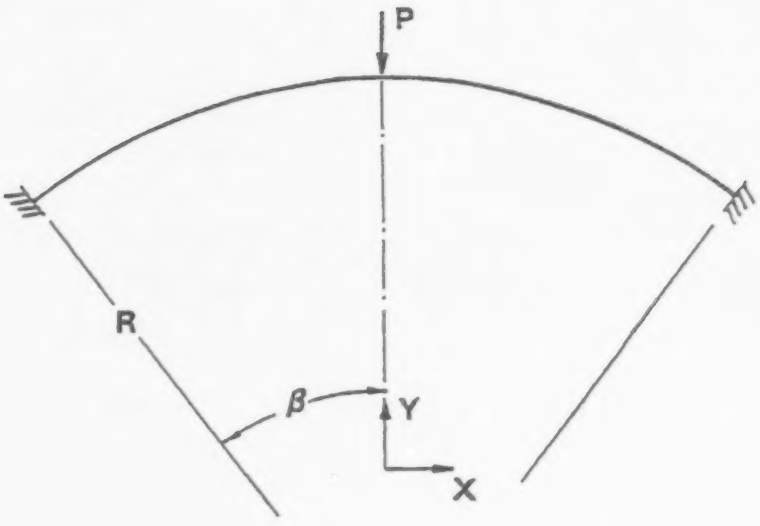

Figure 3.22: Problem Geometry, External Load and Boundary Conditions for General Nonlinear Analysis of a Clamped-Clamped Shallow Cylindrical Arch.

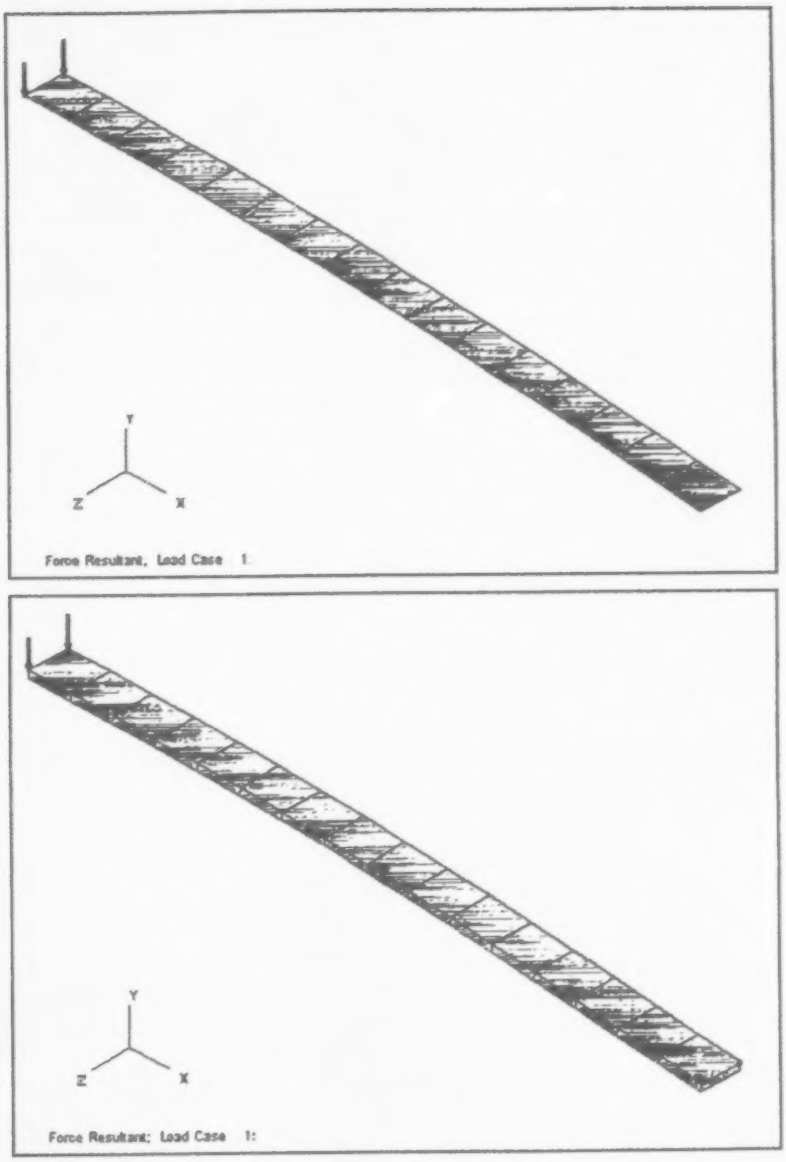

Figure 3.23: Finite Element Meshes for General Nonlinear Analysis of the Cylindrical Arch. (a) 4-Noded Shell Element, (b) 8-Noded Solid Element.

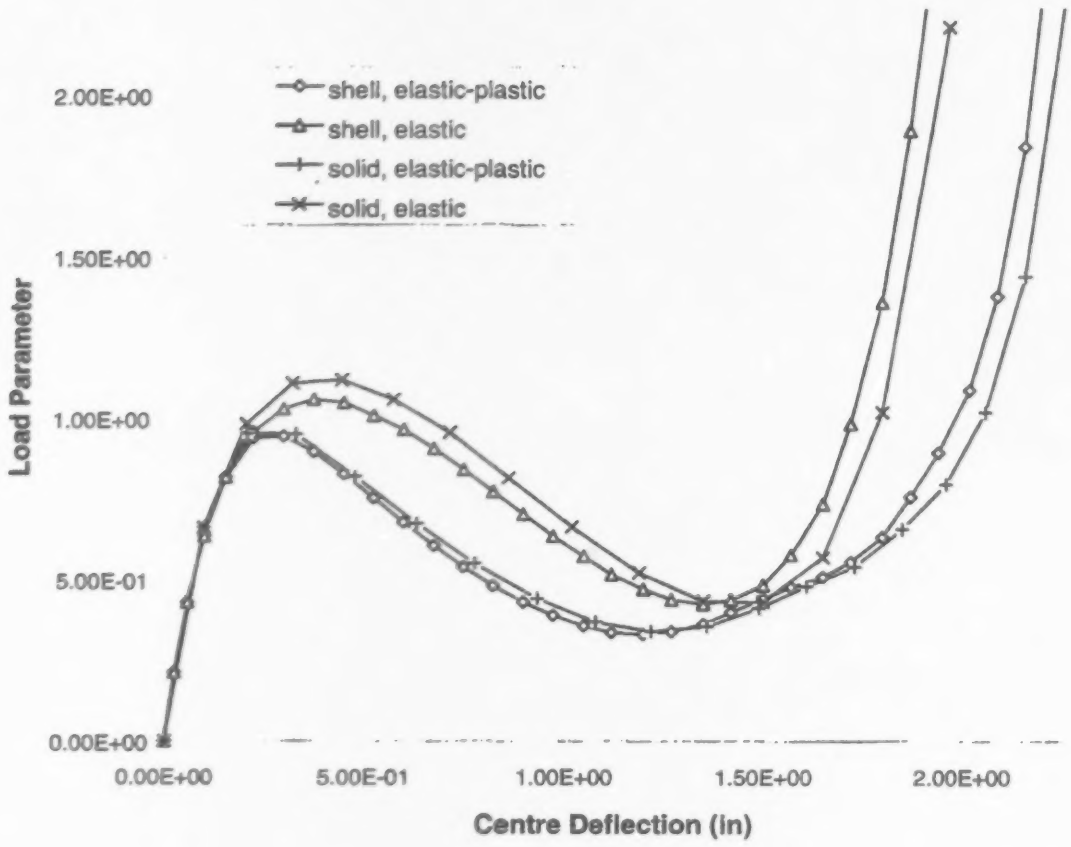

Figure 3.24: Comparison of Load-Center Deflection Curves of the Cylindrical Arch Predicted by the Shell and Solid Elements for Geometrically and Combined Nonlinear Situations.

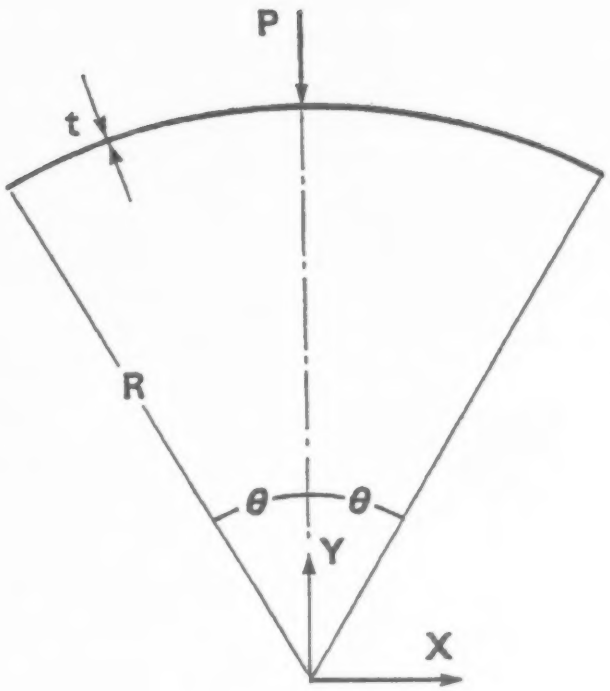

$E = 1.0 \times 10^7$ psi
$\nu = 0.3$
$\sigma_0 = 2.0 \times 10^4$ psi
$E_T = 1.0 \times 10^4$ psi
$R = 4.76$ in
$t = 0.01576$ in
$\theta = 10.9°$

Figure 3.25: Problem Geometry and External Loading Condition for Geometrically and Combined Nonlinear Analysis of a Shallow Spherical Shell.

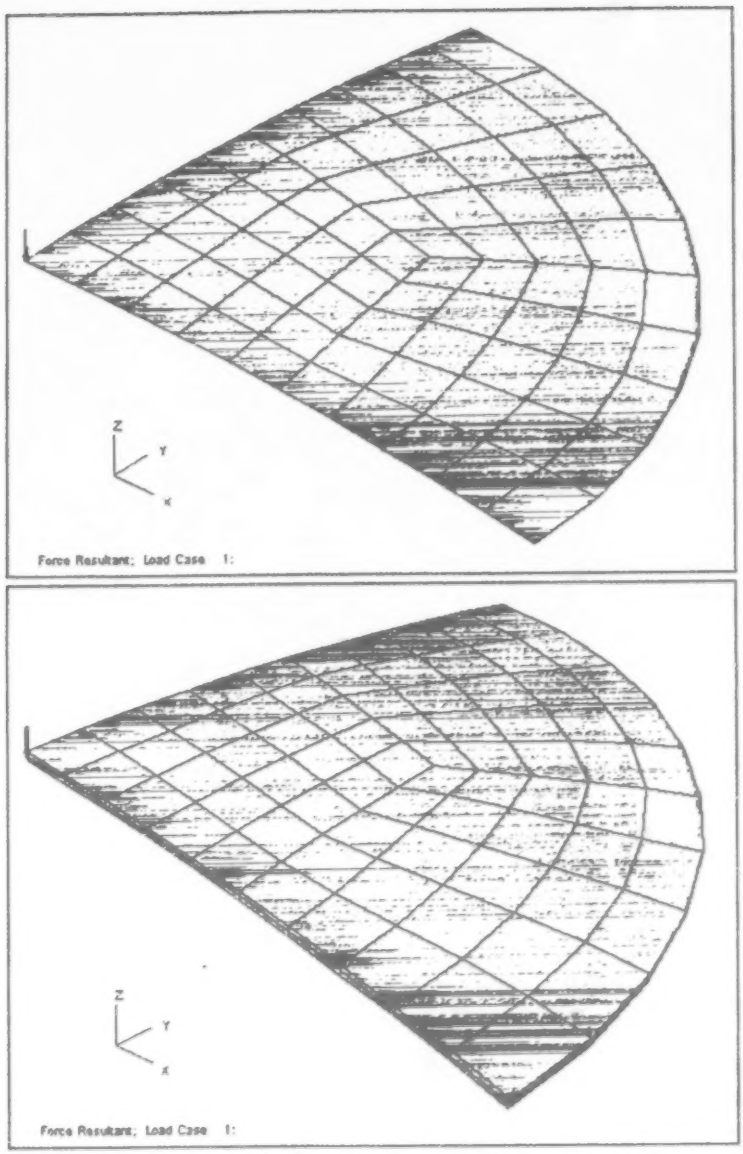

Figure 3.26: Finite Element Meshes for Nonlinear Analysis of the Shallow Spherical Shell. (a) 4-Noded Shell Element, (b) 8-Noded Solid Element.

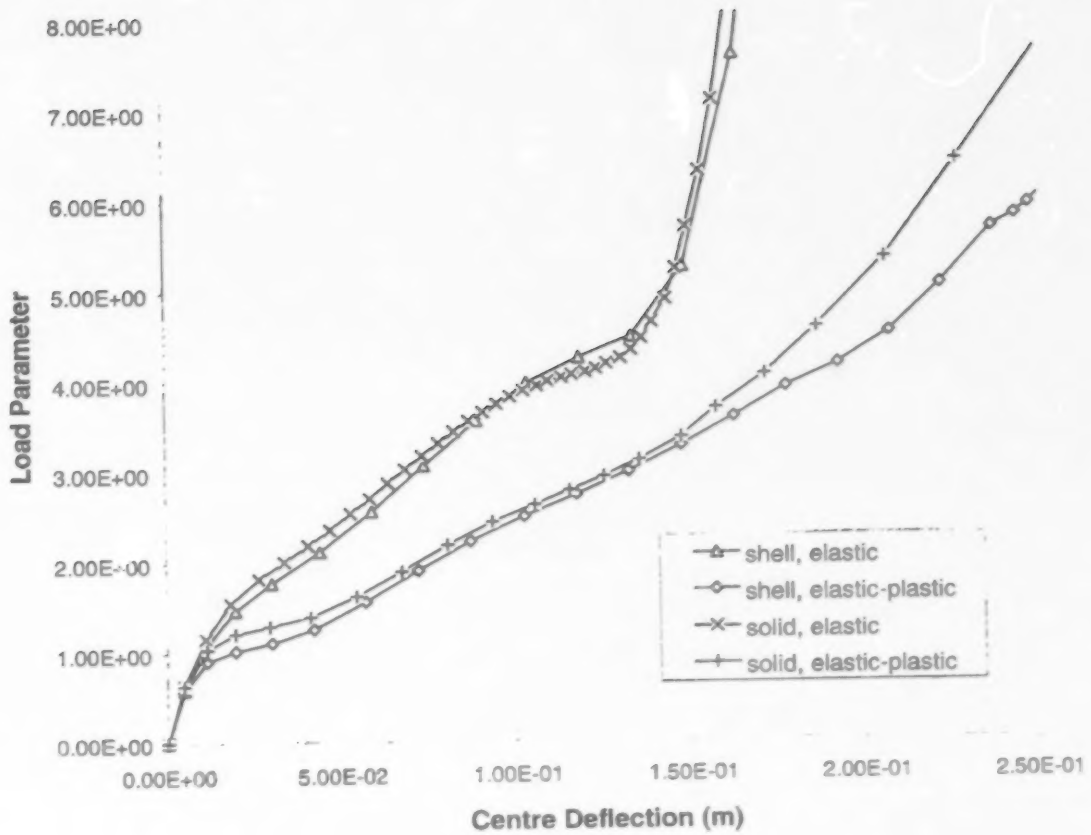

Figure 3.27: Comparison of Load-Center Deflection Curves of the Shallow Spherical Shell Predicted by the Shell and Solid Elements for Geometrically and Combined Nonlinear Situations With Clamped Boundary Conditions.

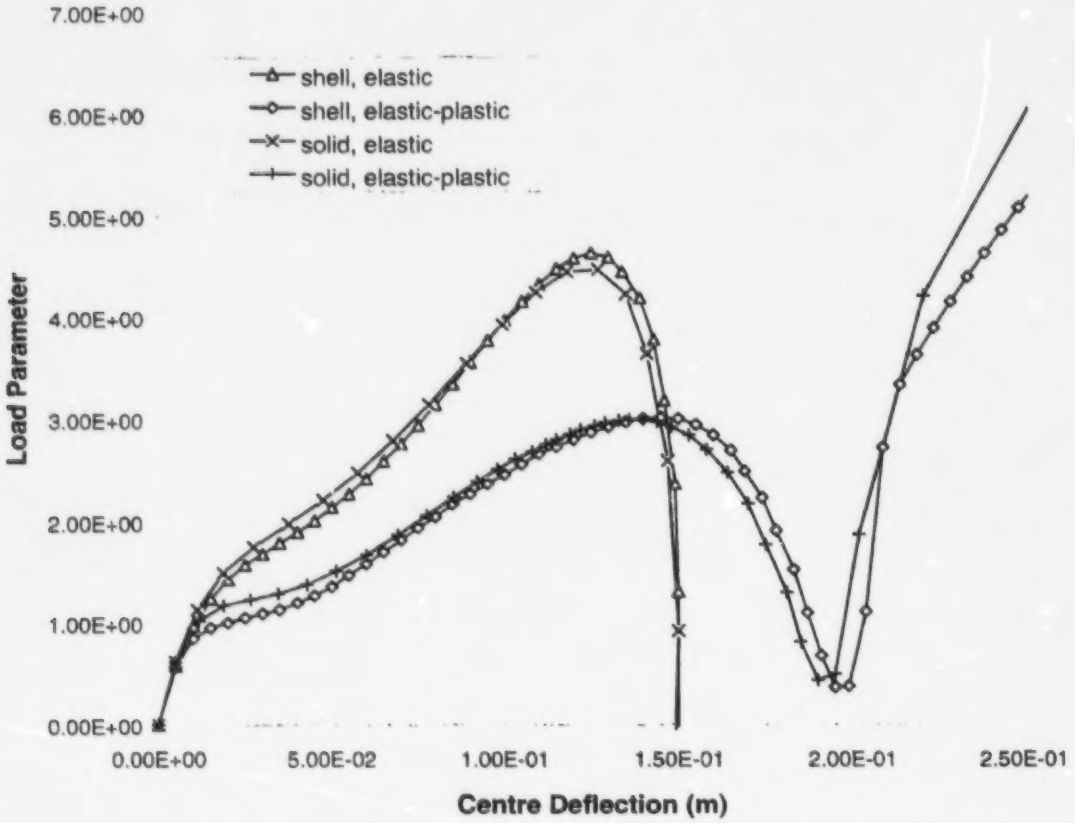

Figure 3.28: Comparison of Load-Center Deflection Curves of the Shallow Spherical Shell Predicted by the Shell and Solid Elements for Geometrically and Combined Nonlinear Situations With Hinged Boundary Conditions.

4. IMPLEMENTATION OF HYPERELASTIC MATERIAL MODEL INTO THE 8-NODED NONLINEAR SOLID ELEMENT

4.1 Rubber Materials and the Hyperelastic Material Model

The original material known as *rubber* was obtained in the form of latex from the tree *Hevea Braziliensis* [20]. In current usage, the word rubber was no longer restricted to the original natural rubber, but was applied to any materials having mechanical properties substantially similar to those of natural rubber, regardless of its chemical contents. The more modern term *elastomer* was often used in relation to synthetic materials having rubber-like properties.

In order to obtain an accurate mathematical representation of the general properties of the rubber-like materials, it was necessary to adopt a "phenomenological" method of approach, i.e. a method which was not based on molecular or structural concepts, but on purely mathematical considerations. This method involved finding the most general (or convenient) way for mathematically describing the material properties, rather than their explanation or interpretation in the molecular or physical sense. Various forms of phenomenological theory have been developed. They varied widely both in their generality and in their degree of sophistication. Some of the theories just described a particular stress-strain relation in mathematical form, while other theories attempted to relate arbitrary strain states on the basis of one or more fundamental postulates. In finite element analyses of rubber-like material, theories from the latter category must be employed. The term "hyperelastic model" often referred to those theories in which stresses were obtained by differentiating a strain energy function expressed in terms of the total strains.

The earliest significant phenomenological theory of large elastic deformation, which had a dominant influence on all the later developments in this field, is that of Mooney [21]. This theory was based on two assumptions:

a. That the rubber was incompressible, and isotropic in the unstrained state; and
b. The Hooke's law was obeyed in simple shear, or in a simple shear superimposed in a plane transverse to a prior uniaxial extension or compression.

Based on these assumptions, Mooney derived, by purely mathematical arguments involving considerations of symmetry, the strain energy function:

$$\phi = C_1\left(\lambda_1^2+\lambda_2^2+\lambda_3^2-3\right)+C_2\left(\lambda_1^{-2}+\lambda_2^{-2}+\lambda_3^{-2}-3\right) \tag{4.1}$$

which contained two elastic constants C_1 and C_2. This strain energy function included the well-known neo-Hookean model with C_2=0. However, through comparison with the experimental data, it had been found that the Mooney equation was quite inadequate as a general representation of the form of the strain energy function [20].

For complete specification of the mechanical properties of a rubber, the strain energy function must be formulated for a pure homogeneous strain of the most general type. The form of the general function, however, was restricted by some logical constraints and certain implied assumptions in the problem. From a basic assumption that the material was incompressible and isotropic in the unstrained state, Rivlin [22] obtained a more general strain energy function as the sum of a series of terms, as:

$$\phi = \sum_{i=0,\, j=0}^{\infty} C_{ij}\,(I_1-3)^i\,(I_2-3)^j \tag{4.2}$$

where I_1 and I_2 indicate the first and second strain invariants. After taking into account the incompressible conditions, they can be expressed as:

$$\begin{aligned} I_1 &= \lambda_1^2+\lambda_2^2+\lambda_3^2 \\ I_2 &= \lambda_1^{-2}+\lambda_2^{-2}+\lambda_3^{-2} \end{aligned} \tag{4.3}$$

However, in the absence of any prior knowledge, it was extremely difficult to select a set of terms and assign values to constants associated with these terms to represent the behaviour of an actual rubber material. From the considerations of mathematical simplicity, it is reasonable to assume that a small number of terms, corresponding to the lowest members of the series, would

predominate and the Mooney equation was the most general first-order relationship in I_1 and I_2. So if we restricted ourselves to a small range of variables, the Mooney equation should be used to achieve a fair approximation to the rubber material behavior.

Following the development of Mooney and Rivlin, numerous strain energy functions were proposed using the strain invariants. The complexity of some of the formulae was caused by the attempt to cover the region of very high strains. However, from the viewpoint of mathematical representation of the elastic properties of rubbers, it was possible to argue that the introduction of the strain invariants might itself be an unnecessary complication, and a formulation in terms of principal stretches might have greater advantages in mathematical simplicity.

An important new departure from earlier work was made by Ogden [23], who dispensed with the restriction to even powers of the principal stretches and wrote the strain energy function for a incompressible rubber in the form of the series:

$$\phi = \sum_n \frac{\mu_n}{\alpha_n}\left(\lambda_1^{\alpha_n} + \lambda_2^{\alpha_n} + \lambda_3^{\alpha_n} - 3\right) \tag{4.4}$$

in which the α_n might have any values, positive or negative, and are not necessarily integers. μ_n are material constants. It should be noticed that the Ogden's strain energy function covered the Mooney equation as a special case with:

$$n = 2, \quad \alpha_{1,} = 2, \quad \alpha_2 = -2 \quad \mu_1 = 2C_1, \quad \mu_2 = -2C_2 \tag{4.5}$$

The utility of a hyperelastic theory must be judged by its ability to represent the experimental data for rubber for all possible types of strain, preferably using a relatively small number of terms. The Ogden's model had been applied to the experimental results of Treloar [20] and the results were compared with those of the neo-Hookean and Mooney models in Figure 4.1 (reproduced from reference [23]). Using as few as three terms with the following material constants (μ in kg cm^{-2}):

$$\begin{aligned} \alpha_1 &= 1.3, \quad \alpha_2 = 5.0, \quad \alpha_3 = 2.0 \\ \mu_1 &= 6.3, \quad \mu_2 = 0.012, \quad \mu_3 = 0.1 \end{aligned} \tag{4.6}$$

the stress-strain curves resulting from the Ogden's strain energy function fitted the experimental data very closely up to a stretch of 7.0. The inadequacy of the neo-Hookean and Mooney models are also clearly revealed in these figures.

Because the Ogden's hyperelastic model can represent the experimentally measured stress-strains curves accurately in various strain conditions, and it also included the commonly used neo-Hookean and Mooney-Rivlin models as special cases, it had been selected for implementation into the VAST program in the present contract.

4.2 Theoretical Derivation of Stresses and Tangent Modulus Matrix for the Ogden's Hyperelastic Material Model

Since the Ogden's strain energy function cannot be easily expressed in strain invariants, it is normally more convenient to work directly with the principal stretches. A number of principal stretch-based large strain finite element formulations have been proposed [24-28]. Most of them dealt with hyperelastic material models for the membrane elements, in which the plane stress assumption was always adopted. In the plane stress situation, the incompressible condition can be conveniently achieved by eliminating the through-the-thickness stretch component from the strain energy function. However, this advantage disappeared in the general three-dimensional stress-strain state.

In 3D problems, if the strain energy function in Equation (4.4) was employed, the resulting incompressible hyperelastic constitutive equations involved a hydrostatic pressure term, which was not directly related to the element strains and could only be determined by appropriate stress boundary conditions. Although various mixed finite element formulations, which solved both the hydrostatic pressure and displacements simultaneously, had been proposed and successfully applied to numerous engineering problems [24, 29], their implementation into the VAST finite element program was not straightforward and required considerable restructuring of the computer code throughout the entire program. Alternatively, purely displacement-based finite

element formulations were developed using near-incompressible strain energy functions, which included an additional penalty term in the conventional Ogden's formulation to enforce the volumetric strain to unity [11]:

$$\phi = \sum_n \frac{\mu_n}{\alpha_n}\left(\bar{\lambda}_1^{\alpha_n} + \bar{\lambda}_2^{\alpha_n} + \bar{\lambda}_3^{\alpha_n} - 3\right) + \frac{K}{2}(J-1)^2 \tag{4.7}$$

where the bulk modulus, K, is used as the penalty parameter, and the principal stretches are normalized using the volumetric strain, $J=\lambda_1\lambda_2\lambda_3$, as:

$$\bar{\lambda}_i = \lambda_i J^{-\frac{1}{3}} \tag{4.8}$$

The use of normalized stretches resulted in separated volumetric and deviatoric strain energies. This particular form of Ogden's strain energy function was adopted in the present implementation.

In the present nonlinear 8-noded solid element, element stresses were computed in four steps. First of all, the total Biot strains was computed at each numerical integration point. The principal strains and their directions were then obtained by solving a local eigenvalue problem. These principal strains were subsequently converted into principal stretches and utilized to compute the principal Biot stresses with respect to the principal axes as:

$$\sigma_{bi} = \frac{\partial \phi}{\partial \lambda_i} = \frac{1}{3\lambda_i}\sum_n \mu_n J^{-\frac{\alpha_n}{3}}\left(2\lambda_i^{\alpha_n} - \lambda_j^{\alpha_n} - \lambda_k^{\alpha_n}\right) + \frac{K}{\lambda_i}J(J-1) \tag{4.9}$$

with cyclic permutation of 1, 2 and 3 for the subscript i, j and k. Finally, the principal stresses were transformed back to the original system in which the element strains were first calculated.

In order to formulate the tangent stiffness matrix for incremental-iterative finite element solutions, the first-order elastic modulus matrix must be generated. In the present principal stretch-based formulation, this matrix was also first formulated in the principal directions as:

$$\mathbf{C}=\begin{bmatrix} C_{11} & C_{12} & C_{13} & 0 & 0 & 0 \\ C_{21} & C_{22} & C_{23} & 0 & 0 & 0 \\ C_{31} & C_{32} & C_{33} & 0 & 0 & 0 \\ 0 & 0 & 0 & C_{44} & 0 & 0 \\ 0 & 0 & 0 & 0 & C_{55} & 0 \\ 0 & 0 & 0 & 0 & 0 & C_{66} \end{bmatrix} \tag{4.10}$$

and subsequently transformed to the desired system through standard coordinate transformation. The upper 3x3 matrix of the tangent moduli was evaluated by differentiating the principal stresses with respect to the principal strains as:

$$\begin{aligned} C_{ii} &= \frac{\partial \sigma_{bi}}{\partial \lambda_i} = \frac{1}{3\lambda_i^2}\sum_n \alpha_n \mu_n J^{-\frac{\alpha_n}{3}}\left[\left(\frac{4}{3}-\frac{2}{\alpha_n}\right)\lambda_i^{\alpha_n}+\left(\frac{1}{3}+\frac{1}{\alpha_n}\right)\left(\lambda_j^{\alpha_n}+\lambda_k^{\alpha_n}\right)\right]+\frac{1}{\lambda_i^2}KJ^2 \\ C_{ji} &= C_{ij} = \frac{\partial \sigma_{bi}}{\partial \lambda_j} = \frac{1}{9\lambda_i\lambda_j}\sum_n \alpha_n \mu_n J^{-\frac{\alpha_n}{3}}\left(\lambda_k^{\alpha_n}-2\lambda_i^{\alpha_n}-2\lambda_j^{\alpha_n}\right)+\frac{KJ}{\lambda_i\lambda_j}(2J-1) \end{aligned} \tag{4.11}$$

where subscript i, j and k are still cyclic permutations of 1, 2 and 3. The shear tangent modulus components, could be obtained as [23]:

$$\begin{aligned} C_{44} &= \frac{(\sigma_{b1}-\sigma_{b2})}{2(\lambda_1-\lambda_2)} \\ C_{55} &= \frac{(\sigma_{b2}-\sigma_{b3})}{2(\lambda_2-\lambda_3)} \\ C_{66} &= \frac{(\sigma_{b3}-\sigma_{b1})}{2(\lambda_3-\lambda_1)} \end{aligned} \tag{4.12}$$

If repeated principal stretches exist, say $\lambda_1=\lambda_2$, the tangent shear modulus could be evaluated as:

$$\begin{aligned} C_{44} &= \lim_{\lambda_1\to\lambda_2}\frac{(\sigma_{bi}-\sigma_{b2})}{2(\lambda_1-\lambda_2)} = \frac{1}{2}\left(\frac{\partial \sigma_{bi}}{\partial \lambda_1}-\frac{\partial \sigma_{b2}}{\partial \lambda_1}\right) \\ &= \frac{1}{2\lambda_1^2}\sum_n \alpha_n \mu_n\left[\lambda_1^{\alpha_n}-\frac{1}{3\alpha_n}\left(\lambda_1^{\alpha_n}-\lambda_3^{\alpha_n}\right)\right]J^{-\frac{\alpha_n}{3}}+\frac{1}{2\lambda_1^2}KJ(1-J) \end{aligned} \tag{4.13}$$

The other two tangent shear modulus components could also be obtained by a similar approach.

To start a nonlinear analysis with hyperelastic material, the ground state constitutive matrix, which is the tangent moduli evaluated about the initial undeformed configuration, must be used. This initial tangent modulus matrix was obtained by substituting principal stretches, $\lambda_1=\lambda_2=\lambda_3=1$, into Equations (4.11) and (4.13) which resulted in

$$\mathbf{C}^0=\left(K-\frac{2}{3}\mu\right)\begin{bmatrix}1&1&1&0&0&0\\1&1&1&0&0&0\\1&1&1&0&0&0\\0&0&0&0&0&0\\0&0&0&0&0&0\\0&0&0&0&0&0\end{bmatrix}+\mu\begin{bmatrix}2&0&0&0&0&0\\0&2&0&0&0&0\\0&0&2&0&0&0\\0&0&0&1&0&0\\0&0&0&0&1&0\\0&0&0&0&0&1\end{bmatrix} \tag{4.14}$$

where the shear modulus, μ, relates to the material constants of the Ogden's strain energy function as:

$$\mu=\frac{1}{2}\sum_n \alpha_n\mu_n \tag{4.15}$$

It should be noticed that the ground state constitutive matrix given in Equation (4.14) coincided with the linear elastic constitutive equations. This fact partially verified the present derivation.

4.3 Implementation of the Ogden's Hyperelastic Model into the VAST Program

During the present development of the hyperelastic solid element capability in VAST, it became apparent that the only section of computer code that depended on the particular selection of constitutive models was that for the computation of the first and second derivatives of the strain energy function with respect to the principal stretches. These derivatives are required in the calculation of the principal stresses and the tangent modulus matrix in the principal directions, respectively. In the present work, we carried out these differentiations analytically for the near-incompressible Ogden's strain energy function discussed earlier, and programmed all of them into

a single subroutine. This subroutine can be viewed as a user supplied subroutine, since when new hyperelastic material models are incorporated in the future, this will be the only subroutine which needs to be modified.

4.4 Numerical Verification

4.4.1 Thick Hyperelastic Cylinder Under Internal Pressure

In order to verify the newly developed 8-noded hyperelastic solid element, we first considered plane strain expansion of a thick rubber cylinder under uniform internal pressure. This test problem had been previously studied by Duffett and Reddy [24] and Moita [11], using a mixed pressure-displacement formulation and the co-rotational method, respectively. Good agreement between these solutions up to a stretch of 5.0 at the inner surface had been reported for various material constants.

In the present analysis, geometric and material properties were all specified in non-dimensional form, following the reference solutions presented in [11,24]. Four sets of material constants were considered, including (1) a three-term Ogden's strain energy function; (2) a two-term Ogden's strain energy function; (3) a one-term Ogden's strain energy function and (4) a Mooney-Rivlin strain energy function. The material parameters for these hyperelastic models are summarized in Table 4.1.

With regard to geometry, the inner radius and thickness of this rubber cylinder were 1.0 and 0.1764, respectively. In order to take into account the change of the inner surface area during the large strain deformation, the follower force capability was used in the present analysis to repeatedly update the external force vector. Due to symmetry in this problem, only a quarter of the cylinder was included in the finite element model.

A 10x2x1 8-noded solid element mesh, as shown in Figure 4.2, was first utilized. Symmetry boundary conditions were applied at both ends and the translational degrees-of-freedom in the z-direction were constrained over the entire model to achieve the plane-strain condition. A

unit pressure load was applied at the inner surface of the cylinder as is also shown in Figure 4.2. Using the newly developed hyperelastic solid element, pressure-displacement curves were obtained for the three-term Ogden's strain energy function with three different bulk modulus to shear modulus ratios. The VAST results are compared with the solution of Duffett and Reddy [24] in Figure 4.3, in which the VAST solution with a K/μ ratio of 100 is in close agreement with the published result. However, in all three VAST analyses, convergence problems appeared suddenly at an inner surface displacement around 1.4, which corresponded to a local strain of 140%. To eliminate the possibility that these failures of VAST analyses were related to the coarseness of the finite element mesh, a finer mesh containing 100 elements was generated. The boundary condition and pressure load applied on the fine mesh are displayed in Figures 4.4. Similar to the coarse mesh runs, the analyses with the fine mesh also failed to converge at about the same level of deformation as shown in Figure 4.5. It is interesting to note that with the incompatible (bubble) displacement modes turned on, the VAST analyses failed in the same manner, but at a much earlier stage of deformation corresponding to an inner surface displacement of about 0.4. This is probably related to the simplified treatment of the internal variables for nonlinear analysis.

The effect of material properties on pressure-displacement characteristics of the rubber cylinder was then investigated, and the VAST solutions are compared with the reference results in Figure 4.6 for all four sets of material constants. Except for the Mooney-Rivlin material model, VAST program still experienced convergence difficulties shortly after the peak load levels were passed. However, for all these material constants, the portion of solutions successfully obtained by VAST were consistently in excellent agreement with the published results [24].

4.4.2 Frequency Response Analysis of the Pre-Stressed Engine Mount Model

At this point, we reconsidered the engine mount model studied earlier in the current contract. In the previous nonlinear analyses using the ANSYS program, a highly simplified engine mount model had been utilized, in which the metal plates were eliminated and only the rubber core was included in the finite element analysis. The same model, which included a 4x4x2 mesh of the 8-noded solid elements as shown in Figure 4.7, was also used in the present analyses.

A Mooney-Rivlin model with material constants, C_1=0.552 MPa and C_2=0.138 MPa, was used to represent the rubber core material. Using these constants, the shear modulus at the ground state was obtained as 1.38 MPa. Assuming the Poisson's ratio as 0.49, the ground state Young's and bulk moduli were 4.1124 MPa and 69 MPa, respectively. This ground state Young's modulus was in good correlation with the experimentally measured material property of the engine mount material provided by the Dockyard Lab of DREA [6].

For frequency response analyses, a unit point load was applied at the center of the top surface as shown in Figure 4.7(a). The bottom surface was fully constrained against translations in the z-direction, however, only minimum boundary conditions were applied in the x-y plane as shown in Figure 4.7(b). The frequency responses at the loaded point obtained without and with visco-elastic material damping are presented as dark solid lines in Figures 4.8 and 4.9, respectively.

The initial static compression was then considered using the nonlinear hyperelastic model. The application of a uniform pressure of 1.675 MPa on the top surface resulted in an approximately 27% reduction on the thickness of the rubber block. The resulting vertical and horizontal displacements are plotted in Figure 4.10 against the load parameter. Using the tangent stiffness matrix generated based on the nonlinear analysis results, the frequency responses at the center of the top surface are again calculated with and without material damping. These results are also presented in Figures 4.8 and 4.9 as lighter solid lines. The comparison of the frequency response results obtained with and without the static compression clearly indicated that when proper nonlinear elastic material model was utilized, the inclusion of the effect of the pre-stress did increase the total stiffness of the rubber block.

This example indicated the effectiveness of the hyperelastic solid element in characterizing the dynamic behaviors of visco-elastic rubber materials under large initial static compression. However, further investigations and tests on this newly developed VAST element are still required before it can be applied to general engineering problems with confidence.

Table 4.1: Material Constants Employed in the Analysis of the Thick Rubber Cylinder Under Uniform Internal Pressure

Hyperelasticity Model	$\mu 1$	$\mu 2$	$\mu 3$	$\alpha 1$	$\alpha 2$	$\alpha 3$
3-term Ogden's Model	1.491	0.003	-0.023	1.3	5.0	-2.0
2-term Ogden's Model	1.528	0.0028	0.0	1.3	5.0	0.0
1-term Ogden's Model	1.667	0.0	0.0	1.2	0.00	0.0
Mooney-Rivlin Model	0.983	-0.170	0.0	2.0	-2.0	0.0

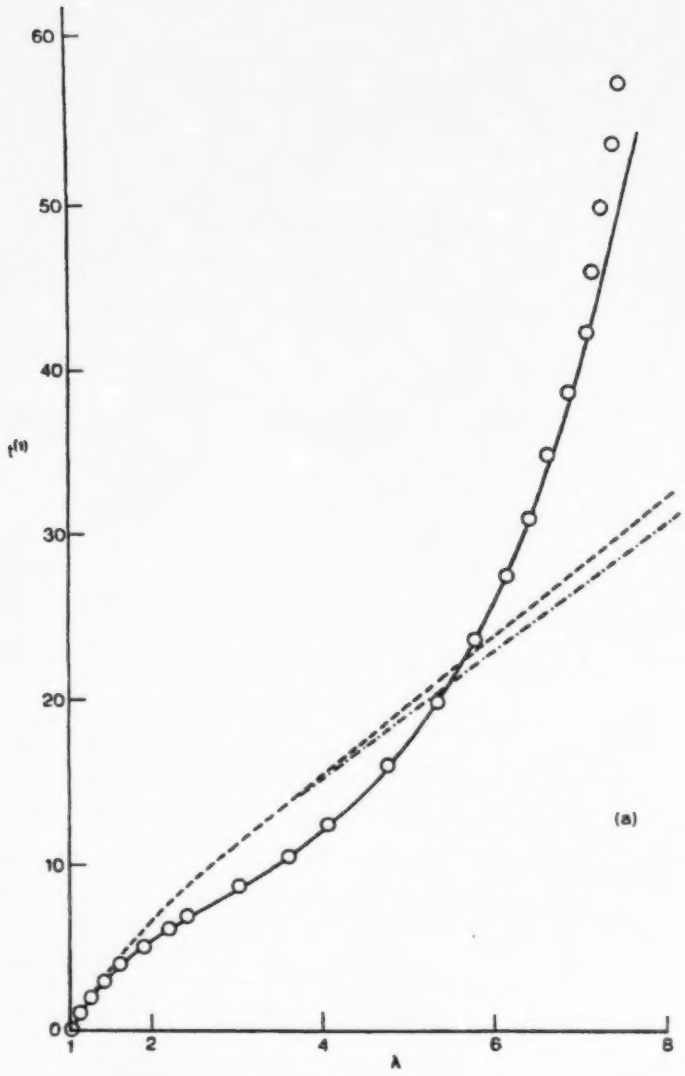

Figure 4.1: Comparison of Treloar's Experimental Data with the Predictions of the neo-Hookean (----), Mooney-Rivlin (-.-.-) and Ogden's (—) Strain Energy Functions (Reproduced From Reference [21]). (a) Simple Tension.

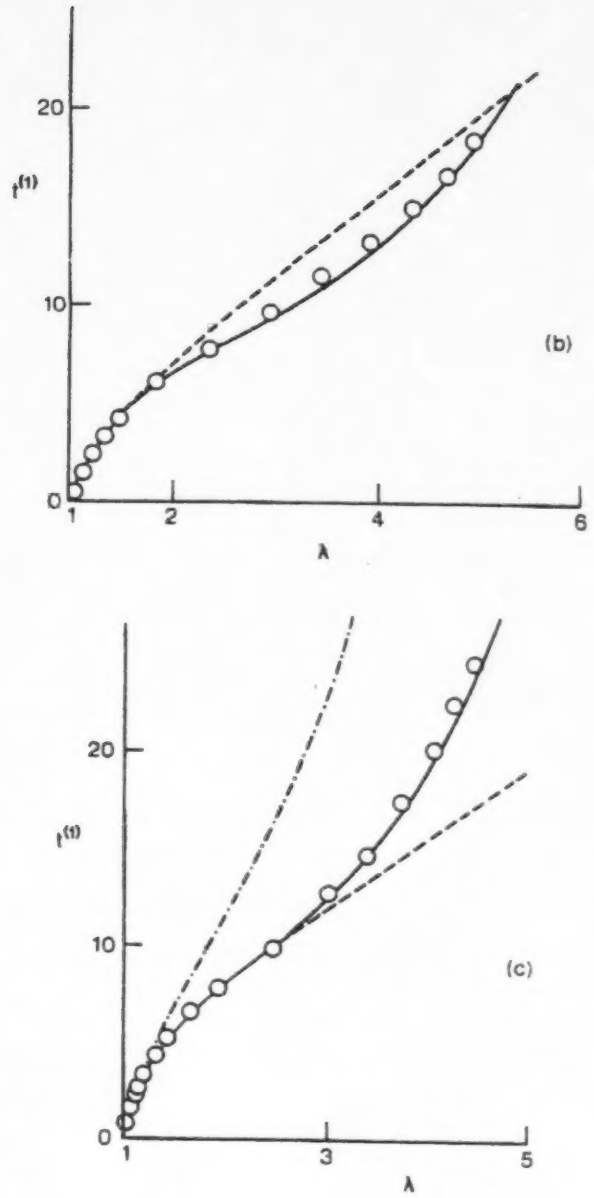

Figure 4.1 (Continued): Comparison of Treloar's Experimental Data with the Predictions of the neo-Hookean (----), Mooney-Rivlin (-.-.-) and Ogden's (—) Strain Energy Functions (Reproduced From Reference [21]). (b) Pure Shear, (c) Equibiaxial Shear.

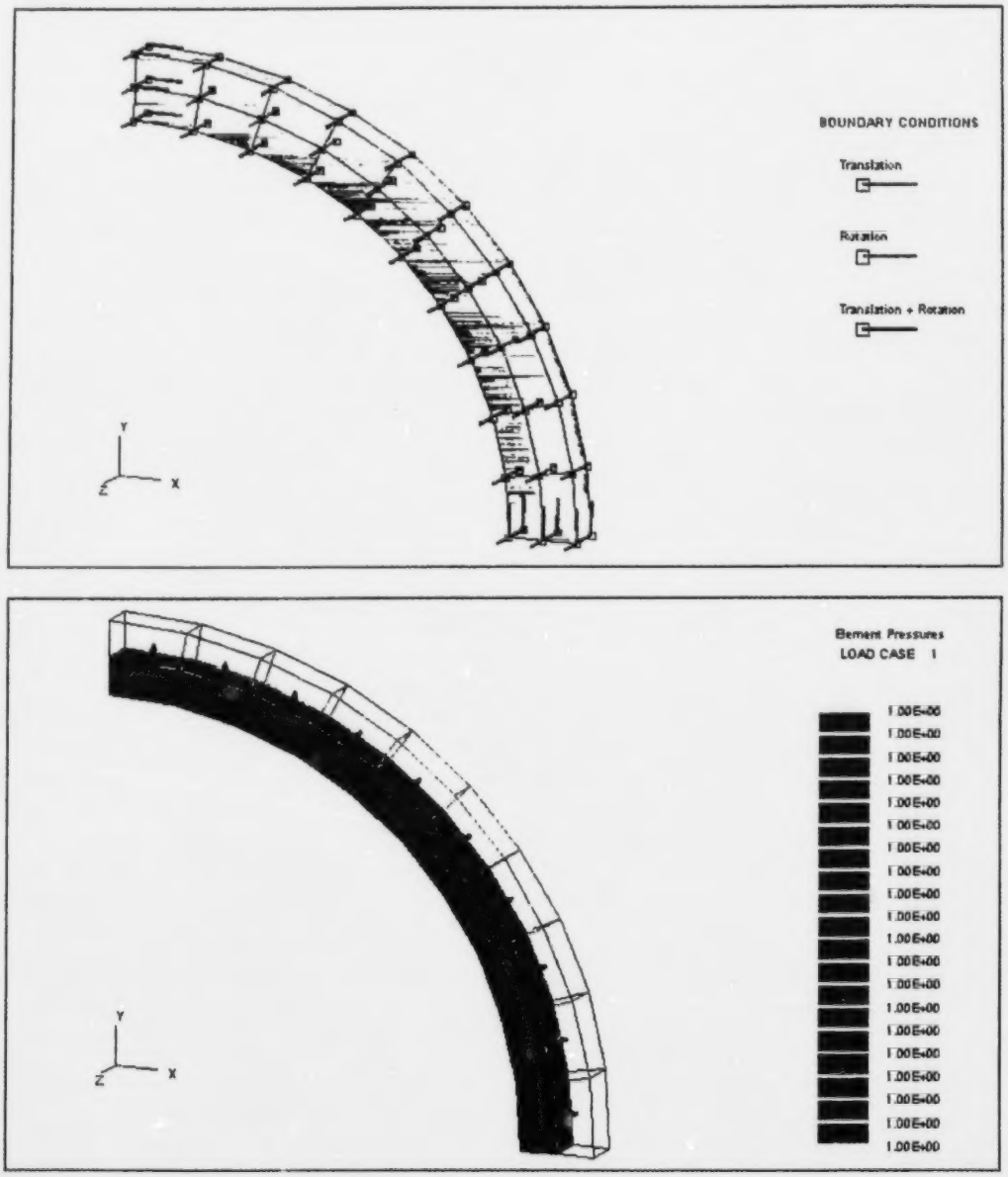

Figure 4.2: Coarse Finite Element Mesh for Plane Strain Expansion of a Thick Rubber Cylinder Under Internal Pressure. (a) Boundary Constraints and (b) Loading Condition.

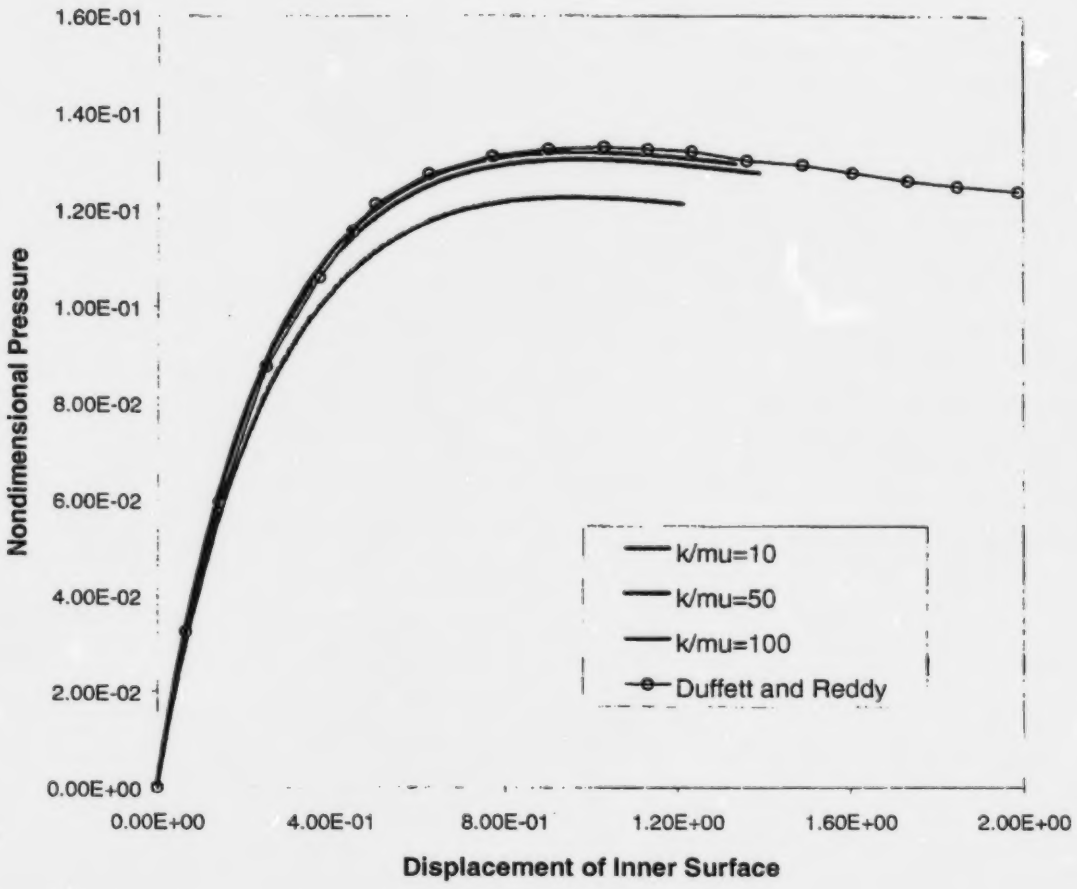

Figure 4.3: Comparison of the Reference Solution and the VAST Predictions Using the Coarse Mesh and Various Values of Bulk Modules for the Plane Strain Expansion of the Thick Rubber Cylinder.

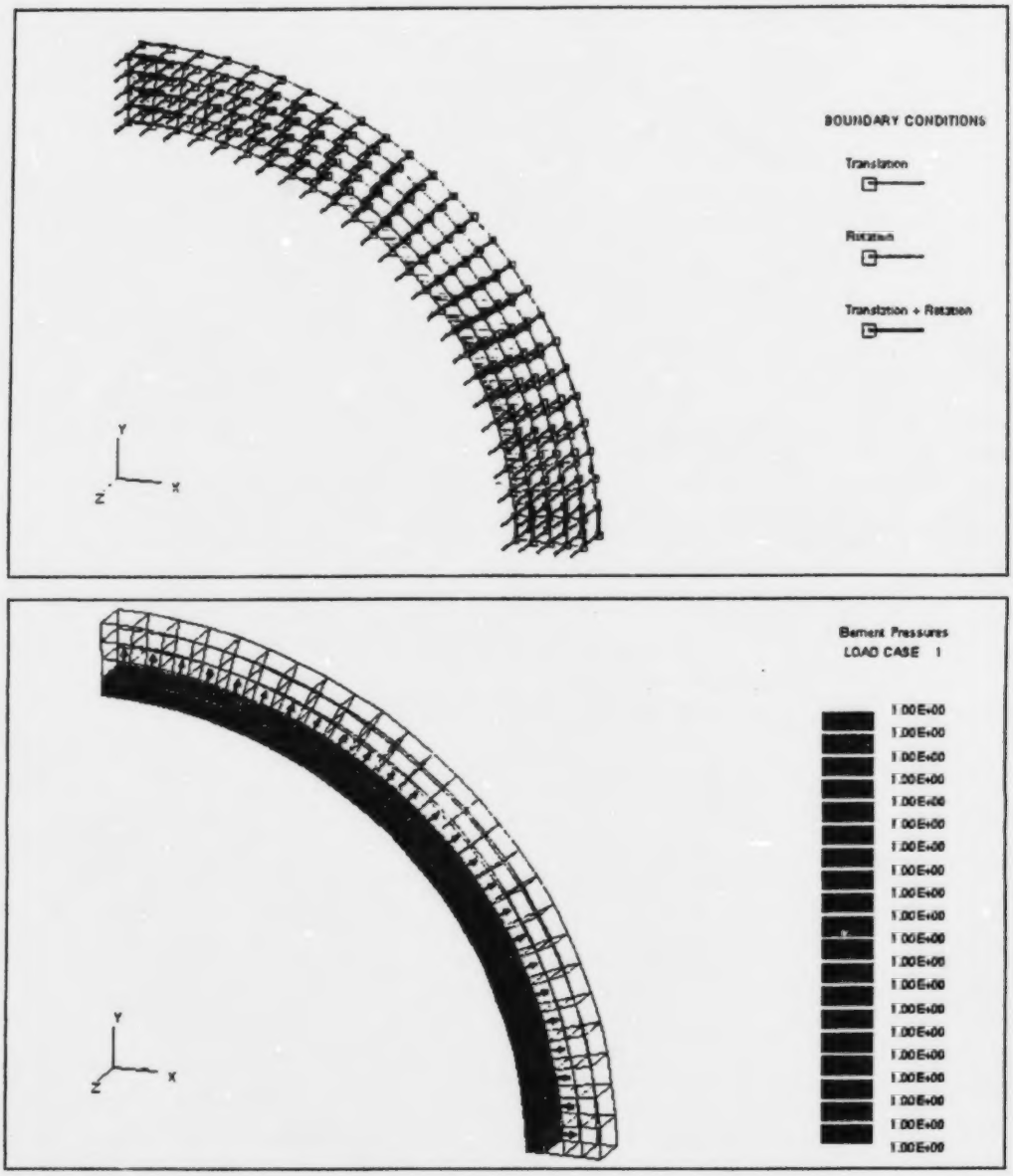

Figure 4.4: Fine Finite Element Mesh for Plane Strain Expansion of a Thick Rubber Cylinder Under Internal Pressure. (a) Boundary Constraints and (b) Loading Condition.

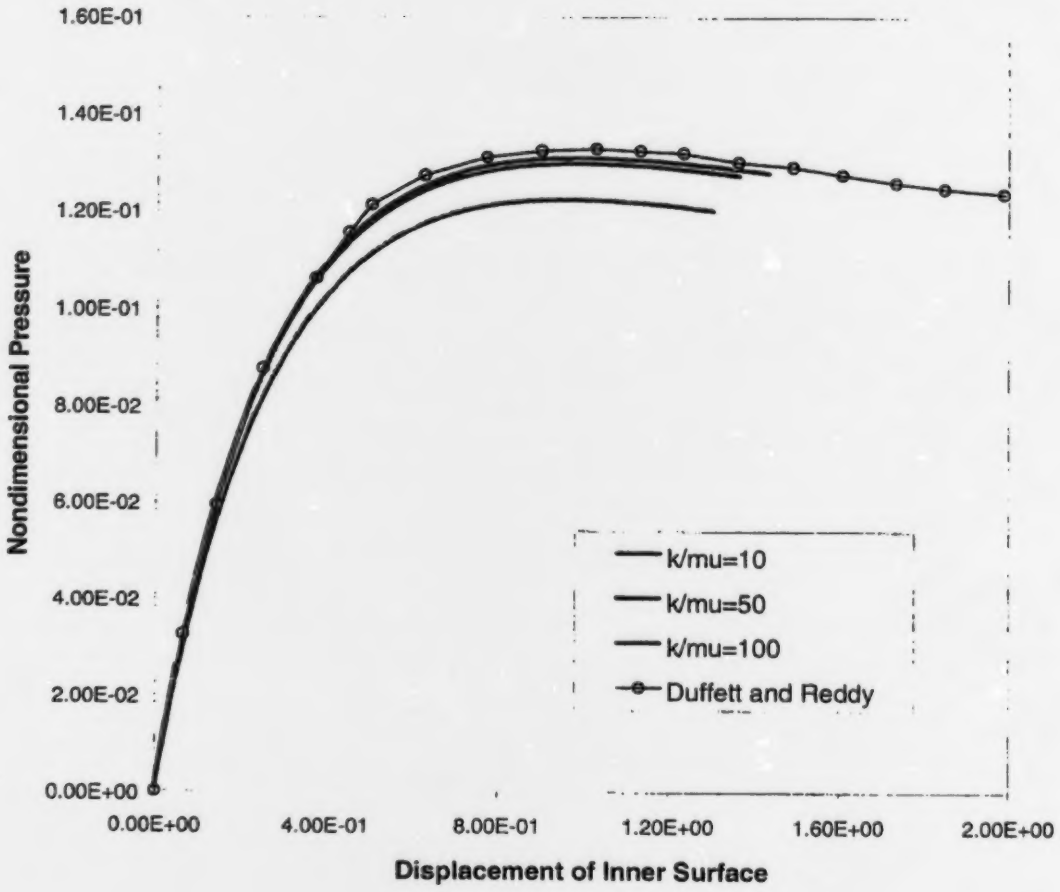

Figure 4.5: Comparison of the Reference Solution and the VAST Predictions Using the Coarse Mesh and Various Values of Bulk Modules for the Plane Strain Expansion of the Thick Rubber Cylinder.

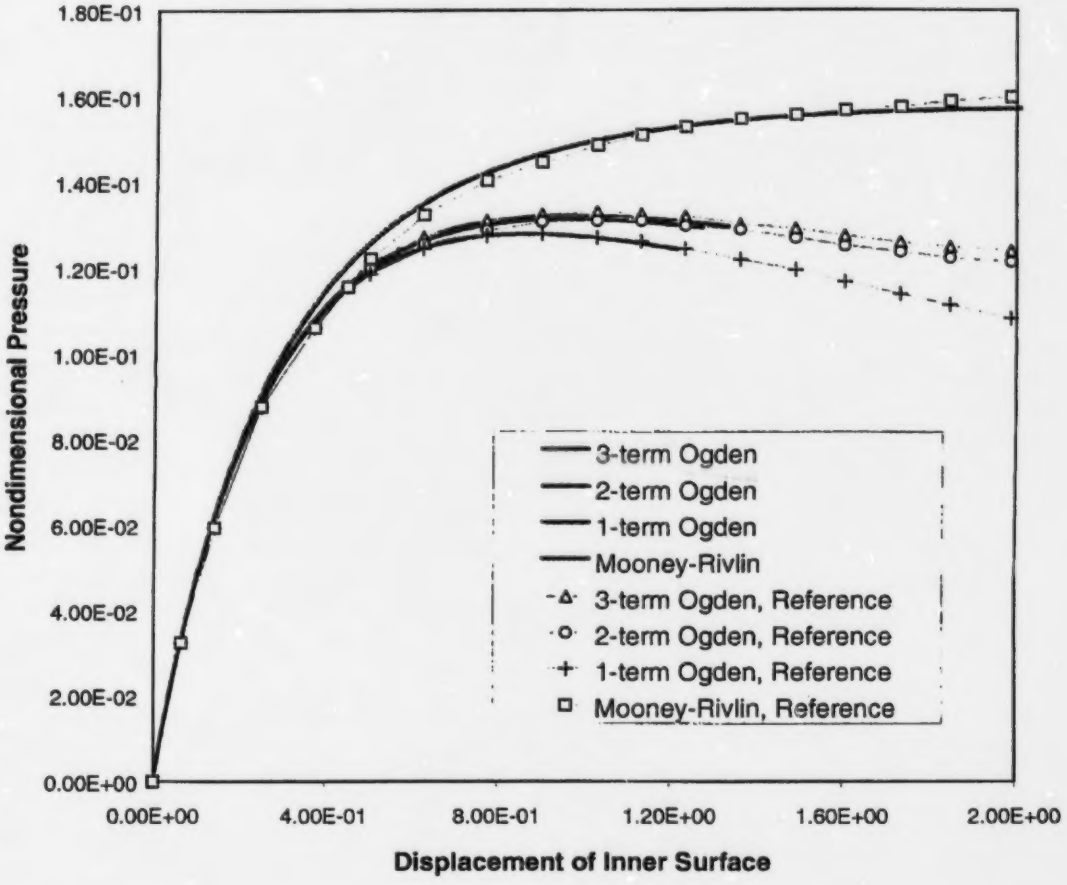

Figure 4.6: Comparison of the Reference Solution and the VAST Predictions Using the Coarse Mesh for the Plane Strain Expansion of the Thick Rubber Cylinder with Various Hyperelastic Material Constants.

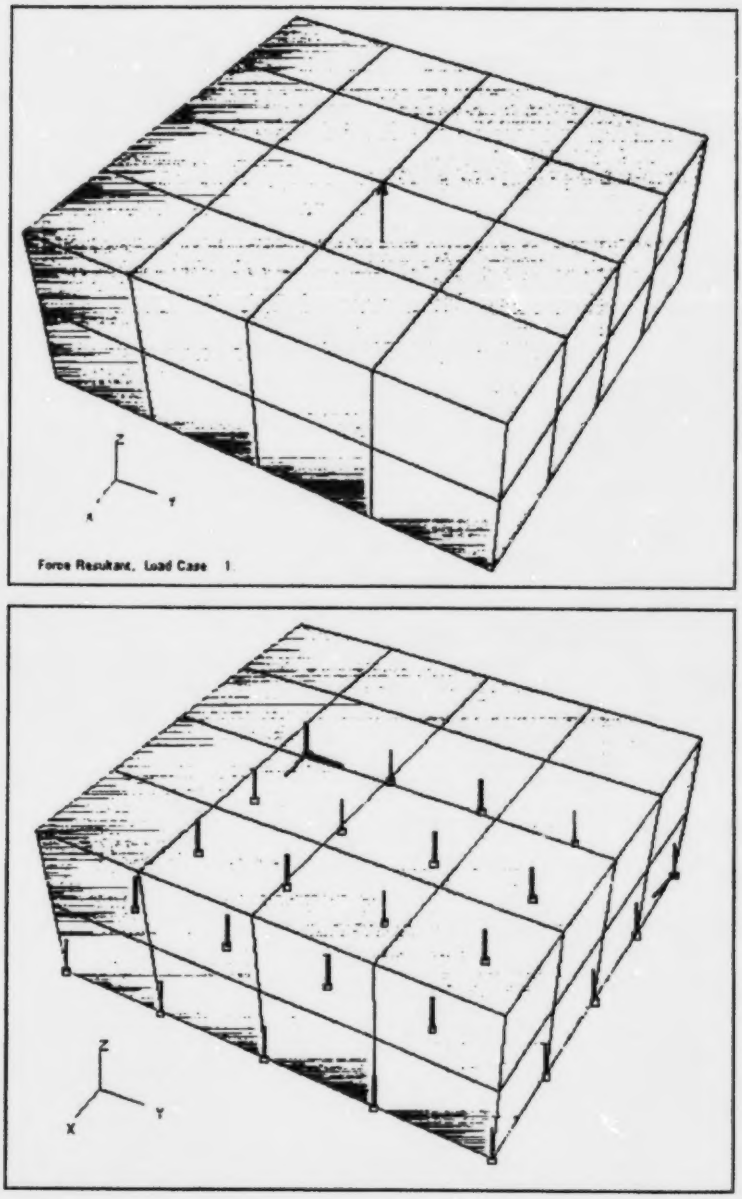

Figure 4.7: A Simplified Engine Mount Model Used for Frequency Response Analyses. (a) Concentrated Dynamic Load and (b) Boundary Conditions.

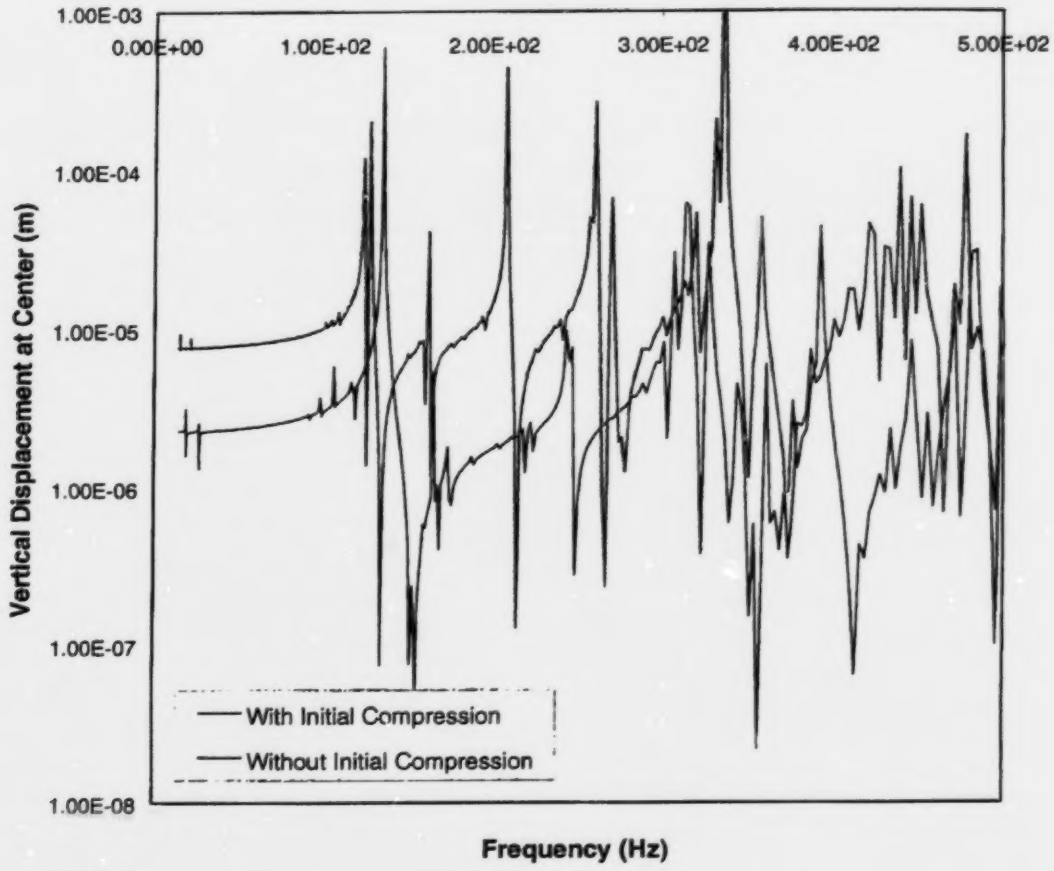

Figure 4.8: Comparison of Undamped Frequency Responses of the Engine Mount With and Without Initial Static Compression

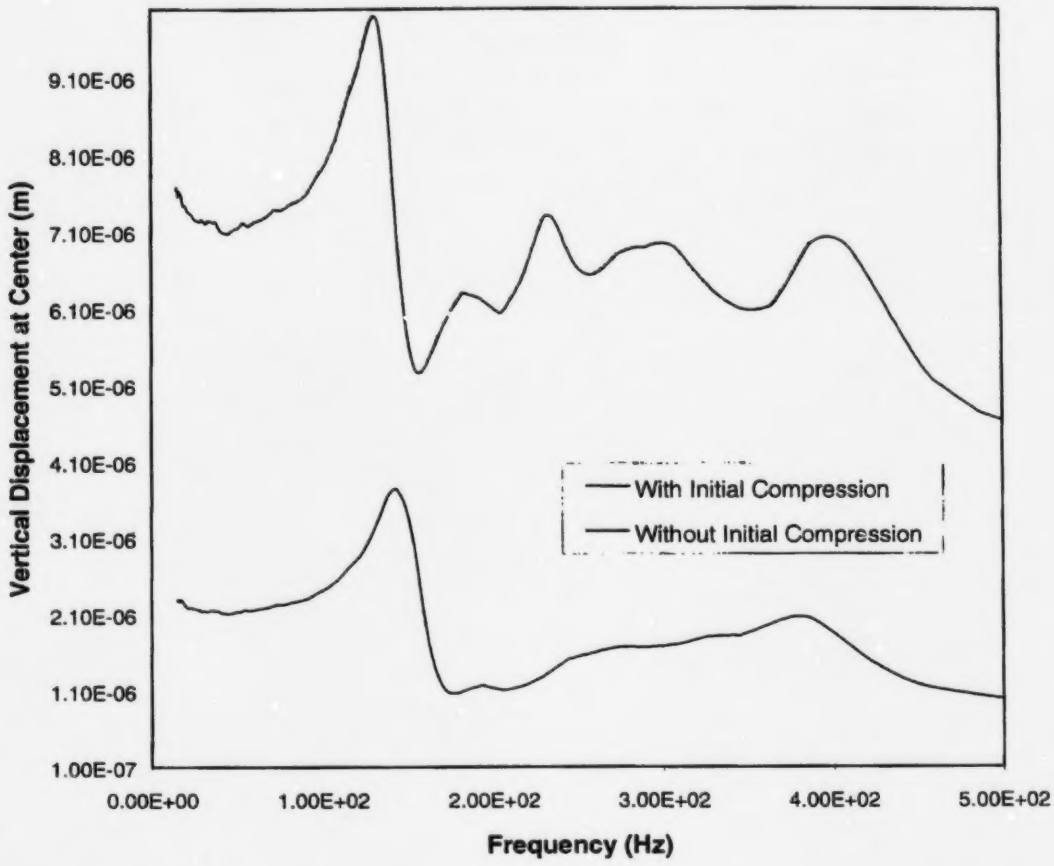

Figure 4.9: Comparison of Damped Frequency Responses of the Engine Mount With and Without Initial Static Compression

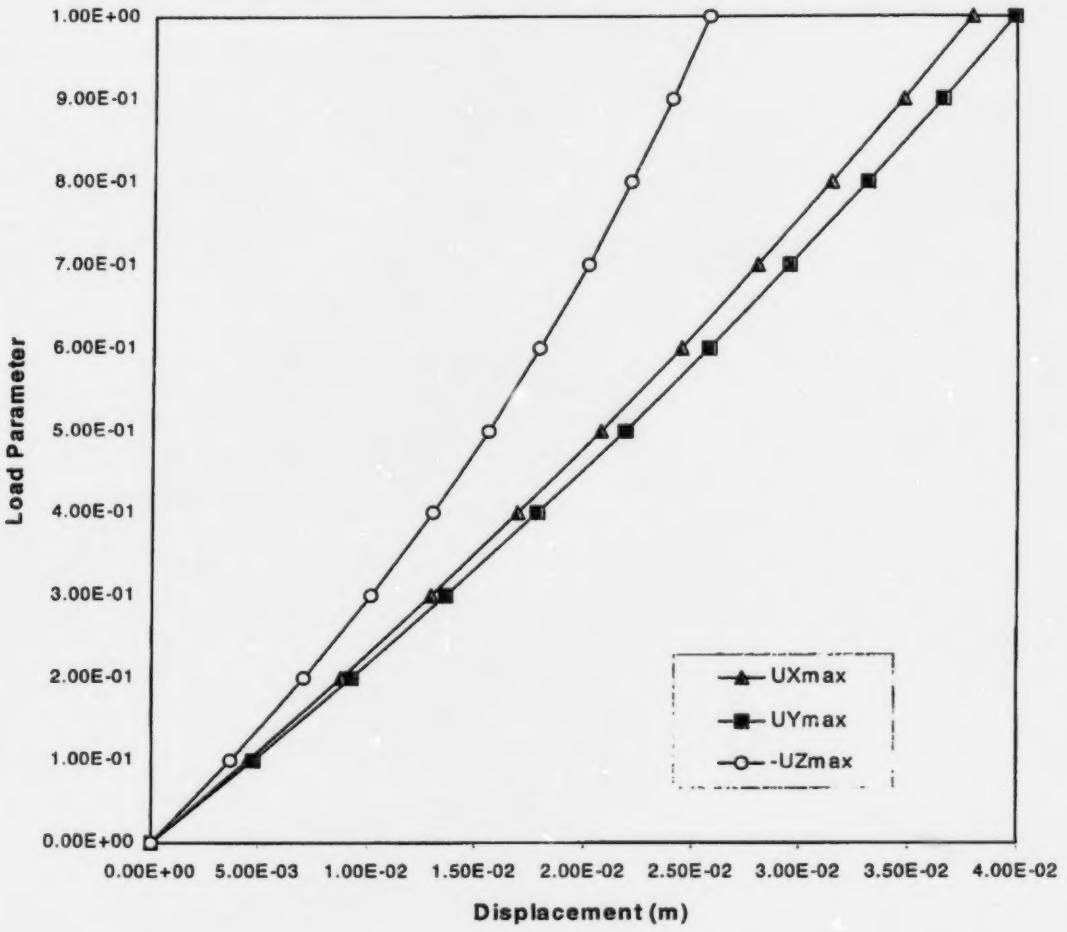

Figure 4.10: Load-Deflection Curves for Nonlinear Static Analysis of the Engine Mount Under Initial Compression.

5. CONCLUSIONS AND RECOMMENDATION FOR FURTHER WORK

In this report, numerical results from an extended finite element study of a pre-stressed engine mount were first presented. This study was motivated by the solutions of a series of frequency response analyses of the engine mount conducted at DREA using the VAST finite element program. These previous frequency response analyses results indicated that if the geometric stiffness matrix caused by the pre static loading was included, VAST predicted a overly soft structural response comparing with the experimental data. In order to understand the cause of this numerical problem, various types of analyses were conducted in the present contract, including linear buckling analyses, frequency response analyses, and nonlinear static and dynamic analyses using VAST and other finite element packages. Different solid elements and meshes were considered. The results of this investigation not only verified the correctness of the geometric stiffness formulation adopted in the solid elements in VAST, but also indicated that nonlinear hyperelastic material models must be employed to obtain the acoustic stiffness solutions of pre-stressed engine mount accurately.

Following this observations, a literature survey was carried out on state-of-the-art finite element formulations for 3D large strain analyses and the co-rotational method proposed by Crisfield and co-workers was identified as the most suitable one for implementation into the VAST program. Due to the basic assumption adopted in this co-rotational method, which states that the deformation gradient was uniform over the element, it is more appropriate to apply this method to lower-order solid elements. The theoretical background and computer implementation issues of this 8-noded co-rotational solid element for geometrically nonlinear and elasto-plastic analyses were given in Chapter 3, whereas detailed derivations of the hyperelastic material model was presented in Chapter 4. To enhance the performance of the 8-noded solid element in problems involving bending dominant deformations and incompressible materials, incompatible bubble displacement modes have been incorporated. A large number of numerical verification problems were solved using this newly developed 8-noded solid element and the present results were compared with the published solutions and VAST solutions obtained using other element types. Although general agreement was observed, the new nonlinear solid element did experience convergence difficulties in some situations.

In particular, for the problem of plane strain expansion of a thick rubber cylinder subjected to internal pressure, VAST runs broke down shortly after the peak load and solutions could not be continued with even extremely small solution steps. As has been demonstrated by Moita [11] in his thesis, the 3D co-rotational formulation, on which the present development has been based, had the capability to solve the thick cylinder problem without any numerical difficulties. This suggested that there are still some small defects in the VAST implementation of the co-rotational formulation. One example of these defects is the simplified treatment of the internal variables during nonlinear analyses. Other defects could have been caused by the misunderstanding of some details of the nonlinear formulation. Because Moita's thesis, that contained a quite detailed description of the formulation, did not arrived until very close to the end of the contract, it has not been studied thoroughly at the present time. Unfortunately, further investigation into this formulation is no longer permissible due to the budgetary constraint in the present contract.

In addition to the convergence problem discussed above, the Ogden's hyperelastic material model implemented in this contract also requires additional verification. The VAST results should be compared with those of other finite element packages, including ANSYS and ADINA. These investigation and improvement of the present nonlinear solid element should be addressed in the next phase of the development.

6. REFERENCES

[1] E.J.M. NIJMAN. Structure-borne Sound Transfer of Eight VRD Sandwich Mountings, Institute of Applied Physics, Delft. January 12, 1988.

[2] L. JIANG, M.F. PALMETER and M.W. CHERNUKA. Enhancement of Frequency Response and Damping Capabilities of the VAST Finite Element Computer Program, Martec Technical Report TR-95-15, Martec Limited, Halifax, 1995.

[3] L. JIANG and M.W. CHERNUKA. Further Enhancement of Frequency Response and Damping Capabilities of the VAST Finite Element Code (Phase III). Part I: Development of Multi-layered Shell Elements, Martec Technical Report TR-96-28, Martec Limited, Halifax, 1996.

[4] L. JIANG and M.W. CHERNUKA. Further Enhancement of Frequency Response and Damping Capabilities of the VAST Finite Element Code (Phase III). Part II: Development of an Out-of-Core Complex Eigen Problem Solver, Martec Technical Report TR-97-23, Martec Limited, Halifax, 1997.

[5] L. JIANG and M.W. CHERNUKA. Further Enhancement of Frequency Response and Damping Capabilities of the VAST Finite Element Code (Phase III). Part III: Some New Features for Improved Modeling of Damped Structures, Martec Technical Report TR-97-24, Martec Limited, Halifax, 1997.

[6] J.P. SZABO. "Dutch VRD 35MO-54 Natural Rubber Mount." Technical Letter, DREA Dockyard Lab, October, 1998.

[7] M.A. CRISFIELD and G.F. MOITA. "A Co-rotational Formulation for 2-D Continua Including Incompatible Modes." *International Journal for Numerical Methods in Engineering*, Vol. 39, pp. 2619-2633 (1996).

[8] G.F. MOITA and M.A. CRISFIELD. "A Finite Element Formulation for 3-D Continua Using the Co-rotational Technique." *International Journal for Numerical Methods in Engineering*, Vol. 39, pp. 3775-3792 (1996).

[9] M.A. CRISFIELD and G.F. MOITA. "A Unified Co-rotational Framework for Solids, Shells and Beams." *International Journal of Solids and Structures*, Vol. 33, pp. 2969-2992 (1996).

[10] M.A. CRISFIELD, G.F. MOITA, G. JELENIC and L.P.R. LYONS. "Enhanced Lower-Order Element Formulations for Large Strains." *Computational Plasticity – Fundamentals and Applications*, Pineridge Press, Swansea, U.K. pp. 293-320, 1995.

[11] G.F. MOITA. Non-Linear Finite Element Analysis of Continua with Emphasis on Hyperelasticity, Ph.D. Thesis, Imperial Collage, London, 1994.

[12] K.J. BATHE. Finite Element Procedures, Prentice Hall, New Jersey, 1996.

[13] S. TIMOSHENKO. Theory of Elastic Stability. McGraw-Hill, New York, 1936.

[14] B. NOUR-OMID and C.C. RANKIN. "Finite Rotation Analysis and Consistent Linearization Using Projectors." *Computer Methods in Applied Methods and Engineering*, Vol.93, pp.353-384 (1991).

[15] L. JIANG and M.W. CHERNUKA. Implementation of a Large Displacement Capability for VAST – Phase II, Martec Technical Report TR-93-14, Martec Limited, Halifax, 1993.

[16] R.L. TAYLOR, P.J. BERESFORD and E.L. WILSON. "A Non-conforming Element for Stress Analysis." *International Journal for Numerical Methods in Engineering*, Vol.10, pp.1211-1219 (1976).

[17] E.L. WILSON and A. IBRAHIMBEGOVIC. "Use of Incompatible Displacement Modes for the Calculation of Element Stiffnesses or Stresses." *Finite Elements in Analysis and Design*, Vol. 7, pp.229-241 (1990).

[18] J.C. SIMO and F. ARMERO. "Geometric Nonlinear Enhanced Strain Mixed Method and the Method of Incompatible Modes." *International Journal for Numerical Methods in Engineering*, Vol.33, pp.1413-1449 (1992).

[19] L. JIANG and M.W. CHERNUKA. Implementation of an Elastic-Plastic Analysis Capability for the VAST Finite Element Computer Program, Martec Technical Report No.: TR-95-23, Martec Limited, Halifax, 1995.

[20] L.R.G. TRELOAR. The Physics of Rubber Elasticity, Clarendon Press, Oxford, 1975.

[21] M. MOONEY. "A Theory of Large Elastic Deformations." *Journal of Applied Mechanics*, Vol. 11, pp. 582-592 (1940).

[22] R.S. RIVLIN. "Large Elastic Deformations of Isotropic Materials IV. Further Developments of the General Theory". *Philosophical Transactions of the Royal Society of London*, Vol. A241, pp. 379-397 (1948).

[23] R.W. OGDEN. Nonlinear Elastic Deformations, Ellis Horwood, Chichester, U.K. 1984.

[24] G. DUFFETT and B.D. REDDY. "The Analysis of Incompressible Hyperelastic Bodies by the Finite Element Method." *Computer Methods in Applied Mechanics and Engineering*, Vol. 41, pp. 105-120 (1983).

[25] F. GRUTTMANN and R.L.TAYLOR. "Theory and Finite Element Formulation of Rubberlike Membrane Shells Using Principal Stretches." *International Journal for Numerical Methods in Engineering*, Vol. 35, pp. 1111-1126 (1992).

[26] P. PAPADOPOULOS and R.L.TAYLOR. "A Generalized Newton Method for Higher-Order Finite Element Approximations in Non-linear Elasticity." *International Journal for Numerical Methods in Engineering*, Vol. 39, pp. 2635-2646 (1996).

[27] S.M. ARNOLD, A.F. SALEEB, H.Q. TAN and Y. ZANG. "Explicit Robust Schemes for Implementation of a Class Principal Value-Based Constitutive Models: Symbolic and Numeric Implementation." *International Journal for Numerical Methods in Engineering*, Vol. 37, pp. 1931-1944 (1992).

[28] E.A. DE SOUZA NETO, D. PERIC and D.R.J. OWEN. "Finite Elasticity in Spatial Description: Linearization Aspects with 3-D Membrane Applications." *International Journal for Numerical Methods in Engineering*, Vol. 38, pp. 3365-3381 (1995).

[29] T. SUSSMAN and K.J. BATHE. "A Finite Element Formulation for Nonlinear Incompressible Elastic and Inelastic Analysis." *Computers & Structures*, Vol. 26, pp. 357-409 (1987).